January 2010

# A Free-Breathing Lung Motion Model

Tianyu Zhao
*Washington University in St. Louis*

Washington University

Department of Physics

Dissertation Examination Committee

Dr. Mark Conradi, Chair
Dr. Daniel Low, Co-Chair
Dr. Andrew Carlsson
Dr. Joseph Culver
Dr. James Miller
Dr. Kevin Moore
Prof. Sasa Mutic
Dr. Parag Parikh

# A Free-Breathing Lung Motion Model

by

Tianyu Zhao

A dissertation presented to the
Graduate School of Arts and Sciences
of Washington University in
partial fulfillment of the
requirements for the degree
of Doctor of Philosophy

August 2010

Saint Louis, Missouri

# Acknowledgements

Any achievement in life is obtained with the assistance of others. This is my opportunity to thank those who made this dissertation possible.

First and foremost, I would like to thank my advisor, Dr. Daniel Low, who led me into this amazing field, taught me how to think with physics intuition and skepticism, and encouraged me to work independently. Without him, I would not be where I am now.

I am greatly indebted to Dr. Wei Lu, who provided the data that I started with. The helpful discussions with Dr. Kevin Moore on the mechanism behind respiration are much appreciated. Special thanks go to Dr. Jeffrey Bradley, Dr. Parag Parikh and Dr. Hiram Gay for their help in signing up patients, and Prof. Sasa Mutic for his generosity in providing me with the convenient access to clinical resources. This research also benefited a lot from Dr. Deshan Yang's knowledge on registration and Ms. Camille Noel's hard work in collecting patient data.

Many thanks to Mr. Benjamin White for the tremendous time he spent in discussing and proofreading this dissertation. I would also like to acknowledge Dr. Sara Wuenschel and Dr. James Lamb for various discussions and input relevant to this dissertation. I am deeply grateful to Ms. Cheryl Zmaila for all the kind and genuine support in all things that make a graduate student's life more livable.

Finally, I would like to thank my parents and my wife. It is their genuine love that sustains me throughout my life.

# Contents

**Acknowledgements** ii

**Table of Contents** iii

**List of Figures** v

**List of Table** vii

**1 Introduction**.....1
**1.1 Motivation and Background**.....1
**1.2.Overview of Dissertation**.....1

**2 Data Acquisition**.....16
**2.1 Image Acquisition**.....16
**2.1.1 16-Slice CT Acquisition**.....17
**2.1.2 64-Slice CT Acquisition**.....17
**2.2 Tidal volume and Air Flow**.....19
**2.2.1 Spirometer and Bellow**.....19
**2.2.2 Air Content Analysis**.....21

**3 Image Registration and Model Fitting**.....24
**3.1 Normalized Cross-correlation Coefficient Registration**.....25
**3.2 Optical Flow Registration**.....28
**3.2.1 Horn and Schunck's Algorithm**.....29
**3.2.2 TV-$L^1$**.....33
**3.3 Model Fitting**.....37
**3.3.1 Least-square Optimization**.....38
**3.3.2 Nelder–Mead Optimization**.....40

**4 Verification of the Lung Motion Model**.....46
**4.1 Introduction**.....46
**4.2 Methods and Materials**.....47
**4.2.1 Derivation of Divergence Relationship**.....47
**4.2.2 Evaluation Equations**.....50
**4.2.3 Evaluation Method**.....53
**4.3 Result**.....54
**4.4 Discussion**.....57

**5 Mechanics of Respiration**……62
**5.1 Stress Distribution in the Lung**……63
**5.2 Biomechanical Model**……..65
**5.3 Angle Analysis**……73
**5.4 Model Validation**……74
**5.4.1 Results from the Empirical Lung Motion Model**..75
**5.4.2 Results from the Biomechanical Model**……...76
**5.4.3 Comparison of $\vec{\alpha}$ and $\vec{\beta}$ between the Empirical Lung Motion Model and the Biomechanical Model**…..77
**5.4.4 Zenith Angle Distribution**……79
**5.5 Results**……79
**5.6 Conclusion and Discussion**……81

**6 Characterization of Free Breathing Patterns**……92
**6.1Introduction**……92
**6.2 Methods and Materials**……92
**6.2.1 Data Acquisition**……92
**6.2.2 Image Registration**……93
**6.2.3 Model fitting**……..95
**6.3 Result**……96
**6.4 Discussion**……99

**7 Clinical Application**……109
**7.1 Distortion of $\vec{\beta}$ in Cancerous Region**……111
**7.2 Model Stability**……..113
**7.3 Radiation Damage Monitoring**……115
**7.4 Breathing Motion Artifacts in Free Breathing PET Images**……120

**8 Conclusion** ……..135
**8.1 Conclusions**……135
**8.2 Future work**……...138

# List of Figures

1.1 Illustration of the free breathing motion model……..15

4.1 Integral of alpha divergence over lung space……56

4.2 Histogram of R in 35 patients…….57

5.1 Stress distribution……84

5.2 Illustration of directions of parameters……85

5.3 Baseline of $\vec{\alpha}$ and $\vec{\beta}$ spontaneous distribution……..86

5.4 Sagittal view of unbiased angle distribution in the left lungs of 3 patients……87

5.5 Sagittal view of unbiased angle distribution in the right lungs of 3 patients…..88

5.6 Normalized angle distribution in both lungs……89

6.1 The registration error of the normalized cross-correlation registration method…….101

6.2 Distribution of $|\vec{\alpha}|$ in a normal pattern……...103

6.3 Distribution of $|\vec{\beta}|$ in a normal pattern……..104

6.4 Distribution of $|\vec{\alpha}|$ in an abnormal pattern…….105

6.5 Distribution of $|\vec{\beta}|$ in an abnormal pattern……106

6.6 Histogram of the mean $|\vec{\alpha}|$ and $|\vec{\beta}|$ at the 85$^{th}$ percentile for 49 patients……..107

6.7 Cumulative histogram of discrepancies between measured and fit locations…108

7.1 Coronal view of model parameters in a lung cancer patient……..123

7.2 More examples on $\vec{\beta}$ discontinuity around cancerous region……...124

7.3 $|\vec{\alpha}|$ distributions of the non-lung cancer patient scanned two weeks apart……125

7.4 Histogram of discrepancy of $|\vec{\alpha}|$ between two scanning sessions…….126

7.5 $|\vec{\beta}|$ distributions of the non-lung cancer patient scanned two weeks apart……127

7.6 Histogram of discrepancy of $|\vec{\beta}|$ between two scanning sessions……128

7.7 $|\vec{\alpha}|$ distributions of one lung cancer patient scanned two weeks apart…….129

7.8 Dose delivered to the lung cancer patient…….130

7.9 Comparison of $|\vec{\alpha}|$ change in cranialcaudal direction……..131

7.10 Comparison of $\nabla \bullet \vec{\alpha}$ in an un-irradiated lung and an irradiated lung…….132

7.11 Application of the model in removing image artifacts…….133

7.12. Comparison of gated and ungated images……..134

# List of Tables

4.1 $\frac{V_{\max}}{f_{\max}}$ of all the patients……59

4.2 Integral of $\int_V \nabla \bullet \vec{\alpha} dV$ conducted over both lungs……60

4.3 Integral conducted $\int_V \frac{\nabla \bullet \vec{\beta}}{1.11 \times \frac{V_{\max}}{f_{\max}}}$ over both lungs……..61

5.1 90 percentile of $|\vec{\alpha}|$ and $|\vec{\beta}|$ in both left and right lungs……...90

# Chapter 1

# Introduction

## 1.1 Motivation and Background

In 2004, cancer accounted for 7.4 million deaths worldwide, around 13% of all deaths[1]. Among the deaths, 1.3 million were related to lung cancer. Lung cancer has surpassed heart diseases as the leading cause of death for people younger than 85 in the United States since 1999. In 2009, a total of 1,479,350 new cancer cases and 562,340 deaths from cancer were predicted in the United States, among which lung cancer was responsible for 219,440 new cases and 159,390 deaths, respectively.[2] Although the incidence rate has been declining dramatically among men, from 102.1 per 100,000 in 1984 to estimated 87.3 per 100,000 in 2009, the incidence rate for women had been increasing by 0.3% per year before 2003 and has been approaching a plateau ever since. While the overall lung cancer death rates have declined, it is anticipated to continue to be the leading cause of cancer deaths until at least the year 2040.[3] Overall lung cancer survival rate is quite small, with one-year survival rate at 41% and five-year survival rate at 15% for all stages combined, making it one of most notorious cancers.

The main types of lung cancer are small cell lung carcinoma (SCLC) and non-small cell lung carcinoma (NSCLC). It has been established that SCLC usually responds better to radiation and chemotherapy. Treatment options for NSCLC, which accounts for

approximately 80% of lung cancer cases, are still under heavy debate. Currently, radiation therapy and chemotherapy treat most of the NSCLC patients jointly or separately.

A typical conventional or conformal radiation therapy delivers 65 Gy with or without chemotherapy, achieving local tumor control at only 17% and 15% respectively.[4] Study also showed that local control could be greatly improved by escalating the radiation dose to the target[5]. However, the toxicity that accompanies higher radiation increases as the energy deposited to the lung volume increases. The suppressing of side effects and the improving of local control could be achieved by more accurately confining the dose to the target. A study by Kubota[6] compared treatment outcomes of chemotherapy only and treatments of chemotherapy followed by three-dimensional conformal radiation therapy, which is a method for attempting to conform the radiation therapy to the tumor. 92 patients at stage III were randomly divided into two groups. One group was given radiation of 50 to 60 Gy for 5 or 6 weeks after chemotherapy and another group received no radiation after chemotherapy. The first year survival rate in the chemotherapy only group was 66%, slightly higher than 58%, the survival rate of the chemo-radiation combining group. However, the two-year and three-year survival rate in the chemo-radiation combining group dramatically beat that of the chemotherapy only group, at 36% vs. 9% and 29% vs. 3%, respectively. The result indicates that if radiation therapy could take advantage of sophisticated dose targeting techniques, it would achieve better long-term survival.

As radiation therapy gradually established its principal role in treating NSCLC patients with localized disease, the conventional radiotherapy local control rate, which typically delivers 65 Gy, was disappointing. A model developed by Martel et al[7] predicted that doses of 84.5 Gy would be required to achieve a 50% tumor control rate in 30 months. A dose at this high level would raise the concern of radiation toxicity to normal tissue, including fatal side effects. Compared to conventional radiotherapy, conformal radiotherapy targets the tumor as accurately as possible while attempting to spare normal tissue. Sun et al[8] conducted phase I-II trials to compare the radiation response, acute and chronic toxicity, local control and survival rate of patients that were randomly selected to receive convention radiotherapy or concomitant boost radiation therapy which was able to more precisely confine the radiation to the tumor. The results were encouraging. For patients in the concomitant boost group, 46.8 Gy was delivered to the CTV (Clinical Target Volume, the gross disease and tissues with suspected disease) in 26 fractions, and an extra concomitant boost of 18.2Gy (0.7 Gy per fraction) was delivered to the GTV (Gross Tumor Volume, the tumor that can be detected by imaging or palpation) with a tight margin of 1.5cm to account for setup uncertainty. A combination of 65 Gy was delivered to the concomitant boost patients in 26 fractions. For patients in the conventional treatment group, 70.8 Gy was delivered in 38 fractions. The response rates were access by radiographs. The boost patients responded significantly better than did the conventional patients, with response rate of 69.8% vs. 48.1%. Acute toxicity was evaluated by measuring the pre- and post-radiotherapy pulmonary function. No significant difference in toxicity was reported in the two groups.

Preliminary data concerning further dose escalation were reported in a phase 1 trial conducted by Hayman et al[9], using conformal therapy techniques. The initial doses ranged from 63 to 84 Gy. Due to the lack of the ability to design effective treatment plans that both covered the tumor and spared the surrounding normal tissue, some of the enrolled patients were unable to be treated to the protocol doses. The investigators hypothesized that Intensity Modulated Radiation Therapy (IMRT) would be able to meet the normal tissue constraints and allow further dose escalation.

IMRT is an advanced approach to high-precision radiation whose clinical applications are expanding to challenging body sites such as the central never system, head and neck, and advanced prostate cancer. The process begins the same way as conformal therapy, with the acquisition of a simulation CT scan. The scan is acquired while the patient is in the intended treatment position and with the use of immobilization hardware that aids in patient positioning and patient compliance. Physicians segment the tumors using the CT scan datasets and they, or other clinical staff, segment the normal organs. The physician also provides a dose prescription, which typically includes the desired tumor dose and the dose limits of the critical organs. The segmentations, termed contours, provide the topological shape of the tumor and normal organs. These, along with the prescriptions, are provided to an inverse treatment planning system that identifies the radiation delivery sequence that best approximates the clinical goals. Unlike conventional and conformal radiation therapy where the intensity of each beam is uniform, the beam intensity in IMRT is modulated by multileaf collimators according to the instructions provided by the treatment planning system. Modulating of beam intensities allows better conformation of

the dose distribution to the tumor shape than is available by conventional and conformal therapy techniques.

Although IMRT has proven its value in achieving more precise dose delivery, the benefit of IMRT in treating lung cancer is greatly limited by organ motion. During natural breathing cycles, the tumor position is not stationary, but traverses a trajectory that varies as the patient's breathing depth and frequency varies. There are many methods for dealing with breathing-induced tumor motion. The simplest is to extend the tumor shape in the treatment plan to encompass the tumor motion. This is termed the internal target volume (ITV) and results in an increased beam aperture size to irradiate the larger volume. The dose distribution is delivered throughout the patient's breathing cycle. The consequence of this method is that it delivers more dose to the surrounding normal tissues than would be possible if the tumor were stationary.

Gated conformal therapy was developed to assist with the challenges of moving tumors. In gated therapy, the treatment plan is conducted assuming that the radiation will be on only during a user-specified phase of breathing. The position of the tumor is monitored by correlating it against a real-time measurement of either an internal or external surrogate. When the surrogate indicates that tumor is entering the appropriate breathing phase, or the gating window, the radiation beam is energized. The beam is shut off when the surrogate indicates that the tumor has exited the gating window. The major source of error from this technique comes from the poor of reliability of the correlation between the surrogate and the tumor position. Therefore, many clinics require independent

conformation of the tumor position prior to treatment using, for example, implanted fiducial markers imaged using fluoroscopic techniques[10] .

The gating technique provides a measure of motion compensation for conventional radiotherapy. Its application in IMRT is compromised by assumptions inherent in IMRT dose delivery. The power of IMRT rests in its ability to subdivide the treatment into a sequence of interlocking inhomogeneous fluences delivery from a variety of angles. The inhomogeneous fluences are delivered by a time-dependent pattern that explicitly assumes that the remaining fluence delivery will be properly aligned. While these fluences can accurately superimpose in the treatment room coordinate systems, the lung and lung tumor tissue is moving during the delivery sequence, so the delivered dose from each beam does not match the successive beams. While gating reduces the intensity of this problem, it does not eliminate it. Currently available IMRT treatment planning systems lack of the ability to correlate the breathing cycle with the delivery sequence, so the magnitude of this problem is not typically known to the treatment planner. The dose errors due to breathing motion are dominated by a broader penumbra[11] and also contain dose delivery errors in the tumor and normal organs[12]. The concerns over dose superposition breakdown due to tumor mobility lead to a guideline published by the National Cancer Institute to limit the clinical use of intra-thoracic IMRT.

Methods to improve the dose delivery for free breathing patients include expanding the radiation portal to account for the motion[13], gating the radiation delivery to synchronize the radiation delivery with the position of the tumor[14,15], tracking the tumor motion with

the radiation portal[16,17,18] and managing breathing motion. Motion management includes free breathing[19-25] coupled with a method for modifying the dose delivery to account for motion, breath hold[26-28], breathing coaching[29], where the patient uses biofeedback to guide their breathing pattern, and abdominal compression. Breath hold and breathing coaching both require cooperation of the patient for accurate implementation. An informal survey of institutions that use these techniques has shown that patient compliance is limited to approximately 50%. Abdominal compression does not require patient compliance, but significant reduction of tumor breathing motion is achieved in a minority of tumors. Free breathing requires neither cooperation nor an external device for implementation, but it does not reduce the tumor motion. It may, however, provide a stable method for predicting the tumor motion during therapy, thereby allowing an accurate prediction of the impact of gating techniques.

The free-breathing treatment planning strategies require a breathing motion model. The model is typically based on CT scans acquired during free breathing and sequenced using a simultaneously acquired breathing surrogate. The surrogate is typically a non-invasive measurement device such as a pneumatic belt placed around the abdomen, camera system that monitors a marker placed on the patient's abdomen or pelvis, or pressure sensor mounted to a belt that is wrapped around the abdomen[14,24]. There are two surrogates used in our research group when we conduct CT scans for free-breathing motion research; a pneumatic belt (bellows) placed around the abdomen, and a spirometer (Interface Associates, VMM 400). The spirometer measures the breathing flow rate, but has

significant measurement drift that precludes its independent use. Simultaneous acquisition of the bellows and spirometry signals allow us to correlate the two signals and remove the drift artifact inherent in the spirometry signal Therefore, the surrogate used to sequence the 4D CT scans can be the patient's tidal volume, a surrogate that has direct physiologic significance.[30]

Verified breathing models have not yet been established. Many investigators have relied on the periodic nature of the breathing pattern to develop mathematical models that use time as an explicit variable. These use the assumption that the breathing motion can be accurately described as a function of time[31]. Seppenwolde et al. [21] modeled breathing in this way using an even power of a cosine function with adjustable period and amplitude. They showed that in some cases, this was able to fit the motion of embedded clips, but also showed that changes in breathing frequency or amplitude were difficult to model.

The breathing motion model may be as simple as identifying the position of the tumor throughout the breathing cycle with the breathing cycle subdivided equally in time between successive peak inhalations or exhalations. This is termed phase-angle based gating. Each breathing phase is assumed to coincide with a constant fraction of time during the breathing cycle. For example, the breathing cycle time can be described as proportional to an angle, from 0° to 360° from peak-to-peak. The CT scan can be gated as a function of the measured breathing cycle, forming a 4D CT scan dataset. Examination of the CT scans reconstructed at each breathing phase allows the treatment planner to determine the overall tumor motion as well as linear accelerator gating

efficiency by identifying the fraction of the 360° breathing cycle for which the beam will be activated. However, this phase-angle based model assumes that breathing patterns are consistent and reproducible, an inaccurate assumption for many lung cancer patients. [32]

A mathematical model of breathing motion would be very useful. It would allow a treatment planning system to examine a recorded breathing cycle and develop a prediction for the positions of the tumor and normal lungs during a simulated treatment. This would allow for an improved prediction of the impact of using an ITV model or predict gating efficiency and its dosimetric impact. Low, et al. [33] developed a breathing motion model that assumed that one of the independent model variables should be the tidal volume. For quiet respiration, the tissue motion was assumed to be linearly proportional to the tidal volume.

Research [34-41] on modeling dynamic lung motion has been conducted with limited success. Most of the work, based on Weibel's model[42] on bronchial anatomy, has applied the principles of fluid dynamics or viscoelasticity to modeling lung motion. However, because of lack of detailed information of lung's inner structure, their results cannot be personalized. Their work can be used to understand the mechanical behavior of lung under different circumstances. The stress distribution without considering the airway resistance was established by Mead[43], indicating that tidal volume may play an important role in modeling lung motion. Lambert[36] established that there are pressure losses in the flow along the airway, from the periphery to the flow-limiting site. A linear relationship between the pressure loss and flow rate was selected because of the low Reynolds's

number found in the bronchial tree. In general, regions with stronger or weaker air resistance, corresponding to worse or better communication with the outside air, longer or shorter airways from the trachea, will have lower or higher air pressure during respiration. The opposite would therefore occur during exhalation, namely that the regions that had lower pressure during inhalation would have greater pressure during exhalation.

Based on the relationship between pressure and airflow, and the fact that different regions of the lungs have different resistance to airflow, hysteresis, defined as differential tissue motion between inhalation and exhalation, was hypothesized by Low, et al. [33] to be caused by pressure distribution imbalances during breathing. For quiet respiration, these pressure imbalances are further assumed to be proportional to the vacuum developed to generate respiration, and that vacuum is in turn assumed to be proportional to the airflow into the mouth. For quiet respiration, a further model approximation is made that the hysteresis motion magnitude was proportional to the airflow.

Finally, the motion model by Low et al[33] assumed that during quiet respiration, the motion component due to tidal volume changes was independent of the motion component due to pressure differentials and consequently airflow. Under this assumption, hysteresis motion due to pressure imbalances would occur with the same magnitude regardless of the tidal volume, and the tidal volume lung expansion component at a specific point in time would not depend on the rate of breathing.

The use of tidal volume and airflow to describe free-breathing motion allows the time dependence of the model to exist outside the mathematical description of tissue motion. The time dependence lies in the behavior of the tidal volume and airflow and does not explicitly exist within the model equation. The positions of lung tissues are therefore hypothesized to be functions of 5 independent parameters; the 3D positions of the tissue at a reference tidal volume and airflow (typically 0 ml and 0 ml/s), the tidal volume, and the airflow [44,45].

As Low, et al[33] hypothesized, the position of lung tissues can be described by a linear approximation in tidal volume and airflow. The original mathematical description has been modified here for clarity. $\vec{X}_0$ is defined as the reference position, where the piece of tissue of concern is at located at zero tidal volume and zero airflow. The position $\vec{X}$ at tidal volume $V$ and airflow $f$ is

$$\vec{X}(v, f : \vec{X}_0) = \vec{X}_0 + \vec{\alpha}(\vec{X}_0)V + \vec{\beta}(\vec{X}_0)f \qquad (1.1)$$

where $\vec{\alpha}(\vec{X}_0)$ and $\vec{\beta}(\vec{X}_0)$ relate the tissue position of the tissue $\vec{X}_0$ to the tidal volume and airflow, respectively. Fig. (1.1) shows an illustration of the breathing motion model superimposed with data acquired from an enrolled patient

## 1.2 Overview of Dissertation

In this dissertation, the breathing motion model described in Eq. (1.1) is discussed and verified.

The major objectives of this dissertation are

1. Develop a CT acquisition and reconstruction process and a deformable registration process that optimally and efficiently provides the positioning data for the proposed breathing motion model.
2. Verify the model.
3. Develop a theoretical interpretation for the breathing motion model.
4. Verify the stability of the breathing model by showing that the breathing motion model parameters do not change in healthy subjects (lungs without any progressing pulmonary disease and not being irradiated), and that detectable changes occur to irradiated lungs.
5. Develop a process that models localized tissue response to radiation therapy and correlates that response to radiation dose

Chapter 2 describes the protocol of image acquisition on a 16-slice and 64-slice CT scanners with details describing tidal volume and air flow measurements using a spirometer. An alternative method for determining tidal volume and air flow for patients who cannot tolerate the use of a spirometer is also discussed.

Chapter 3 gives a brief description of the image registration and fitting methods that were used for this study. Image registration tracks image features through the images acquired at different tidal volumes and air flows. The image feature trajectories, together with

corresponding tidal volumes and airflows, are used to fit the model parameters. (Objective 1)

Chapter 4 gives a self-consistent verification of the breathing motion model using the continuity equation. (Objective 2)

Chapter 5 gives a biomechanical interpretation of the model parameters that involves the stress distribution and Young's modulus. Model parameter averages are estimated from published data. Patient-specific model parameters are then estimated using real patient data. Verification is conducted by comparing the theoretical prediction and results from real patient data. (Objective 3)

Chapter 6 is an application of the breathing motion model in characterizing free-breathing patterns. The breathing motion model parameters for lung cancer and non-lung cancer patients under quiet respiration are reported for a large cohort of patients. The parameters $\vec{\alpha}$ and $\vec{\beta}$ together provide a quantitative characterization of breathing motion that inherently includes the complex hysteresis interplay. The $\vec{\alpha}$ and $\vec{\beta}$ distributions are examined for each patient to determine overall general patterns and inter-patient pattern variations.

Chapter 7 describes potential applications of the breathing motion model in localizing lung cancer, monitoring radiation damage and suppressing artifacts in free-breathing PET images. The stability of the model is evaluated by investigating the consistency of model parameters calculated on image datasets of a healthy lung obtained two weeks apart. The $\vec{\alpha}$ vector field divergence is related to the variation of local density during breathing. Comparing the divergences of $\vec{\alpha}$ at various points along the course of treatment might localize changes in lung tissue biomechanical properties due to radiation damage. (Objective 4 and Objective 5)

Chapter 8 summarizes the main conclusions drawn from the study in this dissertation and proposes future work. The future work include, but not limited to, quantitative guidance for treatment planning, evaluation, staging and management of respiratory diseases in addition to cancer, quantitative nuclear medicine (PET/CT and SPECT/CT) study acquisition for free breathing patients without breathing motion artifacts

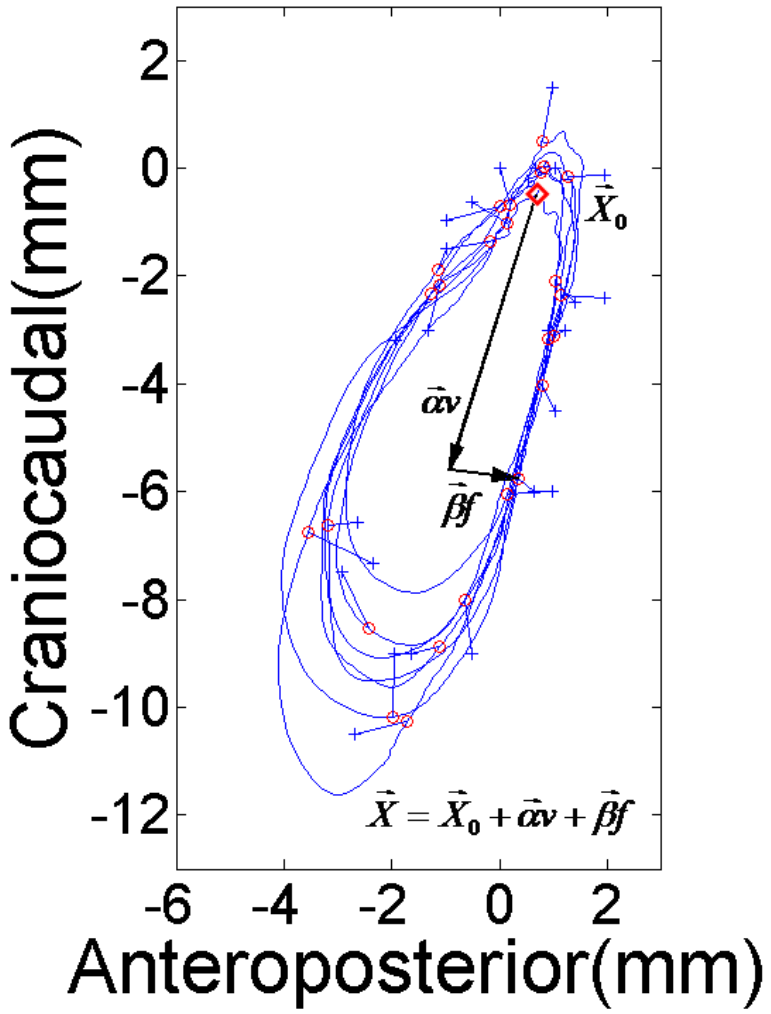


Figure 1.1: The breathing motion model (circles) of a piece of tissue as determined using the measured positions (crosses). $\vec{X}_0$, shown as a diamond, was the location of that tissue at the reference tidal volume and airflow, 0 L and 0 L/s respectively. The displacement vector for a selected tidal volume and airflow is decomposed into the two components, $\vec{X}_v = \vec{\alpha}v$ and $\vec{X}_f = \vec{\beta}f$, which are the tidal volume and airflow components, respectively. The lines connecting the measured and fit locations are the motion model discrepancies. The mean discrepancy in this case was 1.25mm, approximately 13% of the total motion.

# Chapter 2

# Data Acquisition

The inputs to the breathing motion model are the positions of lung tissues and accompanying tidal volumes and airflows. The lung tissue positions are obtained by registering a series of volumetric CT scans that are acquired while the patient's breathing patterns are being quantitatively measured. These positions, together with the tidal volumes and airflows at the acquisitions, constitute the raw data input to our breathing motion model.

## 2.1 Image Acquisition

A 12-slice CT scanner was used to acquire the images when the breathing motion model was proposed in 2005. The scanner was capable of simultaneously acquiring 12 slices of lung in the craniocaudal direction. The thickness of each slice was 1.5 mm. Technology in CT scanner has made a huge progress since then. We acquired all the patient data used in this study in a 16-slice and then a 64-slice CT scanner. Although we have started to collect patient data using the 64-slice CT scanner using a craniocaudal resolution that is better than the 16-slice CT scanner, the large patient dataset we acquired using the 16-slice CT scanner served as an outstanding dataset. In this dissertation, data acquired

using both scanners were used. Therefore, acquisition protocols that were used for both scanners are described.

### 2.1.1 16-Slice CT Acquisition

49 patients were enrolled under an IRB-approved protocol and scanned using a 16-slice CT scanner (Philips 16-slice Brilliance CT) operating in ciné mode using 1.5 mm thick slices. Each contiguous set of the simultaneously acquired 16 CT slices was termed a couch position, which covered 24 mm craniocaudally. The scanner was operated to acquire 25 scans per couch position using a 0.46 s rotation, $360^{o}$ reconstruction, and 0.32 s between successive ciné acquisitions, requiring 19.2 s to acquire the 25 scans. Nine or ten abutting couch positions were typically required to span the entire lung. The in-plane field of view was 500 mm and images were reconstructed using 512 x 512 voxel matrices.

### 2.1.2 64-Slice CT Acquisition

Currently, we have 25 patients enrolled under an IRB-approved protocol and scanned using a 64-slice CT scanner (Philips 64-slice Brilliance CT) operating in ciné mode using 0.625 mm thick slices. A couch position in 64-slice CT scanner covered 40 mm of lung craniocaudally. The scanner was operated to acquire 25 scans per couch position using a 0.42 s rotation, $360^{o}$ reconstruction, and 0.32 s between successive ciné acquisitions, requiring 18.2 s to acquire the 25 scans. Six or seven abutting couch positions were typically required to cover the whole lung. The in-plane field of view was 500 mm and images were reconstructed using 512 x 512 voxel matrices.

The advantages of the 64-slice CT scanner over 16-slice CT scanner included the improved image resolution and extended couch position length. The improved image resolution provided more anatomic detail to facilitate feature tracking. In addition, extended craniocaudal coverage between the two scanners reduced the number of couch positions required to cover the lung and thus reduce the number of intra-couch position boundaries. Six couch positions were usually sufficient to cover the lung in the 64-slice CT scanner. An illustration of boundary aliasing can be found in Yang's work.[46]

In the future, we would like to modify the current image data acquisition protocol. Theoretically, the minimum number of scans required to fit the model parameters is 3. The purpose of acquiring 25 scans on the same couch position was to provide enough redundancy to allow for breathing irregularities and provide redundancy to check short-term reliability and breath-to-breath reproducibility. The scans used in these studies were reconstructed using 360º projections. We are currently working on using 180º reconstruction to reduce image blurring due to breathing motion. Sophisticated registration algorithms were also developed. In the future, we would like to distribute the 25 scans between successive half-overlapping couch positions. Therefore, instead of 6 abutting couch positions, we would have 11 couch positions that half overlap each other to cover the whole lung. Couch positions in this arrangement would greatly reduce boundary aliasing. Each couch position would have 12 scans to provide sufficient redundancy for breathing irregularities.

## 2.2 Tidal Volume and Air Flow

Tidal volume and air flow are the two surrogates used in the breathing motion model. The hypothesis is that, any unique pair of tidal volume and air flow corresponds to specific tissue position.

The acquisition of tidal volume and air flow was initially based on a spirometer and an abdominal pneumatic belt that corrected the spirometry drift. As we acquired data from more patients, we found some patients could not tolerate the spirometer. To make use of the portion of data acquired without spirometer, a new scheme was developed by measuring the amount of air in the lungs using the CT scans themselves. This quantity was termed the air content. .

### 2.2.1 Spirometer and bellows

.The tidal volume was acquired using a calibrated digital spirometer (Interface Associates, VMM 400) that was sampled at 100Hz with 1 ml digitization resolution[47,48]. The spirometer measured the airflow into and out of the mouth using an internal fan that was spun by the airflow as the patient breathed. The fan rotation rate was monitored by the spirometer electronics and a digital data stream was provided as the airflow passing through the spirometer. The spirometer was found to be accurate to within 2% in a laboratory measurement under constant airflow rates, but it drifted significantly in actual use. Therefore a separate drift-free metric was simultaneously acquired. An abdominal

pneumatic belt (Philips Medical Systems) was placed around the patient's abdomen and attached to a pressure transducer. The pressure decreased and increased during inhalation and exhalation, respectively, and for short time intervals, the relationship between the bellows pressure transducer voltage signal and spirometry was found to be linear after a linear spirometry drift correction. The time period to apply the linear drift correction and determine the relationship between spirometry-measured tidal volume and was set to 15 s, based on earlier analyses of the spirometer drift[32]. The drifted spirometer signal was compared against the belt signal for 15 second increments and the correlation coefficient between the two signals was computed. A linear drift correction was applied to the spirometer signal and the drift rate was determined by maximizing the correlation coefficient. The ratio of drift-corrected spirometry signal to bellows signal provided a scale factor that converted the bellows signal to tidal volume. The ratio was evaluated each 15 s throughout the CT scan acquisition, and the correlation between spirometry and the bellows signals is typically stable to a few percent over the course of 10 minutes.

The drift-corrected spirometry signal was used to recalibrate the bellows signal such that the final recorded values were tidal volume. To quantify the zero value of the tidal volume, the fifth percentile tidal volume was selected as 0 ml.

Because of sample-to-sample noise and digitization artifacts, the airflow was determined using a moving *n*th-order polynomial fit. *n* was selected to be five in this work based on the observation that no significant improvement was achieved by using a higher order polynomial fit. The airflow at time *t* was the analytical derivative of the fifth-order

polynomial of the tidal volume measurement taken over a time span of 0.41 s (41 samples) centered at the point where the airflow was determined. This method of determining the derivative was selected because it reproduced the tidal volume signal with a marked reduction in the derivative noise, allowing for a relatively smooth determination of the airflow.

### 2.2.2 Air content analysis

Occasionally, patients signing up the research protocol could not tolerate the spirometer. The leakage between the mouthpiece attached to the spirometer and the mouth could sometimes also compromise the precision of measurement. In those cases, the air content analysis appeared to be an effective way to determine the tidal volume and air flow. Compared to the spirometer, the air content analysis was more accurate, consistent and straightforward to apply to patients with irregular breathing.

CT scanners work by measuring the spatial distribution of x-ray attenuation coefficients using x-ray projections and inverse transforms. The attenuation coefficient $\mu$ is not typically displayed in the CT image. Instead the concept of Hounsfield Unit (HU) is used. The HU scale is set such that the value of water is zero and air is either -1000 or -1024, depending on the scanner manufacturer (Philips uses the standard of -1000). The relationship between the CT number acquired in a Philips CT scanner and $\mu$ can be described as

$$CT = \frac{\mu - \mu_{H_2O}}{\mu_{H_2O}} \times 1000 \tag{2.1}$$

where $\mu_{H_2O}$ is the linear attenuation coefficient of water for the x-ray beam energy.

Because the CT number is linearly proportional to the $\mu$, and for soft tissues, $\mu$ is proportional to density, an empirical equation[48] was used to determine the fraction of a CT voxel that contained air.

$$\text{Fractional air content} = 1.0 - \left( \frac{CT - \overline{CT}_{air}}{\overline{CT}_{tissue} - \overline{CT}_{air}} \right) \tag{2.2}$$

The average CT value of air ($\overline{CT}_{air}$) was sampled in the trachea. The average CT value of tissue ($\overline{CT}_{tissue}$) was estimated by sampling homogeneous soft tissue near the lungs and was assumed to be the same as lung tissue density exclusive of air. The reason for the use of averages rather than the empirical numbers (e.g. -1000 and 0), was that the x-ray beams are not monoenergetic and therefore experience beam hardening as they pass through the patient. This causes the CT numbers to be a function of the patient geometry, so the representative regions were sampled. The volume of air in a CT voxel is the product of fraction of air content and the voxel volume. The volume of air in a couch position was calculated by summing the volume of air of all CT voxels in the same couch position. For images from a 16-slice CT scanner, the voxel volume was 1.43$mm^3$; For images from a 64-slice CT scanner, the voxel volume was 0.60 $mm^3$

For each couch position, 25 air contents were calculated at various phases of breathing. Therefore, tidal volumes could not be fully recovered by simple summation of the air contents. However, bellow signals could be converted to bellow-based air contents for each couch position, given the assumption that the bellow signals and air contents is be linear in each couch position, except for a possible small time delay. The bellow-based air content could be used to recover the tidal volumes. This was achieved in the following steps.

First, for one couch position, 25 bellow signals that synchronize the acquisitions of image data in the same couch position were retrieved from the continuously acquired bellow signals. By least-square fitting the 25 bellow signals to 25 recovered air contents in that couch position, the correlation between bellow signals and air contents was obtained. The correlation was used to convert the continuous bellows signals to continuous bellow-based air contents for that couch position.

Second, the above procedure was repeated to generate bellow-based air content curves for all couch positions. Since the bellow-based air content curves of all couch positions were based on the same bellow signal curve, same position on each bellow-based air content curve is corresponding to the same breathing phase. The whole lung volumes during the acquisition now could be obtained by the summation of the bellow-based air content curves of all couch positions. Tidal volumes were consequentially obtained by zeroing the $5^{th}$ percentile of air content in the whole lung. More details can be found in the technical note by Rene et al[49]

# Chapter 3

# Image Registration and Model Fitting

The goal of the lung motion model developed in this dissertation is to predict lung tissue trajectories by determining the motion model parameters using few samples of the motion trajectory coupled with the corresponding tidal volumes and air flows. The methods for determining the tissue positions in each of the CT scans are described in this chapter. The techniques for fitting the motion model parameters using the registered tissue positions, and corresponding tidal volumes and airflows will also be discussed in this chapter.

Image registration is the process of finding the geometrical or spatial mapping between multiple images of the same objects by determining the correspondence between the images. Registration techniques have been widely used in medicine to identify a patient's tissues throughout multiple image datasets. In this chapter, various image registration schemes will be discussed. These registration schemes were employed during the course of the research program and each had strength and weakness. A brief comparison of those methods will also be given in this chapter.

## 3.1 Normalized Cross-Correlation Coefficient Registration

In signal processing, the cross correlation is a measure of how much two signals resemble each other. Many signals evolve both temporally and spatially, so it is rare that a signal is identical at different points of time and position. In the imaging process, the signal is the image intensity distribution of the tissue of interest. The image intensity distribution changes as the organ moves. Additional distortions and image artifacts are introduced during the acquisition and reconstruction of images. Although variations are always present in images of the same tissue, it is reasonable to assume that images of the same organ will have the greatest similarity. The normalized cross correlation coefficient registration is a registration method based on the quantitative evaluation of the similarity between the two images.

The use of cross correlation for evaluating the similarity of two sub-images, $f$ centered at (0,0) and $g$ centered at ($x$,$y$), from a sequence of images is motivated by the squared Euclidean distance measure,

$$\begin{aligned} d^2_{f,g}(x,y) &= \sum_{u,v}\left(f(u,v)-g(u+x,v+y)\right)^2 \\ &= \sum_{u,v} f^2(u,v)+\sum_{u,v} g^2(u+x,v+y)-2\sum_{u,v} f(u,v)g(u+x,v+y) \end{aligned} \tag{3.1}$$

The cross-correlation term,

$$c(x,y)=\sum_{u,v} f(u,v)g(u+x,v+y) \tag{3.2}$$

is a measure of similarity between the two images if the image energy, termed as $\sum_{u,v} f^2(u,v)$ and $\sum_{u,v} g^2(u+x,v+y)$, are approximately constant.

Image energy density, which is defined as the ratio of the image energy over the corresponding image space, is required to keep constant over the whole image space. Otherwise the correlation between a feature in the image and its exactly match may be less than the correlation between the feature and a bright spot. Evaluation of image similarities based on Eq. (3.2) also poses a stricter requirement on the time stability of image intensities. Any fluctuation in the image intensity over time and special distribution of image energy density would cause the breakdown of Eq. (3.2) as an effective measure of similarity. To overcome this difficulty, the intensities of images are normalized before the similarity evaluation is performed. After normalization, image $f(x,y)$ becomes $\dfrac{f(x,y)-\bar{f}(x,y)}{\sqrt{\sum_{u,v}\left(f(u,v)-\bar{f}(u,v)\right)^2}}$ and image $g(x,y)$ becomes $\dfrac{g(x,y)-\bar{g}(x,y)}{\sqrt{\sum_{u,v}\left(g(u,v)-\bar{g}(u,v)\right)^2}}$.

The squared Euclidean distance of normalized images is now

$$\begin{aligned} d^2_{f,g}(x,y) &= \sum_{u,v}\left(\frac{f(u,v)-\bar{f}}{\sqrt{\sum_{u',v'}\left(f(u',v')-\bar{f}\right)^2}}-\frac{g(u+x,v+y)-\bar{g}}{\sqrt{\sum_{u',v'}\left(g(u'+x,v'+y)-\bar{g}\right)^2}}\right)^2 \\ &= 2-\frac{2\times\sum_{u,v}\left(f(u,v)-\bar{f}\right)\left(g(u+x,v+y)-\bar{g}\right)}{\sqrt{\sum_{u,v}\left(f(u,v)-\bar{f}(u,v)\right)^2\sum_{u,v}\left(g(u+x,v+y)-\bar{g}\right)^2}} \end{aligned} \quad (3.3)$$

The normalized cross-correlation term is

$$c(x,y)=\frac{\sum_{u,v}\left(f(u,v)-\bar{f}\right)\left(g(u+x,v+y)-\bar{g}\right)}{\sqrt{\sum_{u,v}\left(f(u,v)-\bar{f}\right)^2\sum_{u,v}\left(g(u+x,v+y)-\bar{g}\right)^2}} \quad (3.4)$$

which is free of temporal fluctuation of image intensities as well as spatial change of image energy densities between image *f* and image *g*. The normalized cross-correlation term $c(x, y)$ is a more robust measure of image similarity and is termed normalized cross-correlation coefficient.

To register image A to image B, both images are divided into grids, or voxels for 3D image, of the same size. For a grid in image A, normalized cross-correlation coefficients are calculated between it and all grids in image B. The grid in image B with highest normalized cross-correlation coefficient is the match of the grid in image A. Repeating the procedure for all grids in image A, the mapping between image A and image B is established.

Although the normalized cross-correlation registration has been shown to be a straightforward method for registering images, some of its drawbacks limit its application. Firstly, it is a very time consuming technique because it is a search algorithm based on a convolution calculation. The complexity of this algorithm is, therefore, $O(n^3)$ where *n* is the number of voxels in the search region. To speed up this algorithm, a fast normalized cross-correlation coefficient method was introduced by Lewis[50], replacing the time-consuming calculation of convolution with fast Fourier transformation. However, the new scheme only reduces the algorithm complexity from $O(n^3)$ to $O(n^2 \log n)$. A whole-lung image typically includes 3 million voxels. It would take weeks, if not months, to finish the registration of a whole lung through the 25 acquired scans if the images are not downsampled. Despite its poor efficiency, the normalized cross-correlation registration is

easy to implement and robust against image artifacts and distortion. It was the first registration scheme implemented during our work for verifying our model and characterizing the free-breathing motion trajectory patterns, which will be discussed in Chapter 6. Secondly, the selection of the size of the sub-image has to be customized for the image modality and content. It largely depends on the implementer's experience. If the size of the sub-image is too small, there are not enough details in the sub-image for registration; if the size of the sub-image is too large, the registration would average through non-rigid motion. Thirdly, it is difficult to determine the size of the searching region. A large searching scope will deteriorate the already poor efficiency of normalized cross-correlation registration while a small searching scope will compromise the registration's capability of capturing large motion. Therefore, a more efficient and general registration method is needed.

## 3.2 Optical Flow Registration

The optical flow registration method was introduced by Horn and Schunck[51] in 1981. Horn and Schunck related the variation of image intensities at one spatial location in the course of time to the motion of the intensity pattern at the same spatial location. The motion of the intensity pattern, now termed as optical flow, reflected the trajectory of the tracked image feature across a sequence of images. Since its first introduction, substantial research has been devoted to develop more efficient and precise algorithms to calculate the optical flow based on Horn and Schunck's algorithm. Among these algorithms, the total variation optical flow registration with $L^1$ norm in the data fidelity term (TV-$L^1$) has

achieved precise and robust optical flow estimation . Both Horn and Schnuch's original algorithm and TV-$L^1$ algorithm are discussed in the following sections.

### *3.2.1 Horn and Schunck's Algorithm*

In this algorithm, motion is detected through the flow of image intensity. Assuming the image intensity of a certain object located at point $\vec{x}$ doesn't change within a sequence of images, and denoting the image intensity of the object in the image plane and at time *t* as $E(\vec{x},t)$, we have

$$\frac{dE}{dt} = 0. \tag{3.5}$$

Applying the chain rule for differentiation, Eq (3.5) can be expanded into

$$\frac{\partial E}{\partial t} + \vec{U} \bullet \nabla E = 0, \tag{3.6}$$

where $\vec{U}$ is the space velocity of the object moving across the image sequence and $\vec{U} = \frac{d\vec{x}}{dt}$ .

In this chapter, the space velocity of the object is measured in the image frame and is also termed as the image flow or the optical flow. Since the time interval between any two registered images is always taken to be unit time, the image flow or the optical flow is equivalent to the displacement of the concerned object across the images

The image flow can be obtained from Eq (3.6),

$$\vec{U} = -\frac{E_t}{\|\nabla E\|} \tag{3.7}$$

Although any motion satisfies Eq. (3.6), the motion can not be fully recovered from the equation. Only the component that is parallel to the intensity gradient is recoverable in Eq. (3.7). The perpendicular component is lost in the inner product term. This issue is known as the aperture problem of the optical flow algorithm.

One solution to the aperture problem is to introduce additional constrains. Smoothness is the most popular option. The rationale of choosing smoothness as the additional constrain is that, the image flow doesn't move in a random and independent manner. Instead, the motions of neighboring points are assumed to be similar in both magnitude and direction. Unless the gradients of the neighboring image intensities align in the same direction, the local perpendicular component of flow with respect to the gradient of image intensity is determined from more distant points.

One way to smooth the image flow is to minimize the squared Euclidean distance of image flow gradient,

$$\sum_{i,j}\left(\frac{\partial U_i}{\partial x_j}\right)^2 \tag{3.8}$$

where *i* and *j* denote spatial components. Value of (3.8) describes the departure from smoothness. As smoothness decreases, the value of the term in (3.8) increases. The problem then turns to finding the image flow that minimizes both the sum of the residual in Eq. (3.6) and the departure from smoothness:

$$\varepsilon = \int \left( \frac{\partial E}{\partial t} + \vec{U} \bullet \nabla E \right) + \alpha^2 \sum_{i,j} \left( \frac{\partial U_i}{\partial x_j} \right)^2 dx \,. \tag{3.9}$$

The first term is the data term, also known as the optical flow constraint. The second term is a regularization term that exerts a penalty for unsmooth image flows and is known as the deviation term.

The process of determining the minimum of Eq. (3.9) is equivalent to the solving of Euler–Lagrange equation:

$$\frac{\partial L}{\partial U_i} - \sum_j \frac{\partial}{\partial x_j} \frac{\partial L}{\partial U_{ij}} = 0 \tag{3.10}$$

where $L = \frac{\partial E}{\partial t} + \vec{U} \bullet \nabla E + \alpha^2 \sum_{i,j} U_{ij}{}^2$ and $U_{ij} = \frac{\partial U_i}{\partial x_j}$.

Applying the calculus of variation on Eq. (3.10), we obtain

$$\partial_i E \left( \partial_t E + \vec{U} \bullet \nabla E \right) - \alpha^2 \Delta U_i = 0 \,, \tag{3.11}$$

where $\Delta = \sum_i \frac{\partial^2}{\partial x_i^2}$ denotes the Laplace operator. To further simplify the notations in this chapter, we define $\partial_i E \equiv \frac{\partial E}{\partial x_i}$ .and $\partial_t E \equiv \frac{\partial E}{\partial t}$

In practice the Laplacian is approximated numerically by employing the finite difference method. In this method, the image space is divided into grids (2D) or voxels (3D) in unit dimension. The integral of the Laplacian is

$$\begin{aligned} \int \Delta U dV &= \int \nabla \bullet \nabla U dV \\ &= \oint \nabla U d\vec{S} \end{aligned} \tag{3.12}$$

Confining the integral in one of the grids or voxels denoted as *i*, Eq. (3.12) is approximated by

$$\Delta U(i) \approx \kappa\left(\overline{U}(i) - U(i)\right), \tag{3.13}$$

where $\overline{U}(i)$ is the average of image flows in the neighboring grids or voxels sharing one face with grid or voxel *i*. $\kappa$ is the number of neighboring grids or voxels. A convenient approximation to calculate the average is

$$\overline{U}(i) = \sum_n \frac{U(n)}{\kappa} \tag{3.14}$$

Where *n* denotes the grid or voxel that shares one face with voxel *i*. In a 2D image,

$$\Delta U(i, j) = 4\left(\overline{U}(i, j) - U(i, j)\right) \tag{3.15}$$

where

$$\overline{U}(i, j) = \frac{1}{4}\left\{U(i+1, j) + U(i-1, j) + U(i, j-1) + U(i, j+1)\right\} \tag{3.16}$$

In a 3D image,

$$\Delta U(i, j) = 6\left(\overline{U}(i, j) - U(i, j)\right) \tag{3.17}$$

where

$$\begin{aligned}\overline{U}(i, j+k) = \quad & \frac{1}{6}\{U(i+1, j, k) + U(i-1, j, k) + U(i, j-1, k) \\ & + U(i, j+1, k) + U(i, j, k-1) + U(i, j, k+1)\}\end{aligned} \tag{3.18}$$

Eq. (3.11), after applying Eq (3.13), now reads

$$\sum_j \partial_i E U_j \partial_j E + \alpha^2 \kappa U_i = \alpha^2 \kappa \overline{U}_i - \partial_i E \partial_t E \tag{3.19}$$

Eq. (3.19) is a system of linear equations with large absolute values in each row and column dominated by the diagonal element. The Jacobi method is employed to determine the solutions. An iterative process is repeated, starting with initial guesses of solutions,

until the solutions converge. Since the solution depends on the neighboring values of the flow field, it must be repeated each time the neighbors have been updated. Therefore, the following iterative scheme is employed to estimate the image flow,

$$U_i^{k+1} = \overline{U}_i^k - \frac{\partial_i E\left(\sum_j \overline{U}_j \partial_j E + \partial_t E\right)}{\alpha^2 \kappa^2 + \|\nabla E\|^2} \tag{3.20}$$

where the superscript k+1 denotes the next iteration and k is the previously calculated result.

### *3.2.2 TV-$L^1$*

The Horn–Schunck algorithm is capable of yielding a high density of flow vector field. However, a quadratic penalization of the deviation term leads to two challenges. Firstly, discontinuities are not allowed in the displacement field. Secondly, extra small or large motions distant from the rest of the displacement fields can not be handled robustly. To overcome these limitations, several modifications to the original Horn-Schunck algorithm[51] have been proposed in the last two decades. Among them, as proposed by Zach[52], a differentiable approximation of the Total Variation with robust $L^1$ norm (TV-$L^1$) is used in the data fidelity term, which is optical flow constraint that assumes the intensity values of $I_0(x)$ do not change during its motion to $I_1(x+u(x))$.

The total variation of a real-valued function $f$ is a measure of the one-dimensional arclength of the function as described using a parametric equation. In mathematics, the total variation *TV* is defined as

$$TV(f) = \int_{\Omega} |\nabla f| dx . \tag{3.21}$$

If $f$ is monotonic in [a, b], then TV($f$) =|$f$(b)-$f$(a)|, regardless of whether or not $f$ is discontinuous. Since discontinuities in the optical flow appear often in conjunction with high image gradients, penalization on the total variation would control both the sizes of jumps between discontinuities and geometry of boundaries. TV-$L^1$ has advantages over .the Horn–Schunck algorithm, both in precision and robustness.

The objective of the *TV-$L^1$* optical flow registration algorithm is to find the image flow $\vec{U}$ which minimizes the residual that is contributed by a total variation regularization term and a robust $L^1$ norm in the data fidelity term that is similar to what we described in the Horn and Schunck's algorithm. Mathematically, the image flow $\vec{U}$ is the minimizer of

$$\int \left\{ \lambda \left( \partial_t E + \vec{U} \bullet \nabla E \right) + \sum_i |\nabla U_i| \right\} d\vec{x} \tag{3.22}$$

where $\left( \partial_t E + \vec{U} \bullet \nabla E \right)$ represents the image data fidelity and $\sum_i |\nabla U_i|$ is the regularization term. $\lambda$ weighs between the data fidelity term and the regularization term that smoothes the displacement fields.

A dual formulation of Eq. (3.22) is introduced to achieve an efficient and globally convergent solution. In this scheme, Eq. (3.22) is minimized separately in the data fidelity and regularization terms by introducing an auxiliary variable $\vec{V}$ ,

$$\int\left\{\lambda\left(\partial_t E+\vec{V}\bullet\nabla E\right)+\sum_i|\nabla U_i|\right\}d\vec{x} \tag{3.23}$$

In the following paragraphs, we denote the fidelity term $\left(\partial_t E+\vec{V}\bullet\nabla E\right)$ by $\rho(\vec{V})$.

An additional constraint term, $\frac{1}{2\theta}\left\|(\vec{U}-\vec{V})\right\|^2$, is introduced to make sure the image flows, which are minimized in the two terms $\vec{U}$ and $\vec{V}$, converge at approximately the same pace. Eq. (3.23) now reads as:

$$\int\left\{\lambda\rho(\vec{V})+\frac{1}{2\theta}\left\|(\vec{U}-\vec{V})\right\|^2+\sum_i|\nabla U_i|\right\}d\vec{x} \tag{3.24}$$

$\theta$ is a very small constant to guarantee sufficient approximation between $\vec{U}$ and $\vec{V}$, which are minimized independently as depicted below.

1 Minimization of the regularization term

$$\min\int\left\{\frac{1}{2\theta}\left\|(\vec{U}-\vec{V})\right\|^2+\sum_i|\nabla U_i|\right\}d\vec{x} \tag{3.25}$$

2. Minimization of the fidelity term

$$\min\int\left\{\frac{1}{2\theta}\left\|(\vec{U}-\vec{V})\right\|^2+\lambda\rho(\vec{V})\right\}d\vec{x} \tag{3.26}$$

The solution of Eq. (3.25) is given by

$$\vec{U}=\vec{V}-\theta\nabla\vec{\vec{P}} \tag{3.27}$$

where $\vec{\vec{P}}$ is a tensor of $N\times N$ and $N$ is the dimension of $\vec{U}$. $\vec{\vec{P}}$ can be solved iteratively using the following equation,

$$P_{i,j}^{k+1} = \frac{\vec{P}_{i,j}^{k} + \tau \frac{\partial}{\partial x_i}\left(\sum_i \frac{\partial P_{i,j}^{k}}{\partial x_i} - \frac{V_j}{\theta}\right)}{1 + \tau\sqrt{\sum_j \left(\frac{\partial}{\partial x_i}\left(\sum_i \frac{\partial P_{i,j}^{k}}{\partial x_i} - \frac{V_j}{\theta}\right)\right)^2}} \tag{3.28}$$

where $k$ is the iterative step and $P^0 = 0$. $\tau$ is the time step which controls the convergence speed.

The solution of Eq. (3.26) is given by the following threshold step:

$$V_i = U_i + \begin{cases} \lambda\theta\sum_j \frac{\partial}{\partial x_j}\frac{\partial E}{\partial x_i} & if \quad \rho(U_i) < -\lambda\theta\sum_j \left(\frac{\partial}{\partial x_j}\frac{\partial E}{\partial x_i}\right)^2 \\ -\lambda\theta\sum_j \frac{\partial}{\partial x_j}\frac{\partial E}{\partial x_i} & if \quad \rho(U_i) > \lambda\theta\sum_j \left(\frac{\partial}{\partial x_j}\frac{\partial E}{\partial x_i}\right)^2 \\ -\rho(U_i)\sum_j \frac{\partial}{\partial x_j}\frac{\partial E}{\partial x_i} \Big/ \sum_j \left(\frac{\partial}{\partial x_j}\frac{\partial E}{\partial x_i}\right)^2 & if \quad |\rho(U_i)| \le \lambda\theta\sum_j \left(\frac{\partial}{\partial x_j}\frac{\partial E}{\partial x_i}\right)^2 \end{cases} \tag{3.29}$$

The implementation of this scheme is quite simple. Given two images $I_0$ and $I_1$ of any dimensions (2D or 3D),

1. Start with iterative step k=0

2. Set the image flow $U$ =0. Also set $V = 0$ and $\vec{P} = 0$

3. Calculate the image fidelity $\rho$ using $\rho(\vec{U}) = \partial_t E + \vec{U} \bullet \nabla E$

4. Calculate $V^k$ using Eq. (3.29)

5. Calculate $\vec{P}^{k+1}$ using Eq. (3.28)

6. Update $U^{k+1}$ using Eq. (3.27)

7. Update k with k+1

8 Go to step3 and repeat

## 3.3 Model Fitting

After registering the images to obtain the lung tissue motion positions for each acquired image, the images are correlated against the tidal volumes and airflows at the times the images were acquired. The motion model parameters are fit by minimizing the residual of the model equation (1.1),

$$\min_{\vec{X}_0,\vec{\alpha},\vec{\beta}\in\Re^3} \sum_i \left\| \vec{X}_i - \vec{X}_0 - \vec{\alpha} v_i - \vec{\beta} f_i \right\|$$

where $\vec{X}_i$ was the $i^{th}$ location of the registrations, and $v_i$ and $f_i$ were the tidal volume and airflow, respectively, for scan $i$. To recover 3 undetermined model parameter vectors, $\vec{X}_0$, $\vec{\alpha}$ and $\vec{\beta}$, at least 3 images acquired at different pairs of tidal volume and airflow are required. However, because of the image artifacts occurring during the acquisition and registration noises, more than 3 images are needed to recover the model parameters with a higher confidence. Therefore, the determination of the model parameters turn to approximating the solutions for an overdetermined system in which there are more equations than unknowns. In this chapter, we define the process of finding optimal solutions to an overdetermined system as the fitting process.

Two optimization techniques have been implemented so far. One is Linear Least-Square method and another is nonlinear Nelder–Mead method. The implementation of both techniques is discussed in the following section.

### *3.3.1 Linear Least-Square Optimization*

Least-square optimization was first introduced by Carl Gauss around 1794 to study the motion of heavenly bodies. In this method, a residual is defined as the difference between the observed positions (or the registered positions) and the predicted positions from the model. The goal of fitting is to optimize the model parameters to minimize the residuals.

The lung motion model discussed in this dissertation is a regression model that is a linear combination of parameters. In mathematics, it can be expressed concisely with matrix operations,

$$X = PS \tag{3.30}$$

where $X$ is the tissue trajectory. $P$ is the matrix of the model parameters and $S$ is the matrix containing the surrogates that include tidal volume and air flow. $X$ , $P$ and $S$ are specifically defined as the following

$$X = \begin{bmatrix} x_1 & x_2 & \dots & x_N \\ y_1 & y_2 & \dots & y_N \\ z_1 & z_2 & \dots & z_N \end{bmatrix} \tag{3.31}$$

$$P = \begin{bmatrix} X_{0x} & \alpha_x & \beta_x \\ X_{0x} & \alpha_y & \beta_y \\ X_{0x} & \alpha_z & \beta_z \end{bmatrix} \tag{3.32}$$

and

$$S = \begin{bmatrix} 1 & 1 & \dots & 1 \\ V_1 & V_2 & \dots & V_N \\ f_1 & f_2 & \dots & f_N \end{bmatrix} \tag{3.33}$$

where $N$ is the number of the acquisitions per couch position.

The residual between the observed position and the predicted position from the model is written in matrix form as the following,

$$R = X_{ob} - PS \tag{3.34}$$

Please notice that in this equation $X$ is replaced by $X_{ob}$, which denotes the observed position. The sum of the residual squares is given by the Frobenius inner product,

$$L = \left(X_{ob} - PS\right) : \left(X_{ob} - PS\right)^T \tag{3.35}$$

where the operator : donotes the Frobenius inner product which, for two matrixes A and B with equal size, gives

$$A : B = \sum_i \sum_j A_{ij} B_{ij} \tag{3.36}$$

The Frobenius inner product of matrixes can be equivalently transferred to trace operation of the matrix multiplication. Hence Eq. (3.35) can be rewritten as

$$L = Tr\left\{\left(X_{ob} - PS\right)\left(X_{ob} - PS\right)^T\right\} \tag{3.37}$$

where the Frobenius inner product is replaced by the normal matrix multiplication in the trace operation.

The minimum of the sum of squares is found at one point where the derivative of the sum of squares with respect to the unknown parameters equals zero.

$$\begin{aligned} \frac{\partial L}{\partial P} &= \frac{\partial Tr\left\{\left(X_{ob} - PS\right)\left(X_{ob} - PS\right)^T\right\}}{\partial P} \\ &= \frac{\partial Tr\left\{X_{ob}X_{ob}^T - X_{ob}S^TP^T - PSX_{ob}^T + PSS^TP^T\right\}}{\partial P} \\ &= 0 - SX_{ob}^T - SX_{ob}^T + SS^TP^T + SS^TP^T + (SS^T)^TP^T \\ &= -2SX_{ob}^T + 2SS^TP^T \\ &= 0 \end{aligned} \tag{3.38}$$

Therefore, we obtain the parameters in our lung motion model, which is an overdetermined system, in a closed form.

$$P^T = (SS^T)^{-1} SX_{ob}^T \tag{3.39}$$

or

$$P = X_{ob} S^T \left(SS^T\right)^{-1} \tag{3.40}$$

### *3.3.2 Nelder–Mead Optimization*

Although least-square optimization is by far the most popular method to estimate the unknown model parameter, some disadvantages of this method limit its application. Firstly, least-square optimization only works for linear models whose parameter derivatives are available. Secondly, the matrix used in least-square optimization must be non-singular in order to obtain meaningful results. For example, if we prospectively gate the breathing and scan the patient only at end of exhalation and end of inhalation, the airflow would be zero for all the data acquired. In that case, $SS^T$ would be a singular matrix and the inverse of the singular matrix would become meaningless. Thirdly, although we model lung motion during quite respiration using a linear function, in the future we would like to add more terms into our model, especially cross terms of tidal volume and airflow. A motion model with cross terms would be nonlinear and the linear least-square optimization would be no longer applicable. Therefore, we need an optimization method that could be applied to a broader range of situations.

Nelder-Mead optimization [53] is one of the most popular non-derivative algorithms. The word "*non-derivative algorithm*" here means broadly that it uses only function values

(comparing to least-square optimization) and does not implicitly try to approximate the gradient (comparing to finite-difference optimization).

The biggest advantage of a non-derivative algorithm against a derivative algorithm is that, the non-derivative algorithm does not require additional coding to evaluate derivatives, which are usually the major source of errors. This advantage, in addition to simplicity, boosts the popularity of Nelder-Mead optimization among users, despite its relatively lower efficiency.

Nelder-Mead optimization is carried out on simplexes, which are constructed by the model parameters to be fit. In the field of geometry, a simplex is a generalized notion of a triangle or tetrahedron in arbitrary dimensions. Specifically, an n-simplex is an n-dimensional polytope with n + 1 vertices, of which the simplex is the convex hull. For example, a 2-simplex is a triangle, a 3-simplex is a tetrahedron, and a 4-simplex is a pentachoron. A single point may be considered a 0-simplex, and a line segment may be viewed as a 1-simplex. A simplex may be defined as the smallest convex set which contains the given vertices.

The method approximates a local optimum of a problem with N undetermined parameters. For example, the purpose of fitting our lung motion model is to look for an optimal set of parameters as $\vec{\alpha}$ $\vec{\beta}$ and $\vec{X}_0$ that together determine the lung tissue motion. It is clear that the motion is a combination of contributions from all parameters, but it is not easy to visualize the impact of changing any specific element. In this case, we use the Nelder–

Mead method to generate trial motions and test them. Each round of tests will tell us if we should keep looking in the same direction in optimizing the model parameters or we are heading towards a dead end and should change direction.

Initially, one constructs an N-simplex with N+1 vertices. For a two parameter problem, a 2-simplex is constructed with 3 vertices, which is simply a triangle. However, the construction of an initial simplex is more complex for our lung motion mode since the model has 3 undetermined parameters, each of which has 3 independent spatial components. To proceed with 9 variables, a 9-simplex is constructed at the very beginning of the optimization. All the vertices or points in the simplex are used to test the possibility of finding an optimal solution, therefore, they are called test points or test simplex.

After the construction of the initial simplex, a new test point is generated by extrapolating the behavior of the objective function measured at each test point in the current test simplex. The algorithm then chooses to replace one of these test points with the new test point and so the process continues to evolve. The simplest step is to replace the worst point with its mirror point that reflects through the center of gravity of the remaining N points. The center of gravity here is defined as a simple average of the positions of all test points. If the new point is better than the best current point by giving a lower evaluation of the objective function, the next iteration will extend along the same direction. On the other hand, if this new point isn't much better than the previous value, it is possible that a minimum was crossed. Sampling an intermediate point would then be attempted.

There are many variations of the Nelder–Mead method, with variations depending on the nature of the problem to solve. Steps of one Nelder–Mead algorithm are listed as the following:

Given: $N$+1 vertices $x_i$, $i$=1…$N$+1, of a $N$-simplex, a model presented by a function $f(x_i), i = 1...N+1$ ,and coefficient $\rho$ (reflection), $\chi$ (expansion), $\gamma$ (contraction) and $\sigma$ (shrinkage). In a standard implement of Nelder-Mead algorithm, $\rho = 1$, $\chi = 1$, $\gamma = 0.5$ and $\sigma = 0.5$

1**. Initialization.** For a model with N undetermined parameters, choose N+l points. Evaluate the model at each point (vertex) of the simplex.

2. **Sort by model value.** Sort the values at the vertices to satisfy

$$f(x_1) \leq \cdots \leq f(x_N) \leq f(x_{N+1}) \tag{3.41}$$

3. **Localization** of the gravity center. Calculate the gravity center of all points in the simplex except the one that is going to be replaced (N+1).

$$\bar{x} = \sum_{i=1}^{N} x_i \tag{3.42}$$

4. **Reflection**. Computer the mirror point of the worst point by reflecting through the center of gravity

$$x_r = \bar{x} + \rho(\bar{x} - x_{N+1}) \tag{3.43}$$

Comparing the evaluation of the function at the new point to those at points in the simplex except the worst one, if $f(x_1) \leq f(x_r) < f(r_N)$ , the new point is better in minimizing the function than at least one point in the simplex and also worse than at least

one point. This indicates that optimization toward $x_r$ is probably in the right direction, but the room for further improvement is limited. Therefore, $x_r$ will be accepted to replace the worst point and continue to step 2.

5. **Expansion**. . If $f(x_r) < f(x_1)$, the reflected point is the best point so far. This indicates that optimization towards $x_r$ is very promising and the room for further improvement is beyond detection so far. Instead of keeping $x_r$ and replacing the worst point like step 4, a more aggressive exploration is tried in the direction suggested by $x_r$.

$$x_e = \bar{x} + \chi(\bar{x} - x_{N+1}) \tag{3.44}$$

If the expanded point is better than the reflected point, $f(x_e) < f(x_r)$, the worst point in the simplex is replaced by the expanded point. Otherwise, the worst point in the simplex is replaced by the reflected point. Continue to step 2 after the replacing.

6. **Contraction**. If $f(x_r) \geq f(x_N)$, the reflection appears too aggressive to obtain any gain over current points. A contraction between $\bar{x}$ and the better of $x_N$ and $x_{N+1}$ is performed.

a. **Outside**. If $f(x_N) \leq f(x_r) < f(x_{N+1})$, calculate

$$x_c = \bar{x} + \gamma(x_r - \bar{x}) \tag{3.45}$$

If $f(x_c) \leq f(x_r)$, replace $x_{N+1}$ with $x_c$ and proceed to step 2; otherwise proceed to step 7 for a shrinkage.

b. **Inside**. If $f(x_r) \geq f(x_{N+1})$, calculate

$$x_c = \bar{x} + \gamma(x_{N+1} - \bar{x}) \tag{3.46}$$

If $f(x_c) \le f(x_{n+1})$, replace $x_{N+1}$ with $x_c$ and proceed to step 2; otherwise proceed to step 7 for the shrinking.

7. **Shrink**. In this case, all the attempts to find a better point outside of the region enclosed by the simplex have failed. The simplex has to shrink to proceed. All the points are shrunk to new points.

$$x_i^{'} = x_1 + \sigma(x_i - x_1) \tag{3.47}$$

where $i = 1, \cdots, N+1$. The points of the simplex are replaced by the new points and continue to step 2.

The Nelder-Mead algorithm is known for its inefficiency. A lot of effort has been put into a mathematical analysis of the simple steps above with little progress. However the Nelder-Mead algorithm is a simple and straightforward method for global optimization. It has been used to solve a remarkable number of difficult optimization problems. We used the Nelder-Mead algorithm in this study to examine the free breathing patterns. A retrospective study also showed that the fitting results from Nelder-Mead algorithm are slightly better than those from the least-square optimization, in addition to its capability to optimize a potential nonlinear equation that we would like to expand our model to in the future, if necessary.

# Chapter 4

# Verification of The Lung Motion Model

## 4.1 Introduction

The free-breathing lung motion model we discuss in this dissertation hypothesized that the breathing motion of lung tissues and lung tumors can be modeled as a function of 5 independent parameters, which are the tidal volume, the airflow and 3 independent spatial components of the tissue's initial position at the reference condition of zero tidal volume and zero airflow. The tidal volume metric is a surrogate for the general inhalation and exhalation motion while the airflow is a surrogate for the hysteresis behavior. Hysteresis is defined as the variation between trajectories during inhalation and exhalation. The magnitude of hysteresis was observed to be minimal at the beginning of inhalation or the end of exhalation, while maximal at mid-inhalation and mid-exhalation. This observation provided the rationale to model the hysteresis with airflow.

This model was formulated such that the volume and airflow were functions of time, rather than have time as an explicit variable in the model. Excluding the time dependence

explicitly from the model equation allows the complex time dependence to reside within the variables rather than explicitly within the model equation.

In this chapter, some of the consequences of the model will be examined and the predictions will be validated with patient data.

## 4.2 Materials and Methods

### 4.2.1 Derivation of Divergence Relationship

The breathing motion model was proposed with a linear relationship between tidal volume, airflow and the subsequent tissue displacement. The position $\vec{X}$ of tissue was modeled as

$$\vec{X}(v, f : \vec{X}_0) = \vec{X}_0 + \vec{\alpha}(\vec{X}_0)V + \vec{\beta}(\vec{X}_0)f \qquad (4.1)$$

where $\vec{X}_0$ was the position of tissue under the conditions of tidal volume $V = 0$ and airflow $f = 0$, $\vec{\alpha}(\vec{X}_0)$ characterized the displacement of lung tissues from air filling and $\vec{\beta}(\vec{X}_0)$ characterized the hysteresis motion. $\vec{\alpha}$ had units of distance per tidal volume (mm $l^{-1}$ in this work) and $\vec{\beta}$ had units of distance per airflow (mm s $l^{-1}$ in this work). Eq. (4.1) does not have time explicitly included. The time dependence is imbedded in *V* and *f*. This first-order model was assumed to accurately represent breathing motion under the conditions of quiet respiration which was typically characterized by smooth changes in

tidal volume and airflow. In this model, the physical processes that were modeled by the tidal volume and airflow were assumed to be independent of one another, so the hysteresis behavior occurred independently of lung filling. For example, if the hysteresis component of motion for a specific piece of tissue (located at $\vec{X}_0$) was $\vec{\beta}\left(\vec{X}_0\right)$, the hysteresis motion was the same whether the tidal volume was at inhalation or exhalation or in between.

The model accuracy has been studied by Low et al[54] and investigations are ongoing to evaluate the consistency of model parameters both in the case of irradiated and unirradiated lungs.

The objective of this chapter is to examine whether the model behaves correctly when applied to the continuity equation. The continuity equation states that the relationship between a velocity field $\vec{U}$ and density $\rho$ is:

$$\vec{\nabla} \bullet \rho\vec{U} = -\frac{\partial \rho}{\partial t} \tag{4.2}$$

where *t* is time and the velocity vector field is $\vec{U} = d\vec{X}/dt$. Expanding the left side of Eq. (4.2)

$$\vec{\nabla}\rho \bullet \vec{U} + \rho\vec{\nabla} \bullet \vec{U} = -\frac{\partial \rho}{\partial t} \tag{4.3}$$

The equation states that the change in lung tissue density at a point in space is due to two causes presented by two terms on the left side of Eq. (4.3). The first term is the inner product of the gradient of the tissue density and the tissue velocity. When there is a gradient in the tissue density and the tissue moves past the point of observation, the

density at the point of observation will change in time. The second term describes the change in density due to expansion or contraction of the velocity field. The local expansion and contraction of lung tissue is likely to be a physiologically relevant quantity to study, so the first term is subtracted from both sides of the equation. This results in

$$\rho\vec{\nabla}\bullet\vec{U} = -\frac{d\rho}{dt} \tag{4.4}$$

In the proposed breathing motion model, time was not the dependent variable, so the chain rule was employed to change the variable from *t* to *V* and *f* yielding terms with the derivative $df/dt$. In order to simplify the equation, the constraint of a constant airflow $df/dt = 0$ was applied. This yielded

$$\rho\frac{dV}{dt}\left\{\frac{\partial}{\partial x}\frac{\partial x}{\partial V}+\frac{\partial}{\partial y}\frac{\partial y}{\partial V}+\frac{\partial}{\partial z}\frac{\partial z}{\partial V}\right\} = -\frac{\partial\rho}{\partial V}\frac{dV}{dt} \tag{4.5}$$

Eq. (4.1) shows the relationship between the tidal volume, the airflow, and the tissue position. Taking the partial derivatives of the position vectors and dividing both sides by $\rho\, dV/dt$ leads to

$$\vec{\nabla}\bullet\vec{\alpha} = -\frac{1}{\rho}\frac{\partial\rho}{\partial V} \tag{4.6}$$

where the equation is valid under conditions of constant airflow. This equation was obtained by dividing both sides by $\rho\, dV/dt$, so in principal it is not valid when either the density or the airflow is zero, but it is valid in the limit that the density or airflow approach zero.

### 4.2.2 Evaluation Equations

Eq. (4.6) showed that under conditions of constant airflow, the relative local density changed as a function of tidal volume by an amount equal to the divergence of the $\vec{\alpha}$ field. The hypothesis was that the local density variation as a function of inhaled tidal volume, and consequently $\vec{\alpha}$, would remain consistent with time (days or weeks) if the lungs were not affected by disease or treatment intervention such as radiation therapy.

Measuring the local density change directly from CT scans acquired during free breathing would normally be challenging due to the complex hysteresis motion during respiration. However, with the approach proposed by Low et al[1], the position of the tissues in the individual free breathing CT scans could be correlated against the tidal volumes and airflows to generate the model parameters $\vec{\alpha}$ and $\vec{\beta}$. According to Eq. (4.6), the divergence of $\vec{\alpha}$ provided the relative density variation as though the patient had breathed infinitely slowly (consistent with the constant airflow restriction) so that hysteresis effects were not present.

While Eq. (4.6) provided the potential for examining the lung density variations, a validation of the equation would provide a powerful validation of the 5D model and its consequences. The left side of Eq. (4.6) was integrated throughout the lungs so Gauss's law could be used to convert the integral to a surface integral

$$\int_V \vec{\nabla} \bullet \vec{\alpha}\, dV = \oint_S \vec{\alpha} \bullet d\vec{S} \tag{4.7}$$

where the integral on the left of Eq. (4.7) would be conducted throughout the entire lung volume *V* through volume elements *dV*, and the surface integral on the right would be conducted on the lung surface $\vec{S}$ through surface area elements $d\vec{S}$, which represented an infinitesimal surface area element whose direction was normal to the lung surface.

The term on the right could be expressed as

$$\oint_S \vec{\alpha} \bullet d\vec{S} = \oint \frac{\vec{X}(v,\, f : \vec{X}_0) - \vec{X}_0 - \vec{\beta}(\vec{X}_0)\, f}{V} \bullet d\vec{S} \tag{4.8}$$

At end of inhalation and exhalation, the airflow equals zero. At these two phases, Eq. (4.8) became

$$\oint \vec{\alpha} \bullet d\vec{S} = \frac{1}{V} \oint \left( \vec{X}(v,\, f = 0 : \vec{X}_0) - \vec{X}_0 \right) \bullet d\vec{S} \tag{4.9}$$

$\vec{X}(v,\, f = 0 : \vec{X}_0) - \vec{X}_0$ was the displacement vector of an infinitesimal surface element on the lung, its vector product with the surface area was the change of lung volume through the infinitesimal surface. The integral of the displacement over the whole lung boundary gave the total change of lung volume due to respiration at end of inhalation. The ratio of lung volume change to the tidal volume had been established to be 1.11[55], the ratio of room air to lung air densities. Therefore,

$$\oint \vec{\alpha} \bullet d\vec{S} = 1.11 \tag{4.10}$$

Using Gauss' law, Eq. (4.10) became

$$\int_V \vec{\nabla} \bullet \vec{\alpha}\, dV = 1.11 \tag{4.11}$$

Eq. (4.11) provided a useful test metric for the motion model. It indicated that for every patient and every 4DCT scan session, the integral of the divergence of $\vec{\alpha}(\vec{X}_0)$ must be 1.11.

The value of $\vec{\beta}(\vec{X}_0)$ was tested in a similar way. $\vec{\beta}$ related motion to airflow, which in the breathing motion model was assumed to be proportional to internal pressure imbalances that occurred during the act of inhalation and exhalation. Similar to the analysis of Eq. (4.7) where the surface integral of $\vec{\alpha}$ described the inflation of the lungs, the surface integral of $\vec{\beta}$ also described lung inflation, this time due to hysteresis. Because lung inflation due to changes in tidal volume was modeled by $\vec{\alpha}$, the lung inflation due to hysteresis should have been negligible, but unlike Eq. (4.10), integrating the divergence of $\vec{\beta}$ did not provide a unitless quantity (it had a unit of time), so interpretation of the results would have been difficult. Instead, the *ratio* of surface integrals of $\vec{\beta}$ to $\vec{\alpha}$ was defined, multiplying each integral by the maximum airflow $f_{\max}$ and tidal volume $V_{\max}$. The surface integrals described the integrated rate of inflation. Multiplying the rate of inflation by the appropriate variable would yield the total inflation. For example, $\vec{\alpha}$ was calculated in units of distance per tidal volume, so multiplying by the surface integral by tidal volume gave the expansion at the lung surface at the maximum tidal volume. Similarly, $\vec{\beta}$ was calculated in units of distance per airflow, so multiplying by the maximum airflow gave the amount of lung inflation due to the hysteresis component. The ratio, defined as *R*, compared the maximum volume expansion for these components.

$$R \equiv \frac{f_{\max}}{V_{\max}} \frac{\oint \vec{\beta} \bullet d\vec{S}}{\oint \vec{\alpha} \bullet d\vec{S}} \tag{4.12}$$

The motion model predicted that the influence of tidal volume and airflow mechanics were independent, and that the inflation was predicted by the volume component, so the $\vec{\beta}$ component, and consequently the ratio *R* should have been equal to zero. The ratio of $\frac{V_{\max}}{f_{\max}}$ can be found in Tab. (4.1) for all patients enrolled in this study. The surface integral in the denominator of Eq. (4.12) was provided in Eq. (4.10). Applying Gauss's law to the numerator

$$R = \frac{\int_V \vec{\nabla} \bullet \vec{\beta} dV}{1.11 \times \frac{V_{\max}}{f_{\max}}} \tag{4.13}$$

Like Eq. (4.11), this provided a test of the model parameter, in this case $\vec{\beta}(\vec{X}_0)$.

### 4.2.3 Evaluation Method

Eq. (4.11) and Eq. (4.13) were evaluated using clinical data from 35 patients. These patients were scanned using a 16-slice CT (Philips Brilliance) scanner operated in ciné mode (spatial resolution: 0.98x0.98x1.5 $mm^3$) with 25 scans acquired contiguously at each 24 mm wide couch position. Two external respiratory measurements were simultaneously acquired; tidal volume measured using a spirometer (VMM-400, Interface Associates), and a bellows pressure signal measured using a pneumatic belt system that was wrapped around the abdomen. The bellows pressure measurement was correlated

with the spirometry measurement to provide the tidal volume and airflow at each scan. Lu et al[56] described this technique.

The tissue positions were mapped for each scan using the normalized cross-correlation. The scan with tidal volume closest to zero ml (defined as the 5$^{th}$ percentile tidal volume) was employed as the reference scan. The remaining scans were sorted by tidal volume and categorized into whether they were acquired during inhalation or exhalation. The position matching was performed in the inhalation and exhalation category separately, ordered by increasing tidal volume and using the reference scan as the initial guess for the first operation in each category. The result from each match was used as the initial guess for the next match in the tidal volume order.

After the positions were mapped, the values of $\vec{\alpha}$, $\vec{\beta}$, and $\vec{X}_0$ were fit by minimizing the least squares difference of the predicted (Eq. (4.1)) and measured positions. The integrals of the divergences in Eq. (4.11) and Eq. (4.13) were computed and the results used to evaluate the model quality.

## 4.3 Results

Of the 35 datasets, 18 were from lung cancer patients and 17 were from non-lung cancer patients. Tab. (4.1) lists the maximum tidal volume and airflow. The mean ratio of maximum airflow to tidal volume was $V_{\max} / f_{\max} = 1.19s \pm 0.45s$.

Tab. (4.2) and Tab. (4.3) list the results of Eq. (4.11) and Eq. (4.13) for each patient, respectively. According to Eq. (4.11), the prediction of $\int_V \vec{\nabla} \bullet \vec{\alpha}\, dV$ was 1.11 while the mean measured value was $1.06 \pm 0.14$. Fig. (4.1) shows a histogram of the values of $\int_V \vec{\nabla} \bullet \vec{\alpha}\, dV$ for the 35 patients. The predicted and mean measured values agreed within 5% and the spread of the results was relatively narrow.

The prediction of $R$ was 0. Fig. (4.2a) shows a histogram of the values of $R$ for the 35 patients. The average value was $0.017 \pm 0.027$. Fig. (4.2b) shows a histogram of the values of $R$ for 17 non-lung cancer patients with average value at 0.007±0.021. Fig. (4.2c) shows a histogram of the values of $R$ for 18 lung cancer patients with an average value at 0.028±0.029. All the results are very close to the prediction of 0.

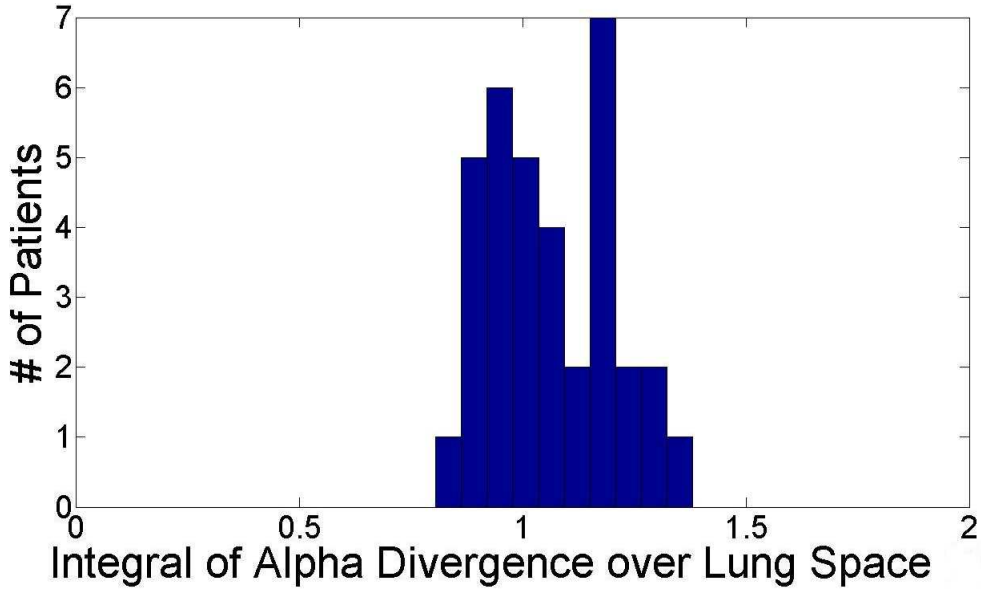


Figure 4.1: Histogram of the integral of $\int_V \vec{\nabla} \bullet \vec{\alpha}\, dV$ for the 35 evaluated patient scans, predicted to be 1.11 according to Eq. (4.11)

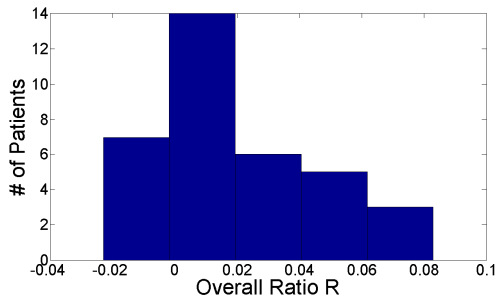


(a)

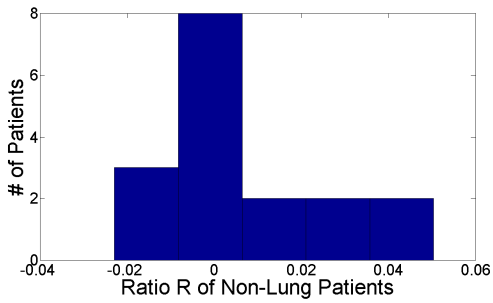


(b)

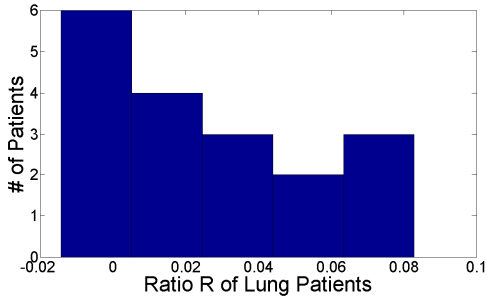


(c)

Figure 4.2: (a) Histogram of

$$R = \frac{\int_V \vec{\nabla} \bullet \vec{\beta} dV}{1.11 \times \frac{V_{\max}}{f_{\max}}}$$ for 35 patients. (b) Histogram of $R$ in non-lung cancer patients.(c) Histogram of $R$ in lung cancer patients

## 4.4 Discussion

Although Fig. (4.2) and Tab.(4.3) show that the $R$ ratios of both lung cancer and non-lung cancer patients are very close to the prediction of 0, the results from non-lung cancer patients, whose lung are assumed to function more normally than lung cancer patients', lie closer to the prediction, indicting that the motion model may be more robust for non-lung cancer patients.

Both of the motion model quantitative evaluations showed that the predictions of the model agreed well with clinical data. The overall utility of the motion model will

ultimately be tested by repeated testing in patients, but the data shown here have provided significant evidence to the model's validity.

The reason that this analysis was possible was that the motion model used tidal volume and its time derivative airflow as the motion metrics and as independent variables. Most published breathing motion studies or models have used metrics such as abdomen height or a belt wrapped around the abdomen, neither of which provided a physiologic metric that could be used to provide independent verification of a motion model. The use of tidal volume and airflow allowed the model predictions to be validated, in this case using the continuity equation.

| | Lung Patients | | | Non-Lung Patients | | |
|---|---|---|---|---|---|---|
| | $V_{max}$ (l) | $f_{max}$ (l/s) | $V_{max}/f_{max}$ (s) | $V_{max}$ (l) | $f_{max}$ (l/s) | $V_{max}/f_{max}$ (s) |
| 1 | 497.9 | 556.9 | 0.89 | 587.3 | 521.1 | 1.13 |
| 2 | 480.0 | 626.0 | 0.77 | 982.4 | 412.2 | 2.38 |
| 3 | 271.4 | 412.1 | 0.66 | 630.9 | 513.7 | 1.23 |
| 4 | 358.8 | 372.3 | 0.96 | 472.1 | 288.3 | 1.64 |
| 5 | 256.4 | 315.6 | 0.81 | 463.3 | 461.9 | 1.00 |
| 6 | 630.5 | 653.2 | 0.97 | 615.9 | 281.2 | 2.19 |
| 7 | 317.1 | 556.9 | 0.57 | 528.2 | 432.5 | 1.22 |
| 8 | 411.4 | 359.1 | 1.15 | 541.5 | 508.3 | 1.07 |
| 9 | 399.1 | 367.0 | 1.09 | 633.7 | 550.9 | 1.15 |
| 10 | 449.0 | 461.9 | 0.97 | 398.2 | 318.7 | 1.25 |
| 11 | 318.3 | 472.3 | 0.67 | 404.4 | 305.6 | 1.32 |
| 12 | 408.0 | 332.4 | 1.23 | 308.8 | 302.8 | 1.02 |
| 13 | 409.1 | 416.9 | 0.98 | 1438.7 | 611.1 | 2.35 |
| 14 | 459.0 | 402.5 | 1.14 | 335.7 | 356.1 | 0.94 |
| 15 | 848.9 | 699.4 | 1.21 | 523.9 | 443.8 | 1.18 |
| 16 | 557.9 | 321.6 | 1.73 | 569.1 | 425.5 | 1.34 |
| 17 | 971.0 | 510.0 | 1.90 | 240.0 | 349.7 | 0.69 |
| 18 | 546.6 | 595.7 | 0.92 | | | |
| | | | | | | |
| Mean | | | 1.03 | | | 1.36 |
| VAR | | | 0.12 | | | 0.25 |
| STD | | | 0.34 | | | 0.49 |
| Overall | | | | | | |
| Mean | 1.19 | | | | | |
| VAR | 0.20 | | | | | |
| STD | 0.45 | | | | | |

Table 4.1. $\frac{V_{max}}{f_{max}}$ of all the patients

| | Lung Patient | Non-Lung Patient |
|---|---|---|
| 1 | 1.1887 | 1.0760 |
| 2 | 1.2032 | 1.1603 |
| 3 | 1.2758 | 0.9676 |
| 4 | 0.9277 | 0.8884 |
| 5 | 1.2167 | 1.0996 |
| 6 | 1.0256 | 1.2387 |
| 7 | 1.0820 | 1.0813 |
| 8 | 1.2077 | 1.0071 |
| 9 | 0.9413 | 1.1072 |
| 10 | 0.9113 | 0.9175 |
| 11 | 1.2744 | 1.2023 |
| 12 | 0.9422 | 1.1597 |
| 13 | 1.0445 | 0.8056 |
| 14 | 1.3814 | 1.0154 |
| 15 | 0.9219 | 1.0313 |
| 16 | 0.8686 | 1.1724 |
| 17 | 0.8988 | 0.9649 |
| 18 | 1.0050 | |
| | | |
| Mean | 1.0732 | 1.0526 |
| VAR | 0.1591 | 0.1189 |
| STD | 0.0239 | 0.0141 |
| Overall | | |
| Mean | 1.0632 | |
| VAR | 0.0194 | |
| STD | 0.1393 | |

Table 4.2. Integral of $\int_V \vec{\nabla} \bullet \vec{\alpha}\, dV$ conducted over both lungs

| | Lung Patient | Non-Lung Patient |
|---|---|---|
| 1 | 0.0760 | 0.0503 |
| 2 | 0.0653 | 0.0504 |
| 3 | 0.0178 | -0.0029 |
| 4 | -0.0004 | -0.0181 |
| 5 | 0.0244 | -0.0016 |
| 6 | 0.0093 | -0.0004 |
| 7 | 0.0348 | 0.0034 |
| 8 | 0.0428 | -0.0011 |
| 9 | 0.0023 | -0.0041 |
| 10 | 0.0829 | 0.0116 |
| 11 | 0.0515 | 0.0322 |
| 12 | 0.0027 | -0.0229 |
| 13 | -0.0142 | -0.0014 |
| 14 | 0.0497 | 0.0070 |
| 15 | 0.0326 | 0.0265 |
| 16 | 0.0007 | 0.0061 |
| 17 | -0.0025 | -0.0102 |
| 18 | 0.0240 | |
| | | |
| Mean | 0.0278 | 0.0073 |
| VAR | 0.0008 | 0.0004 |
| STD | 0.0288 | 0.0211 |
| Overall | | |
| Mean | 0.0178 | |
| VAR | 0.0007 | |
| STD | 0.0270 | |

Table 4.3. Integral $\int_V \frac{\vec{\nabla} \bullet \vec{\beta}}{1.11 \times \frac{V_{\max}}{f_{\max}}} dV$ conducted over both lungs.

# Chapter 5

# Mechanics of Respiration

Although the accuracy and application of the heuristic breathing motion model has been discussed in the original paper[33] and the previous chapter, the biomechanical meaning behind the parameters of the breathing motion model was not yet clearly described. The goal of this chapter is to rebuild the free breathing lung motion model by examining the biomechanical properties of lung tissue. To distinguish the model we are about to develop in this chapter from the heuristic free breathing lung motion model we have discussed in previous chapters, we term the former the biomechanical model and the latter 5D model (tidal volume, air flow and 3 independent components of reference position) or lung motion model. We will see that the biomechanical model agrees with the 5D model under the first order approximation, giving biomechanical interpretation to parameters in the heuristic breathing motion model.

The alveoli, where the exchanges of gas take place, constitute 70% of the parenchyma at the distal level of the bifurcated airway structure. Lung tissue motion is driven by the response of alveoli to the actions of the respiratory muscles, as the volume of the lung increases with inhalation and decreases with exhalation. Among all the respiratory

muscles, the diaphragm, acting like a piston to increase the volume of thoracic cavity, is the primary breathing muscle driving respiration.

Adult alveoli have average diameter of 0.2 mm with a very thin membrane. A very fine mesh of capillaries covers the alveoli, stretching over 70% of the alveoli surface. The capillary network, together with a skeleton of connective tissue fibers that are mainly composed of collagen and elastin, build a wall called the interalveolar septum that is shared by adjacent alveoli. The lung parenchyma is filled with interstitial fluid that acts as the transmitter of pleural pressure[57].

In this chapter, the alveolar structure is modeled simply as a cubic network. The stresses on the lung tissue are analyzed to establish the relationship between the driving forces and the resulting deformation. The biomechanical model will be compared against the published heuristic 5D lung motion model[33,58].Verification of the biomechanical model will be provided by comparing results from patient data with 5D model predictions.

## 5.1 Stress Distribution in the Lung

Alveoli have an irregular polyhedral configuration. A close observation of fluorescently labeled lung parenchyma, conducted by Brewer et al[59] in 2003 as illustrated in Fig. (5.1a), shows a roughly hexagonal arrangement of alveoli. In this chapter, we employ a cubic network to model the alveoli arrangement. The projection of this arrangement is illustrated in Fig. (5.1c); the cubic-shaped alveolus is subjected to distending stresses that inflate the alveolus on its 6 faces, each operating at an angle of $90^{o}$ with respect to the

shared alveolar wall. The distending stresses come from the pressure drop between the inside and outside of the alveolar cell, which ultimately arises from the pressure drop across the alveolar cell and the pleural wall as will be demonstrated below. The direction of distending stress is normal to the surface upon which it acts, and it will be termed here as normal stress.

Under quasi-static conditions and ignoring the velocity variation of connected tissues, a balance of stresses on the alveolar wall is reached. The equation of balanced stresses normal to the alveolar wall is:

$$P_1^{alv} + P_2^{w} + T_2^{normal} = P_2^{alv} + P_1^{w} + T_1^{normal} \tag{5.1}$$

where $P_1^{alv}$ and $P_2^{alv}$ are the alveolar pressures in alveoli 1 and 2 respectively. $P_1^{w}$ and $P_2^{w}$ are the radial stresses arising from the surface tension on the alveolar membrane, with subscripts 1 and 2 indicating the source of the surface tension. $T_1^{normal}$ and $T_2^{normal}$ are the surface tensions arising from the resistance of the alveolar wall against the inflation and deflation of alveoli and are normal to the alveolar walls. The source of the recoil stresses is indicated by the subscript. Although most of the physiology literature assumes these pressures to be equal, this assumption is only valid when the airflow is infinitesimally slow. As the airflow rate changes during respiration, the pressure drop between the atmosphere and inside of alveoli changes nonuniformly. This slight fluctuation in the alveolar pressure distribution is non-trivial, especially when considering hysteresis, which is caused by the imbalance of pressure along the moving path.

A question we try to answer in this chapter is how the stress that distends the alveolus is related to the pleural pressure. Applying Eq. (5.1) to a sac of alveoli *i* as illustrated in Fig. (5.1c), the following equations are defined for a chain of alveoli to the lung boundary,

$$\begin{aligned} P_i^{alv} + P_{i+1}^{w} + T_{i+1}^{normal} &= P_{i+1}^{alv} + P_i^{w} + T_i^{normal} \\ P_{i+1}^{alv} + P_{i+2}^{w} + T_{i+2}^{normal} &= P_{i+2}^{alv} + P_{i+1}^{w} + T_{i+1}^{normal} \\ \cdots \quad &\cdots \\ P_{n-1}^{alv} + P_n^{w} + T_n^{normal} &= P_n^{alv} + P_{n-1}^{w} + T_{n-1}^{normal} \\ P_n^{alv} &= P_{pl} + P_n^{w} + T_n^{normal} \end{aligned}$$

Summing the equations results in

$$P_i^{alv} - P_{pl} = P_i^{w} + T_i^{normal} \tag{5.2}$$

Eq. (5.2) states that if the motion of the alveolar cell is ignored, any alveolus, wherever it is, is exposed to the pleural pressure. $P_i^{alv} - P_{pl}$ provides the stress that expands the volume of the alveolar cell. $P_i^{w}$ and $T_i^{normal}$ together provide the recoil stress from the i$^{th}$ alveolar unit. Many publications have described the measuring of recoil stress[60]. The recoil stress is passive and serves as the response of lung structure to the normal stress that inflates the lung. The recoil stress is virtually equivalent to the normal stress in magnitude and opposite in direction under the condition of quiet respiration.

## 5.2 Biomechanical Model

In this chapter, we define a unit tissue as a piece of lung tissue with unit dimensions. The unit tissue is small enough to be virtually homogeneous inside, while big enough that principles of classical mechanics still apply. Such a unit tissue is considered to contain the structures similar to that of the alveolus. A unit tissue of 1×1×1 mm$^3$ contains

approximately 125 alveoli, smoothing out the modeling or calculating error of each alveolus.

A stress vector $\vec{S}_n$ is defined as the stress on a plane normal to the vector $\vec{n}$ and passing through the point of interest. Although there are infinite number of planes passing through that point, Cauchy showed that by just knowing the stress vectors on three orthogonal planes, the stress vector on any plane passing through that point can be found through coordinate transformations. In general, the stress can be presented by a second-order Cartesian tensor which completely defines the state of stresses at a point $\vec{x}_0$,

$$\vec{\vec{S}} = \begin{bmatrix} s_{11}(V, f, \vec{x}_0) & s_{12}(V, f, \vec{x}_0) & s_{13}(V, f, \vec{x}_0) \\ s_{21}(V, f, \vec{x}_0) & s_{22}(V, f, \vec{x}_0) & s_{23}(V, f, \vec{x}_0) \\ s_{31}(V, f, \vec{x}_0) & s_{32}(V, f, \vec{x}_0) & s_{33}(V, f, \vec{x}_0) \end{bmatrix}, \tag{5.3}$$

where $s_{11}$, $s_{22}$ and $s_{33}$ are the normal stresses that are normal to the orthogonal planes. $s_{12}$ and $s_{13}$, $s_{21}$ and $s_{23}$, $s_{31}$ and $s_{32}$ are 3 pairs of shear stresses that are parallel to the orthogonal planes. We hypothesized that all nine elements in the stress tensor are functions of tidal volume and air flow.

Introducing

$$\pi_{ij} = \frac{s_{ij} + s_{ji}}{2} \tag{5.4}$$

and

$$\tau_{ij} = \frac{s_{ij} - s_{ji}}{2} \tag{5.5}$$

the stress tensor can be decomposed into symmetric and anti-symmetric components,

$$\begin{aligned}\vec{\vec{S}} &= \vec{\vec{S}}_{symm} + \vec{\vec{S}}_{anti-symm} \\ &= \begin{bmatrix} \pi_{11}(V, f, \vec{x}_0) & \pi_{12}(V, f, \vec{x}_0) & \pi_{13}(V, f, \vec{x}_0) \\ \pi_{21}(V, f, \vec{x}_0) & \pi_{22}(V, f, \vec{x}_0) & \pi_{23}(V, f, \vec{x}_0) \\ \pi_{31}(V, f, \vec{x}_0) & \pi_{32}(V, f, \vec{x}_0) & \pi_{33}(V, f, \vec{x}_0) \end{bmatrix} + \begin{bmatrix} 0 & \tau_{12}(V, f, \vec{x}_0) & \tau_{13}(V, f, \vec{x}_0) \\ \tau_{21}(V, f, \vec{x}_0) & 0 & \tau_{23}(V, f, \vec{x}_0) \\ \tau_{31}(V, f, \vec{x}_0) & \tau_{32}(V, f, \vec{x}_0) & 0 \end{bmatrix}\end{aligned} \tag{5.6}$$

where $\vec{\vec{S}}_{symm}$ is a symmetric Cauchy stress tensor working on a body that is in equilibrium and satisfies conservation of angular momentum; $\vec{\vec{S}}_{anti-symm}$ is an anti-symmetric Cauchy stress tensor that gives net moments to the body and causes rigid rotation.

For any symmetric Cauchy stress tensor, we can always find three orthogonal planes, called principal planes, where shear stresses vanish, resulting in the corresponding stress vector that is perpendicular to the plane. The three stresses normal to these principal planes are called principal stresses. If we choose a coordinate system with axes oriented to the principal directions, then the normal stresses will be the principal stresses and the stress tensor is represented by a diagonal matrix.

$$\vec{\vec{S}}_{symm} = \begin{bmatrix} \sigma_1 & 0 & 0 \\ 0 & \sigma_2 & 0 \\ 0 & 0 & \sigma_3 \end{bmatrix} \tag{5.7}$$

where $\sigma_1 \geq \sigma_2 \geq \sigma_3$. Under equilibrium conditions, the principal stress can be written as a combination of the pressure across the alveolar wall and the stress from gravity,

$$\sigma_i = p(V, f) + g_i \tag{5.8}$$

where $g_i$ is the pressure caused by the gravity on principal direction *i*.

On any plan that passes through a point on which the symmetric Cauchy stress tensor $\overleftrightarrow{S}_{symm}$ works, the maximum shear stress $\tau_{\max}$ is given by[61]

$$\begin{aligned} \tau_{\max} &= \frac{1}{2}(\sigma_1 - \sigma_3) \\ &= \frac{1}{2}(g_1 - g_3) \end{aligned} \tag{5.9}$$

The maximum difference between pressures caused by gravity is given by the weight of the alveolus on the cross section area. Comparing to the isotropic pressure drop across the alveolar wall that is caused by the breathing muscles, the anisotropic pressures from gravity is negligible. Ignoring the impact of gravity, the maximum shear stress $\tau_{\max}$ goes to zero. Hence the principal stress can be simply presented by the pressure drop across the alveolar wall. The symmetric Cauchy stress tensor $\overleftrightarrow{S}_{symm}$ can be reduced into

$$\overleftrightarrow{S}_{symm} = \begin{bmatrix} p(V, f) & 0 & 0 \\ 0 & p(V, f) & 0 \\ 0 & 0 & p(V, f) \end{bmatrix} \tag{5.10}$$

On the other hand, the rigid-rotation tensor $\overleftrightarrow{S}_{anti-symm}$, part of the shear stress in $\overleftrightarrow{S}$, comes from the relative motion between adjacent tissues. We find that the relative motion reaches its minimum at beginning of inhalation and end of exhalation when airflow is minimal, and maximum at the middle of inhalation and exhalation when airflow is maximal. Bases on this observation, we assume that all the shear stress components in $\overleftrightarrow{S}_{anti-symm}$ only depend on airflow instead of tidal volume. Hence $\overleftrightarrow{S}_{anti-symm}$ can be reduced to

$$\vec{\vec{S}}_{anti-symm} = \begin{bmatrix} 0 & \tau_{12}(f,\vec{x}_0) & \tau_{13}(f,\vec{x}_0) \\ \tau_{21}(f,\vec{x}_0) & 0 & \tau_{23}(f,\vec{x}_0) \\ \tau_{31}(f,\vec{x}_0) & \tau_{32}(f,\vec{x}_0) & 0 \end{bmatrix} \tag{5.11}$$

The stress tensor $\vec{\vec{S}}$ is therefore simplified to be

$$\vec{\vec{S}} = \begin{bmatrix} p(V,f) & \tau_{12}(f,\vec{x}_0) & \tau_{13}(f,\vec{x}_0) \\ \tau_{21}(f,\vec{x}_0) & p(V,f) & \tau_{23}(f,\vec{x}_0) \\ \tau_{31}(f,\vec{x}_0) & \tau_{32}(f,\vec{x}_0) & p(V,f) \end{bmatrix} \tag{5.12}$$

The stress vector $\vec{S}_n$ that works on a plane normal to unit vector $\vec{n} = (n_1, n_2, n_3)$ is given by

$$\begin{aligned} \vec{S}_n &= \vec{n} \cdot \vec{\vec{S}} \\ &= \vec{\sigma}_n + \vec{\tau}_n \end{aligned} \tag{5.13}$$

where $\vec{\sigma}_n$ is the normal stress that works on the plane, whose magnitude is given by

$$\begin{aligned} \left|\vec{\sigma}_n\right| &= \vec{n} \cdot \vec{\vec{S}} \cdot \vec{n} \\ &= n_1^2 p + n_2^2 p + n_3^2 p + n_1 n_2 \tau_{12} + n_1 n_2 \tau_{21} + n_1 n_3 \tau_{13} + n_1 n_3 \tau_{31} + n_2 n_3 \tau_{23} + n_2 n_3 \tau_{32} \\ &= p(V,f) \end{aligned} \tag{5.14}$$

$\vec{\tau}_n$ is the shear stress that works on the plane. It is perpendicular to the normal stress $\vec{\sigma}_n$ working on the same plane, and its magnitude is given by

$$\begin{aligned} \left|\vec{\tau}_n\right| &= \sqrt{\left|S_n\right|^2 - \left|\sigma_n\right|^2} \\ &= \sqrt{\tau_{12}^2 + \tau_{13}^2 + \tau_{23}^2 - \left(n_3\tau_{12} - n_2\tau_{13} - n_1\tau_{23}\right)^2} \\ &= \tau(f) \end{aligned} \tag{5.15}$$

Suppose the strain of the unit tissue at tidal volume $V$ and airflow rate $f$ is $x$ in the $\vec{n}$ direction. As the tidal volume changes from $V$ to $V+\delta V$ and the airflow rate changes from $f$ to $f+\delta f$, the strain follows from $x$ to $x+\delta x$. The change of the strain is given by

$$\delta x_n = \frac{\vec{\sigma}_n(V+\delta V, f+\delta f, \vec{x}_0) - \vec{\sigma}_n(V, f, \vec{x}_0)}{E(\vec{x}_0)} + \frac{\vec{\tau}_n(f+\delta f, \vec{x}_0) - \vec{\tau}_n(f, \vec{x}_0)}{G(\vec{x}_0)} \qquad (5.16)$$

where $\vec{x}_0$ is the location of the tissue at zero tidal volume and airflow, $\vec{\sigma}_n(V, f, \vec{x}_0)$ is the normal stress vector and $\vec{\tau}_n$ is the shear stress vector. $E(\vec{x}_0)$ is Young's modulus of the tissue and $G(\vec{x}_0)$ is the shear modulus. $\delta$ indicates an infinitesimal variation from the original value.

The Taylor expansion of $\vec{\sigma}_n(V+\delta V, f+\delta f, \vec{x}_0)$ at $V=V_0$ and $f = f_0$ is

$$\begin{aligned}\vec{\sigma}_n(V+\delta V, f+\delta f, \vec{x}_0) = \vec{\sigma}_n(V_0, f_0, \vec{x}_0) \\ + \frac{\partial \vec{\sigma}_n(V, f, \vec{x}_0)}{\partial V}\bigg|_{\substack{V=V_0 \\ f=f_0}} (V+\delta V - V_0) + \frac{\partial \vec{\sigma}_n(V, f, \vec{x}_0)}{\partial f}\bigg|_{\substack{V=V_0 \\ f=f_0}} (f+\delta f - f_0) \\ + \frac{\partial^2 \vec{\sigma}_n(V, f, \vec{x}_0)}{\partial V^2}\bigg|_{\substack{V=V_0 \\ f=f_0}} (V+\delta V - V_0)^2 + \frac{\partial^2 \vec{\sigma}_n(V, f, \vec{x}_0)}{\partial f^2}\bigg|_{\substack{V=V_0 \\ f=f_0}} (f+\delta f - f_0)^2 \\ + \frac{\partial^2 \vec{\sigma}_n(V, f, \vec{x}_0)}{\partial V \partial f}\bigg|_{\substack{V=V_0 \\ f=f_0}} (f+\delta f - f_0)(V+\delta V - V_0) + \ldots\end{aligned} \qquad (5.17)$$

The Taylor expansion of $\vec{\tau}_n(f+\delta f, \vec{x}_0)$ at $f = f_0$ is

$$\vec{\tau}_n(f+\delta f,\vec{x}_0)=\vec{\tau}_n(f_0,\vec{x}_0)+\left.\frac{\partial\vec{\tau}_n(V,f,\vec{x}_0)}{\partial f}\right|_{V=V_0}(f+\delta f-f_0)+\left.\frac{\partial^2\vec{\tau}_n(V,f,\vec{x}_0)}{\partial f^2}\right|_{V=V_0}(f+\delta f-f_0)^2+\ldots \tag{5.18}$$

where $V_0$ and $f_0$ are selected to minimize the approximation error. In this study, we chose $V_0=0$ and $f_0=0$. Stubbs, et al[62] studied the correlation between recoil pressure, lung volume and air flow rate. His results suggested that a linear relationship exists between recoil pressure, lung volume and airflow, especially during quiet respiration. We hypothesize that the first order approximation in Eq. (5.17) and Eq. (5.18) would be adequate to achieve adequate clinical precision. Therefore Eq. (5.16) is reduced to

$$\delta\vec{x}_n=\frac{1}{E(\vec{x}_0)}\left(\delta V\left.\frac{\partial\vec{\sigma}_n(V,f_0,\vec{x}_0)}{\partial V}\right|_{V=V_0}+\delta f\left.\frac{\partial\vec{\sigma}_n(V_0,f,\vec{x}_0)}{\partial f}\right|_{f=f_0}\right)+\frac{1}{G(\vec{x}_0)}\left(\delta f\left.\frac{\partial\vec{\tau}_n(f,\vec{x}_0)}{\partial f}\right|_{f=f_0}\right) \tag{5.19}$$

When tidal volume changes from zero to $V$ and air flow from zero to $f$, the strain is accumulated to

$$\begin{aligned}\Delta\vec{x}_n &=\int\delta\vec{x}_n\\ &=\int_0^V\frac{1}{E(\vec{x}_0)}\left.\frac{\partial\vec{\sigma}_n(V,f_0,\vec{x}_0)}{\partial V}\right|_{V=V_0}dV+\int_0^f\frac{1}{E(\vec{x}_0)}\left.\frac{\partial\vec{\sigma}_n(V_0,f,\vec{x}_0)}{\partial f}\right|_{f=f_0}df\\ &\quad+\int_0^f\frac{1}{G(\vec{x}_0)}\left.\frac{\partial\vec{\tau}_n(f,\vec{x}_0)}{\partial f}\right|_{f=f_0}df\end{aligned} \tag{5.20}$$

where $\Delta\vec{x}_n$ is the strain vector of the unit tissue. The total displacement of the unit tissue is accumulated by all pieces of tissue moving behind it. Therefore, the displacement vector $\Delta\vec{X}_n$ due to air filling is

$$\begin{aligned}\Delta\vec{X}_n &= \int_0^{\vec{x}_0} d\vec{x}\int_0^V \frac{1}{E(\vec{x})}\frac{\partial\vec{\sigma}_n(V, f_0, \vec{x})}{\partial V}\bigg|_{V=V_0} dV + \int_0^{\vec{x}_0} d\vec{x}\int_0^f \frac{1}{E(\vec{x})}\frac{\partial\vec{\sigma}_n(V_0, f, \vec{x})}{\partial f}\bigg|_{f=f_0} df \\ &\quad \int_0^{\vec{x}_0} d\vec{x}\int_0^f \frac{1}{G(\vec{x})}\frac{\partial\vec{\tau}_n(f, \vec{x})}{\partial f}\bigg|_{f=f_0} df\end{aligned} \tag{5.21}$$

where 0 denotes the location in the lung where the tissue doesn't move during respiration. Three additional variables are introduced

$$\vec{\alpha}(\vec{x}_0) = \int_0^{\vec{x}_0} \frac{1}{E(\vec{x})}\frac{\partial\vec{\sigma}_n(V, f_0, \vec{x})}{\partial V}\bigg|_{V=V_0} d\vec{x} \tag{5.22}$$

$$\vec{\beta}_1(\vec{x}_0) = \int_0^{\vec{x}_0} \frac{1}{E(\vec{x})}\frac{\partial\vec{\sigma}_n(V_0, f, \vec{x})}{\partial f}\bigg|_{f=f_0} d\vec{x} \tag{5.23}$$

$$\vec{\beta}_2(\vec{x}_0) = \int_0^{\vec{x}_0} \frac{1}{G(\vec{x})}\frac{\partial\vec{\tau}_n(f, \vec{x})}{\partial f}\bigg|_{f=f_0} d\vec{x} \tag{5.24}$$

Since $\vec{\alpha}$, $\vec{\beta}_1$ and $\vec{\beta}_2$ are functions only of the reference position $\vec{x}_0$, the total displacement vector $\Delta\vec{X}_n$ is reduced to

$$\begin{aligned}\Delta\vec{X}_n &= \int_0^V \vec{\alpha}(\vec{x}_0)dV + \int_0^f \vec{\beta}_1(\vec{x}_0)df + \int_0^f \vec{\beta}_2(\vec{x}_0)df \\ &= \vec{\alpha}(\vec{x}_0)V + \vec{\beta}(\vec{x}_0)\, f\end{aligned} \tag{5.25}$$

where $\vec{x}_0$ is the position of the tissue at zero tidal volume and zero airflow, and $\vec{\alpha}(\vec{x}_0)$ and $\vec{\beta}(\vec{x}_0)$ are used to be consistent with the equation originally proposed by Low, et al.[33]

Physiologically, $\vec{\alpha}(\vec{x}_0)$ characterizes the displacement of lung tissues due to air filling, and $\vec{\beta}(\vec{x}_0)$ characterizes the hysteresis motion that was described by Seppenwoolde, et al[21]. While $\vec{\alpha}$ is determined by the overall integral of the tidal volume derivative of the normal stress, $\vec{\beta}$ is decomposed into two independent components, $\vec{\beta}_1$ and $\vec{\beta}_2$. The first one is perpendicular to $\vec{\alpha}$ and the second one is parallel to $\vec{\alpha}$.

## 5.3 Angle Analysis

An evaluation of the terms $\vec{\alpha}$, $\vec{\beta}$ ($\vec{\beta}_1$ and $\vec{\beta}_2$) from Eq. (5.22), Eq. (5.23), and Eq. (5.24) is illustrated in Fig.(5.2). $\vec{\alpha}$ is the integral of the tidal volume derivative of normal stress over the lung space at constant airflow rate, and similarly, $\vec{\beta}$, the combination of $\vec{\beta}_1$ and $\vec{\beta}_2$, is the integral of the airflow derivative of stress over the lung space at constant tidal volume. The $\vec{\alpha}$ motion component is contributed entirely by the change of tidal volume, or equivalently, the change of lung volume. The $\vec{\beta}$ component, which comes from changes of airflow rate during breathing, characterizes the hysteresis component of the motion and contributes nothing to the volume change. The $\vec{\beta}_1$ component, which is parallel to $\vec{\alpha}$, aligns with the displacement vector which is driven by the normal pressure gradient purely from volume change. Therefore it contributes to a displacement that

further inflates or deflates the lung and subsequently changes the volume of any individual piece of tissue on which it works. However, the changes of volume add up to zero over the whole lung space because according to the definition, $\vec{\beta}_1$ is the airflow rate derivative of normal stress at a fixed tidal volume. The $\vec{\beta}_2$ component, which is perpendicular to $\vec{\alpha}$, serves as a rigid-body rotation of the $\vec{\alpha}$ component and won't change the volume of the tissue it works on. The verification that the summation of $\vec{\beta}$ over the lung space equals zero was described in chapter 4.

In the region where the normal stress decreases as airflow increases, the direction of $\vec{\beta}_1$ is anti-parallel to that of $\vec{\alpha}$. In the region where normal stress increases as airflow increases, the direction of $\vec{\beta}_1$ is parallel to that of $\vec{\alpha}$. $\vec{\beta}$ lies at a specific angle θ with respect to $\vec{\alpha}$ and this angle will be predicted and measured as described in section 5.4.3.

## 5.4. Model Validation

49 patients were enrolled in an IRB-approved protocol and scanned using a 16-slice CT scanner operating in ciné mode and acquiring scans with a spatial resolution of 0.98 x 0.98 x 1.5 $mm^3$.25 scans were acquired contiguously at each 24 mm wide couch position (CP). Two external respiratory measurements were simultaneously acquired; the tidal volume measured using a spirometer (VMM-400, Interface Associates), and a bellows pressure signal measured using a pneumatic belt system that was wrapped around the abdomen. The bellows pressure measurement was correlated with the spirometry measurement to provide the tidal volume and airflow at each scan. [47,48]

### 5.4.1 Results from the Empirical Lung Motion Model

The tissue positions were mapped for each scan using a normalized cross-correlation method. The scan with tidal volume closest to zero was employed as the reference scan. The rest of scans were sorted on tidal volume and categorized into inhalation and exhalation. The position matching was performed in the inhalation and exhalation categories respectively in the order of tidal volume, with zero motion as the initial estimate for the first registration in one category and the result from previous matching as the initial estimate for the remaining registrations in that category.

The registration results, together with the corresponding tidal volumes and airflows were fit to Eq. (1.1) employing the Nelder-Mead Optimization Algorithm by minimizing the root-mean least-squares average distance between the fitting and measurements.

$$\min_{\vec{X}_0,\vec{\alpha},\vec{\beta}\in\Re^3} \sum_i \left\| \vec{X}_i - \vec{X}_0 - \vec{\alpha} v_i - \vec{\beta} f_i \right\| \tag{5.26}$$

where $\vec{X}_i$ was the $i^{th}$ location of the measurements, and $v_i$ and $f_i$ were the tidal volume and airflow, respectively, for scan $i$. In this study, 25 scans were obtained for each couch position, so $\vec{X}_0$, $\vec{\alpha}$ and $\vec{\beta}$ in Eq. (5.26) were overdetermined to suppress the impact of image motion artifacts and registration errors.

For each dataset, we defined $\left|\vec{\alpha}\right|_{90}$ and $\left|\vec{\beta}\right|_{90}$ as the 90$^{th}$ percentile of the $\vec{\alpha}$ and $\vec{\beta}$ magnitudes, respectively. We choose the 90$^{th}$ percentile as the indicator to represent the

maximum $\vec{\alpha}$ and $\vec{\beta}$ magnitudes because it was stable against registration and fitting errors.

### 5.4.2 Results from the Biomechanical Model

$\vec{\alpha}$ and $\vec{\beta}$ result from the stresses in the lung parenchyma. Theoretically, they can be predicted through Eq. (5.22), Eq. (5.23) and Eq. (5.24) if the Young's modulus, shear modulus, tidal volume and airflow rate derivative of stress, and the distance from the investigated tissue to a fixed reference point are known. Although in-vivo acquisition of patient-specific parameters required in Eq. (5.22), Eq. (5.23), and Eq. (5.24) are infeasible, values in the literature were used here for estimations. The Young's modulus $E$ was taken to be 27.7 cm $H_2O$ from Lai-Fook, et al[63] by averaging results from 15 subjects with two independent measuring methods. The average tidal volume derivative of normal stress $\frac{\partial \sigma_n}{\partial V}$ was 3.80 cm $H_2O$/L from a study conducted by Rodarte et al.[60] The average airflow rate derivative of normal stress $\frac{\partial \sigma_n}{\partial f}$ was estimated to be 0.40 cm $H_2O$ s/L from the study conducted by Stubbs et al[62]. Since no published literature data on the shear stress inside of the lung is available, only $\vec{\beta}_1$ could be estimated from published data. The reference point that is supposed not to move during respiration was set at the apex of the lung. The lung height $L_{90}$ was defined as the 90$^{th}$ percentile of distances of all points inside the lung to the reference point. Using these values, $|\vec{\alpha}|_{90}$ was predicted using Eq. (5.22), which is

$$\begin{aligned} \left|\vec{\alpha}\right|_{90} &= \frac{L_{90}}{E}\frac{\partial \sigma_n}{\partial V} \\ &= \frac{3.80}{27.7}L_{90} \end{aligned} \tag{5.27}$$

$\left|\vec{\beta}_1\right|_{90}$ was be predicted using Eq. (5.23),

$$\begin{aligned} \left|\vec{\beta}_1\right|_{90} &= \frac{L_{90}}{E}\frac{\partial \sigma_n}{\partial f} \\ &= \frac{0.40}{27.7}L_{90} \end{aligned} \tag{5.28}$$

### 5.4.3 Comparison of $\vec{\alpha}$ and $\vec{\beta}$ between the Empirical Lung Motion Model and the Biomechanical Model

A comparison of the 90th percentile of the $\vec{\alpha}$ magnitudes from both the 5D model and the biomechanical model was used to evaluate how well both models agree with each other. $\vec{\beta}$ is a vector composed of two orthogonal vectors, $\vec{\beta}_1$ and $\vec{\beta}_2$, and the angle between $\left|\vec{\beta}_1\right|$ and $\left|\vec{\beta}\right|$ is given by

$$\cos(\vartheta_1) = \frac{\left|\vec{\beta}_1\right|}{\left|\vec{\beta}\right|} \tag{5.29}$$

Although $\vec{\beta}$ could be determined clinically by fitting the patient data to our empirical lung motion model, it could not be fully recovered from the biomechanical model because the determination of one component of $\vec{\beta}$, $\vec{\beta}_2$, required information on the shear stress between adjacent tissues, for which we did not have any qualitative study to refer to. Therefore, the only possible way to calculate the angle

$\vartheta_1$ was performed by taking $\left|\vec{\beta}_1\right|_{90}$ from the biomechanical model and $\left|\vec{\beta}\right|_{90}$ from the 5D model by fitting patient data. $\left|\vec{\beta}_1\right|$ was calculated by using published data using Eq. (5.24). Presuming the measurements of the biomechanical properties of lungs obey a Gaussian distribution in the literature mentioned above, the estimation of $\left|\vec{\beta}_1\right|$, which depended on those biomechanical properties should also obey a Gaussian distribution. Therefore, the average $\left|\vec{\beta}_1\right|$ was also the $\left|\vec{\beta}_1\right|$ with maximum likelihood, and $\vartheta_1$ in Eq. (5.29) was taken as the maximum-likelihood angle between $\vec{\beta}_1$ and $\vec{\beta}$, or equivalently, the maximum-likelihood angle between $\vec{\alpha}$ and $\vec{\beta}$.

An alternative way to calculate the angle between $\vec{\alpha}$ and $\vec{\beta}$ was using only the results from 5D model. A new variable $\vartheta$ was introduced to distinguish the angle calculated in this way from the way discussed in the previous paragraph. $\vartheta$ was obtained through the following equation,

$$\cos(\vartheta) = \frac{\vec{\alpha} \cdot \vec{\beta}}{\left|\vec{\alpha}\right|\left|\vec{\beta}\right|} \tag{5.30}$$

where both $\vec{\alpha}$ and $\vec{\beta}$ were obtained from the 5D model by fitting the patient data.

Unlike $\vartheta_1$, $\vartheta$ was obtained from $\vec{\alpha}$ and $\vec{\beta}$ over the whole lung. Due to the variation of lung properties and errors in registration and fitting of 5D model, $\vartheta$ was obtained as a spectrum of angles, instead of a single value. A new parameter $\vartheta_2$ was defined as the angle with the maximum likelihood over the spectrum and is compared to $\vartheta_1$.

As demonstrated by the biomechanical model conducted above, $\vec{\beta}_1$ is parallel to $\vec{\alpha}$. Therefore, $\vartheta_1$ is expected to equal $\vartheta_2$. The comparison of $\vartheta_1$ and $\vartheta_2$ provided another indicator of how well the biomechanical model agreed with the 5D model.

### 5.4.4. Zenith Angle Distribution

The distribution of $\vartheta$ is biased on the Zenith angle distribution which is illustrated in Fig. (5.3). Defining the Zenith direction as parallel to $\vec{\alpha}$, a random distribution of $\vec{\beta}$ would be proportional to sin($\theta$) (Fig.(5.3)). The angular distribution from the 5D model was divided by this baseline to unbias the results.

## 5.5. Results

The craniocaudal dimensions of the lungs in 49 patients were measured using the CT images. The average 90$^{th}$ percentile of the distances between all tissues in both the left and right lungs to the corresponding reference points which were defined at the apex of each lung were 192 mm and 191 mm respectively, as illustrated in Tab. (5.1).

The estimated value of $|\vec{\alpha}|_{90}$ in the left lung from Eq. (5.27) was 26.3 mm/L, compared to the average $|\vec{\alpha}|_{90}$ of 25.2 mm/L from the 5D model. The discrepancy between the biomechanical model prediction and the result by fitting real patient data in the 5D model was 1.1 mm/L, or 4.4% of the fitting result.

The estimated value of $|\vec{\alpha}|_{90}$ in the right lung from Eq. (5.27) was 26.2 mm/L, compared to the average $|\vec{\alpha}|_{90}$ of 28.9 mm/L from the 5D model. The discrepancy between the biomechanical model prediction and the result by fitting real patient data in the 5D model was 2.7 mm/L, or 9.3% of the fitting result.

The estimate of $|\vec{\beta}_1|_{90}$ from Eq. (5.28) was 2.8 mm·s/L in the left lung. The average $|\vec{\beta}|_{90}$ measured from the 5D model was 4.2 mm·s/L in the left lung as listed in Tab. (5.1). The angle $\vartheta_1$ between $\vec{\beta}_1$ and $\vec{\beta}$ was 48.2º. Since $\vec{\beta}_1$ was normal to $\vec{\alpha}$, $\vartheta$ was 41.8º or 138.2º if $\vec{\beta}_2$ was parallel or anti-paralleled to $\vec{\alpha}$, and corresponded to the angles where tissues are pushed and held back by surrounding tissues, respectively.

The estimate of $|\vec{\beta}_1|_{90}$ from Eq. (5.28) was 2.8 mm·s/L in the right lung. The average $|\vec{\beta}|_{90}$ measured from the 5D model was 4.2 mm·s/L in the right lung as listed in Tab. (5.1).. The angle $\vartheta_1$ between $\vec{\beta}_1$ and $\vec{\beta}$ was 48.2º. Therefore, $\vartheta$ was 41.8º or 138.2º if $\vec{\beta}_2$ was or anti-paralleled to $\vec{\alpha}$, respectively.

The spectrum of angles $\vartheta$ between $\vec{\alpha}$ and $\vec{\beta}$ was also measured for the 49 patients. There were 3 typical patterns, illustrated in Fig. (5.4) and Fig.(5.5) for left and right lungs, respectively. All of the distributions included at least one obvious peak, indicating the most probable $\vartheta$. The peak angles were very close to the predictions using the biomechanical model developed in this chapter.

The histogram of angles ($\vartheta_2$) with maximum likelihood in all the datasets is illustrated in Fig. (5.6). Fig. (5.6a). These show that the 5D model localized peaks at 42.1º and 149.5º

in the left lungs, while the two predicted angles ( $\vartheta_1$ ) from the biomechanical model were 41.8º and 138.2º. Fig. (5.6b) showed that the 5D model localized peaks at 37.7º and 133.0º in the right lungs with the same predicted angles as the left lungs from the biomechanical model.

## 5.6 Conclusion and Discussion

This study establishes a relationship that links the empirical 5D breathing motion model parameters published by Low, et al[33] to biomechanical properties of the lung, such as stress and Young's modules. Analysis of the published biomechanical properties of lung tissues provided predictions of the 5D model parameters. They were found to be in good agreement with the directly measured parameters.

The spectrum of $\vartheta$ provides more insight into the stress distribution inside the lung parenchyma. The hysteresis lag in the anterior left lung might be explained by the presence of heart as a geometrical retardant to tissue motion. As the anterior portion of the left lung moved towards the heart, the resistance from the hearts was enhanced by squeezing the lung tissue against the heart. The increased resistance in the anterior portion of the left lung caused the pressure across the alveolar membrane decreased in the same region. Although the pressure inside the alveolus remained, the pressure drop (the normal stress) decreased by the escalation of wall resistance when airflow rose. The physiological sequence of decreased intrapulmonary pressure was that the air was redistributed to region with higher intrapulmonary region like the posterior region.

Therefore, in the anterior portion of the left lung, $\vec{\beta}_1$ is most likely to be anti-parallel to the motion of the lung tissue and $\vartheta_2$ was observed to be larger than 90º. As indicated in Fig. (5.4), the motion of the anterior portion of the left lung was most likely to lag due to the hysteresis component. Similar phenomena were observed in the inferior and posterior portion of the right lung, but for a different reason. Since the heart impacts breathing motion primarily inferior to the left lung, the right lung has less geometrical confinement than the left lung does. Instead, gravity plays a relatively important role in distributing the air in the right lung. Since the inferior and posterior region of the right lung bear more stress from gravity, it has a smaller resting volume at the beginning of inhalation compared to that of the anterior region of the right lung. The elasticity of the lung , which is a monotonically decreasing function of lung volume[64], is in favor of smaller alveoli than larger ones. Therefore, the inferior and posterior region of the right lung is easier to inflate than the superior and anterior region and consequently receives more ventilation. However, the relatively smaller air space and more ventilation in the inferior and posterior region would escalate the pressure inside of alveolus higher than in the superior and anterior region as airflow increases. The higher alveolar pressure would redistribute the air from the inferior and posterior region to the superior and anterior region. Hence the pressure drop that drives the alveolus to inflate in the inferior and posterior region would decrease. Therefore, the motion of the region with better ventilation was subject to a hysteresis lag and $\vartheta_2$ was observed to be larger than 90º, as illustrated in Fig. (5.5) where a hysteresis lag was present in the inferior and posterior region of the right lung. On the other hand, the region with less ventilation would be boosted by the extra air flow and move more than it would have at constant airflow.

In the left lung, the hysteresis lag was present because the amount of air flowing in decreased due to resistance increase during airflow increase. In the right lung, the hysteresis lag was present because the alveolar pressure decreased during airflow increase due to the relatively easy and fast redistribution of air through airways. Both the increase in resistance and the decrease of alveolar pressure lead to a decline in the stress that drives the lung to inflate and deflate.

In this chapter, a biomechanical model was developed by modeling the lung as an elastic material subjected to driven forces from diaphragm and other breathing muscles. The first order approximation of this biomechanical model led to a lung motion model proposed by Low, et al[33]. Two parameters in the biomechanical model, $\vec{\alpha}$ and $\vec{\beta}$ were calculated using published data while the same parameters in Low's 5D lung motion model were fit using clinical datasets. Both models reached close agreement both on the magnitude of the parameters and on the angle of hysteresis with respect to the motion of the concerned tissue.

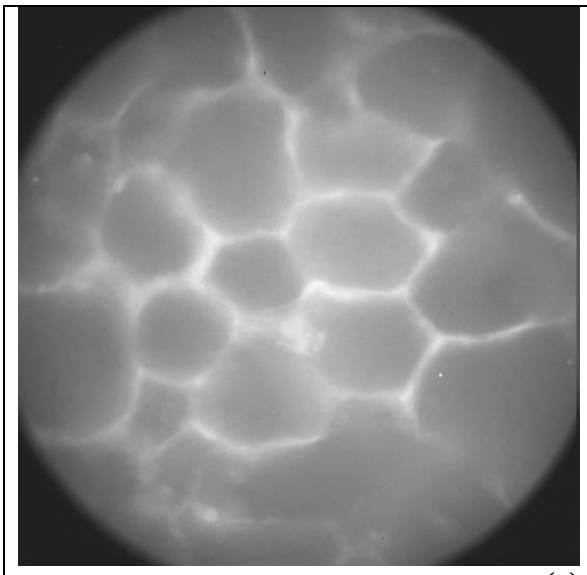

(a)

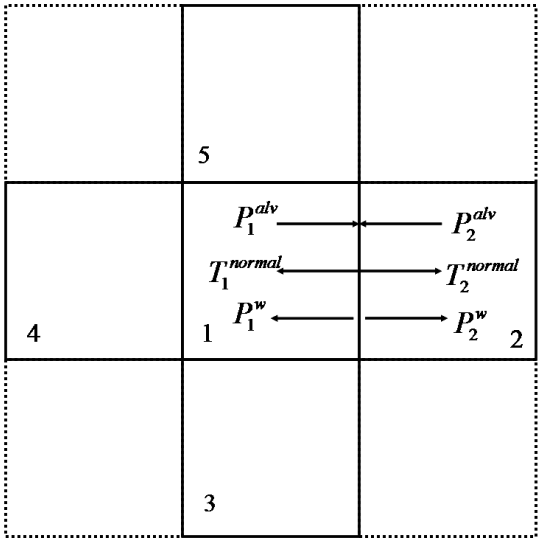


(b)

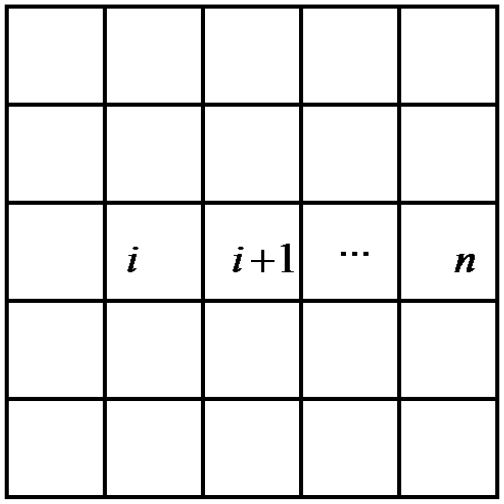


(c)

Fig .5.1: (a) Fluorescently labeled lung tissue, Brewer, K. K. et al. J Appl Physiol 95: 1926-1936 2003 (b) Stresses normal to the wall shared by two adjacent alveoli . $P^{alv}$ is the alveolar pressure and $P^{w}$ comes from the surface tension of the liquid membrane that defines the boundary of alveolus. $T^{normal}$ is the recoil stress from the resistance of the alveolar wall against the deflation or inflation of the alveolus inside. (c) Arrangement of alveoli on a 2D plane.

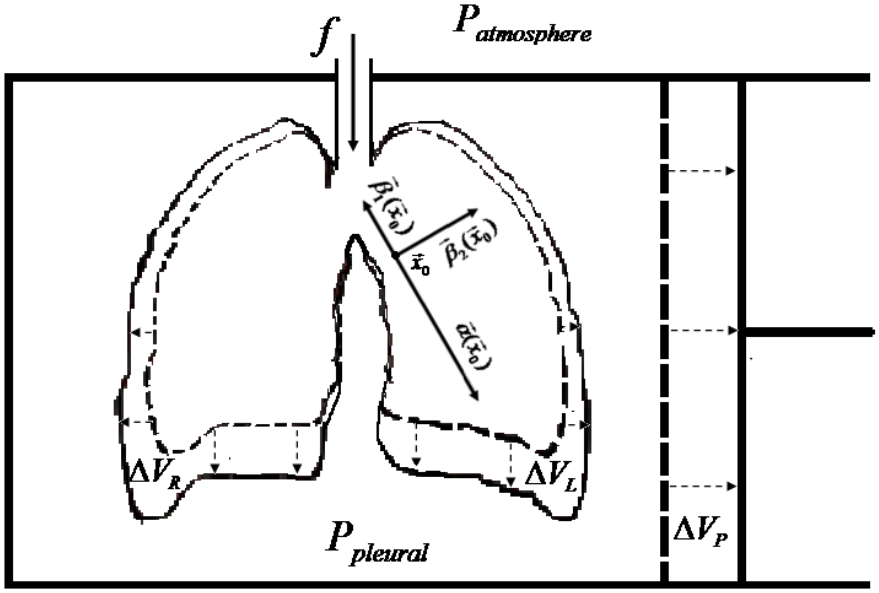


$$\Delta V_R + \Delta V_L = \Delta V_P \Rightarrow f \rightarrow$$
$$\Delta V_R + \Delta V_L < \Delta V_P \Rightarrow f \uparrow$$
$$\Delta V_R + \Delta V_L > \Delta V_P \Rightarrow f \leftarrow$$

Fig .5.2: Chest wall and respiration muscles are simulated with an airtight container and a piston. Airflow rate changes as the free space between the container and the lung. The displacement of tissue at $\vec{x}_0$ is $\vec{\alpha}(\vec{x}_0)V + \vec{\beta}_1(\vec{x}_0)f + \vec{\beta}_2(\vec{x}_0)f$ , as described in Eq (5.25).

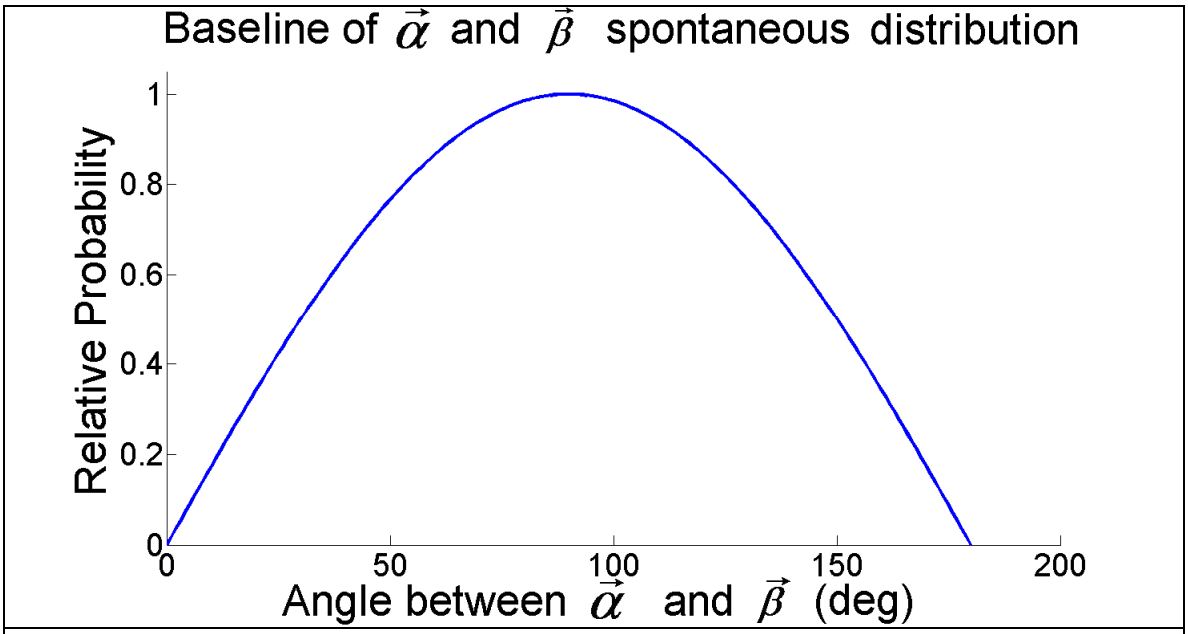


Fig. 5.3 Baseline of $\vec{\alpha}$ and $\vec{\beta}$ spontaneous distribution

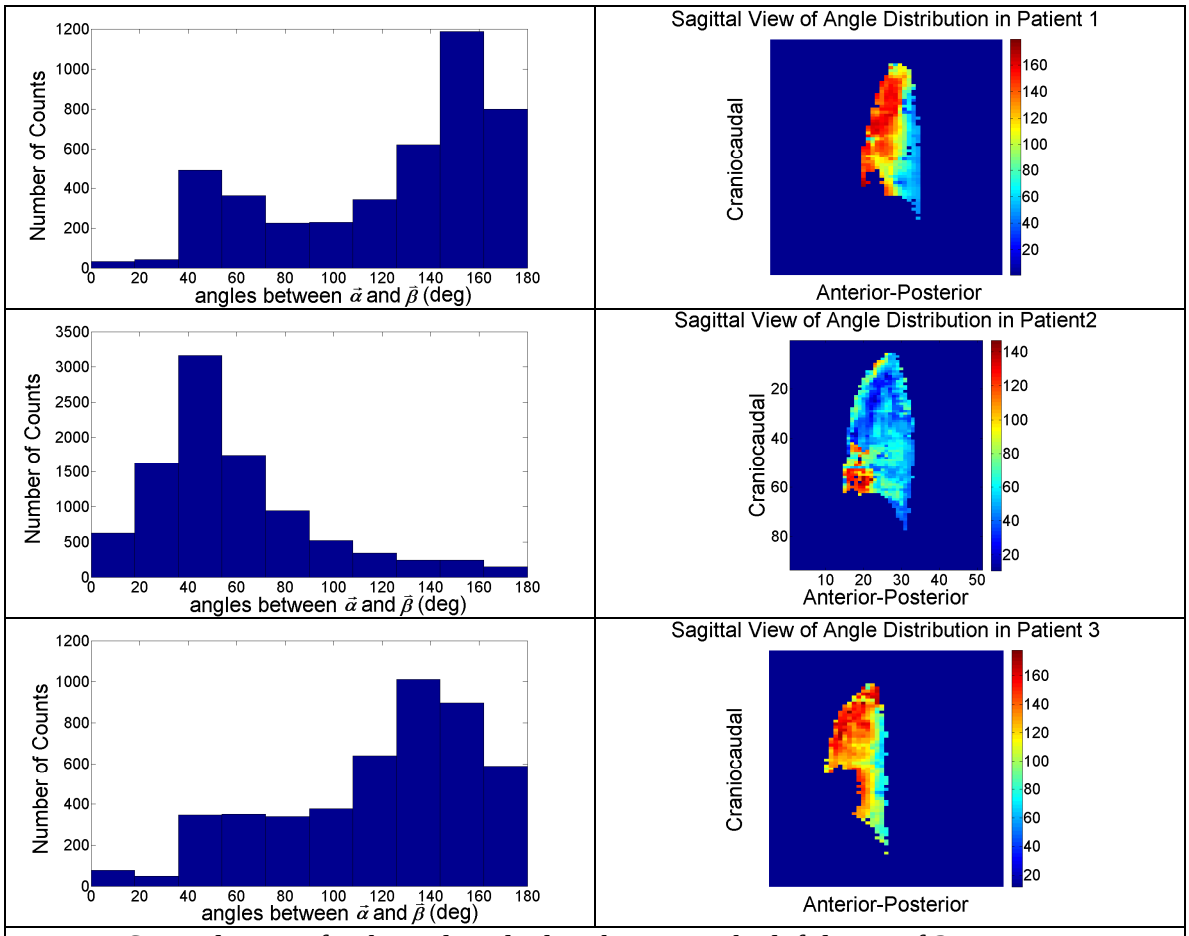


Fig .5.4:Sagittal view of unbiased angle distribution in the left lungs of 3 patients.

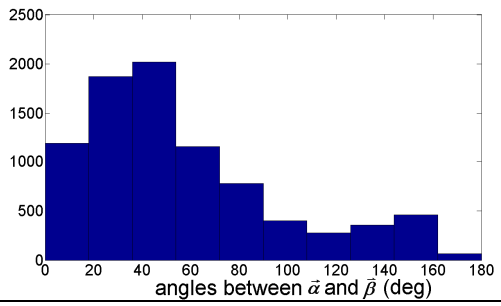


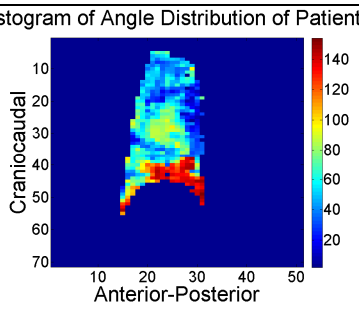


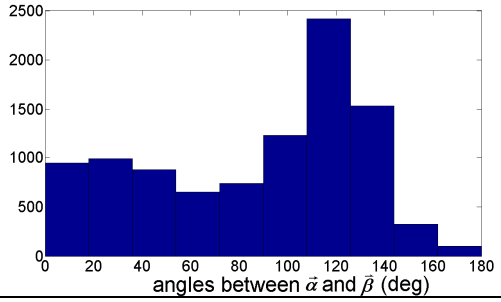


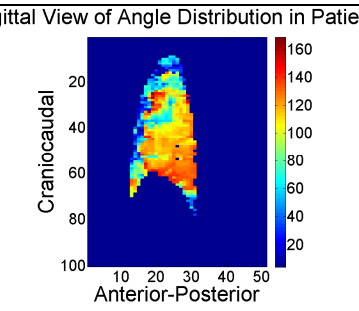


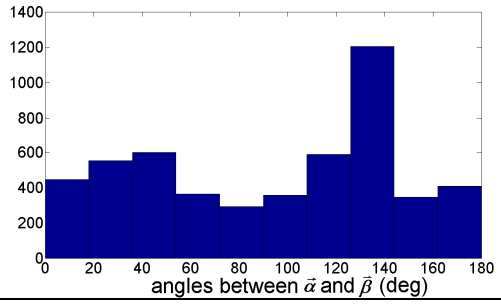


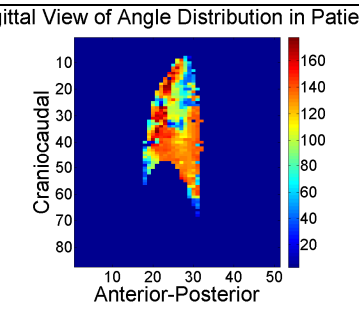


Fig .5.5:Sagittal view of unbiased angle distribution in the right lungs of 3 patients.

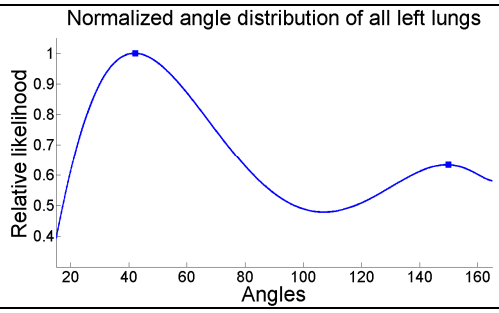


Fig .5.6 (a): Two peaks at 42.1º and 149.5º. The predictions from the biomechanical model are 41.8º and 138.2º.

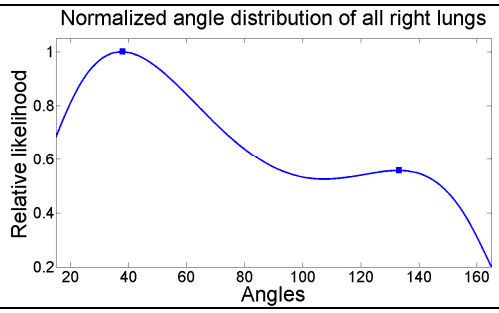


Fig. 5.5.6 (b): Two peaks at 37.7º and 133.0º. the predictions from the biomechanical model are 41.8º and 138.2º.

| Patient # | Left Lung | | | Right Lung | | |
|---|---|---|---|---|---|---|
| | $L_{90}$ (mm) | $\lvert\vec{\alpha}\rvert_{90}$ (mm/L) | $\lvert\vec{\beta}\rvert_{90}$ (mm·s/L) | $L_{90}$ (mm) | $\lvert\vec{\alpha}\rvert_{90}$ (mm/L) | $\lvert\vec{\beta}\rvert_{90}$ (mm·s/L) |
| 1 | 165.2 | 7.1 | 2.2 | 208.0 | 26.1 | 3.8 |
| 2 | 175.0 | 23.8 | 2.8 | 176.2 | 24.7 | 2.7 |
| 3 | 176.3 | 25.7 | 2.9 | 178.2 | 24.1 | 2.5 |
| 4 | 202.8 | 30.9 | 2.9 | 212.6 | 30.7 | 3.8 |
| 5 | 195.5 | 38.7 | 5.8 | 186.1 | 44.5 | 5.7 |
| 6 | 201.1 | 20.1 | 3.8 | 197.3 | 18.4 | 5.0 |
| 7 | 183.6 | 33.1 | 5.1 | 172.7 | 37.3 | 5.1 |
| 8 | 185.4 | 23.2 | 3.2 | 178.3 | 29.5 | 3.2 |
| 9 | 155.1 | 19.4 | 2.5 | 163.1 | 18.9 | 2.0 |
| 10 | 160.6 | 32.3 | 6.8 | 160.7 | 28.1 | 7.5 |
| 11 | 174.2 | 22.1 | 2.6 | 162.4 | 35.8 | 2.8 |
| 12 | 214.1 | 22.5 | 2.7 | 216.9 | 26.8 | 3.3 |
| 13 | 192.4 | 34.2 | 3.6 | 163.1 | 31.7 | 2.8 |
| 14 | 203.1 | 21.0 | 2.2 | 195.3 | 29.9 | 2.4 |
| 15 | 206.1 | 26.1 | 5.5 | 200.8 | 34.1 | 2.6 |
| 16 | 207.5 | 26.4 | 3.4 | 197.5 | 21.8 | 2.8 |
| 17 | 207.0 | 20.5 | 3.1 | 203.9 | 26.2 | 2.6 |
| 18 | 198.5 | 17.5 | 3.2 | 209.9 | 26.9 | 3.2 |
| 19 | 208.7 | 24.3 | 4.9 | 201.3 | 21.6 | 4.2 |
| 20 | 190.4 | 41.6 | 5.3 | 178.6 | 29.6 | 5.3 |
| 21 | 159.0 | 16.9 | 5.4 | 171.8 | 36.6 | 5.0 |
| 22 | 253.2 | 31.6 | 4.8 | 265.9 | 35.2 | 4.6 |
| 23 | 179.1 | 23.0 | 4.4 | 180.7 | 36.6 | 9.1 |
| 24 | 177.2 | 26.0 | 5.1 | 170.7 | 40.9 | 5.8 |
| 25 | 183.1 | 25.6 | 3.9 | 196.6 | 30.0 | 4.3 |
| 26 | 166.3 | 39.3 | 6.1 | 174.7 | 55.0 | 8.4 |
| 27 | 218.8 | 25.1 | 2.7 | 228.6 | 17.0 | 1.9 |
| 28 | 230.9 | 40.5 | 3.2 | 212.7 | 12.5 | 1.8 |
| 29 | 178.0 | 11.3 | 12.1 | 159.4 | 15.1 | 12.1 |
| 30 | 171.3 | 32.4 | 3.6 | 166.0 | 43.9 | 3.5 |
| 31 | 204.0 | 29.3 | 4.9 | 183.9 | 43.0 | 6.0 |
| 32 | 173.5 | 34.3 | 3.7 | 161.6 | 36.0 | 5.0 |
| 33 | 197.5 | 17.3 | 3.6 | 175.0 | 17.9 | 2.8 |
| 34 | 179.5 | 45.6 | 13.4 | 182.6 | 39.5 | 5.9 |
| 35 | 206.7 | 14.9 | 2.7 | 174.1 | 14.9 | 3.7 |
| 36 | 199.5 | 16.7 | 1.6 | 191.9 | 30.9 | 3.9 |
| 37 | 180.5 | 25.5 | 3.8 | 185.1 | 36.6 | 3.7 |
| 38 | 222.3 | 23.7 | 2.3 | 209.8 | 28.3 | 2.8 |
| 39 | 150.1 | 12.8 | 3.7 | 189.7 | 43.1 | 4.6 |
| 40 | 242.7 | 12.6 | 2.8 | 245.1 | 20.6 | 3.0 |
| 41 | 209.7 | 27.0 | 7.8 | 200.6 | 26.5 | 5.1 |
| 42 | 192.2 | 17.3 | 4.4 | 193.1 | 22.2 | 4.4 |
| 43 | 183.0 | 21.8 | 3.0 | 161.2 | 30.5 | 3.5 |
| 44 | 172.1 | 9.1 | 6.3 | 171.0 | 11.0 | 6.7 |
| 45 | 218.6 | 21.2 | 2.6 | 220.2 | 29.0 | 2.5 |

| | | | | | | |
|---|---|---|---|---|---|---|
| 46 | 156.4 | 43.4 | 5.6 | 189.7 | 44.3 | 5.1 |
| 47 | 166.8 | 28.1 | 2.3 | 170.1 | 19.6 | 1.6 |
| 48 | 231.6 | 15.8 | 2.6 | 237.8 | 11.8 | 2.7 |
| 49 | 202.9 | 38.1 | 4.9 | 208.3 | 19.7 | 3.8 |
| Mean | 192.0 | 25.2 | 4.2 | 190.6 | 28.9 | 4.2 |

Table 5.1. 90 percentile of $|\vec{\alpha}|$ and $|\vec{\beta}|$ in both left and right lungs.

# Chapter6

# Characterization of Free Breathing

## 6.1. Introduction

Little is know about the motion pattern of lung tissues during quiet respiration. Textbooks state that the diaphragm is the primary breathing muscle and that the intercostal muscles are secondary in that they help to expand the rib cage. Therefore, the movement of lung tissue is mainly in the cranialcaudal direction with some transverse motion. When observing patients signing up for our protocol, we found that motion pattern variations exist, either in the direction of the dominant motion or its magnitude. In this chapter, $\vec{\alpha}$ and $\vec{\beta}$ distributions were examined, both qualitatively and quantitatively, for each patient to determine general patterns and inter-patient pattern variations.

## 6.2. Methods and Materials

### 6.2.1. Data Acquisition

49 patients were enrolled under an IRB-approved protocol and scanned using a 16-slice CT scanner (Philips 16-slice Brilliance CT) operating in ciné mode using 1.5-mm-thick slices. Of these patients, 28 were lung cancer patients and 21 were non-lung cancer patients. Data were acquired during patients' treatments. Tidal volumes were measured

and calibrated with a spirometer and pneumatic abdominal belt. Air flows were calculated as the time derivative of tidal volumes. More details can be found in Chapter 2.

### 6.2.2. Image Registration

In order to determine the motion model at each point, position measurements of each point of tissue in each CT scan dataset were required. In this study, a fast normalized cross-correlation (NCC) method that was described in Chapter 3 was employed. In order to determine the motion of a specific point of tissue, a small region with $11\times11\times10$ pixels that surrounded the point was identified and the NCC algorithm was used to locate that same region in the other 24 scans. One advantage of using the NCC model was that the determination of the maximum NCC was not sensitive to the variation of CT Hounsfield Units found between inhalation and exhalation CT scans.

The CT scan with the tidal volume closest to 0 ml (exhalation) was selected as the reference scan for purposes of motion mapping. The CT scan length of 2.4 cm limited each multi-slice CT dataset to a small portion of the lung, typically 1/8 or 1/9. The magnitude of the motion at the inferior lung was often greater than 3.0 cm. Some tissue regions, especially those closest to the diaphragm, moved out of the longitudinal coverage of the dataset because the zero tidal volume scan was selected as the reference. This would give rise to two issues that could have compromised the results. Firstly, the region being tracked would move out of the searching region but the NCC registration method would select a region within the couch position with largest correlation

coefficient and produce spurious results. Secondly, if the region of interest moved out of the current couch position and was not tracked, some of the 25 scans would be unused.

In this study, the registration was performed in two directions, depending on the breathing phase relative to the reference phase. During exhalation, the tissue generally moved superiorly. Therefore, the multi-slice CT dataset was first categorized into two groups, inhalation and exhalation respectively. Each group was sorted according to the tidal volumes from low to high. The reference scan was divided into a 3D mesh of abutting templates consisting of $11\times11\times10$ voxels, corresponding to $10.7\times10.7\times15\ mm^3$. The search region, co-centered with the template, had $21\times21\times20$ voxels, corresponding to $20.5\times20.5\times30\ mm^3$. The registration began with the scan that had the tidal volume closest to the reference scan tidal volume. Because 25 scans were acquired during respiration, there were enough tidal volume samples to limit the tidal volume change between two successive scans to less than 100 ml. The magnitude of motion corresponding to a tidal volume change of 100 ml was usually less than 8 mm. The search range used in this study had sufficient margins to allow for this much motion. When a matching tissue was identified, the displacements were recorded and accumulated to generate the new center of search region for the next scan. When the search region was expected to cross the boundary of the current couch position, the portion that moved out was replaced by the corresponding part of the scan in the next couch position with the closest tidal volume and its accompanying airflow as the reference template.

### 6.2.3. Model fitting

The registration process typically resulted in a set of 25 (*x,y,z*) locations for each evaluated point, along with the tidal volume and airflow corresponding to the acquisition time for each scan. The positions, tidal volumes, and airflows were fit to the motion model, employing the Nelder-Mead Optimization Algorithm described in Chapter 3 by minimizing the root-mean least-squares average distance between the fitting and measurements.

$$\min_{\vec{X}_0,\vec{\alpha},\vec{\beta}\in\Re^3} \sum_{i=1}^{25} \left\| \vec{X}_i - \vec{X}_0 - \vec{\alpha}V_i - \vec{\beta}f_i \right\| \tag{6.1}$$

where $\vec{X}_i$ was the $i^{th}$ location of 25 measurements, and $V_i$ and $f_i$ were the tidal volume and airflow, respectively, for scan *i*. In equation 1.1, $\vec{X}_0$, $\vec{\alpha}$ and $\vec{\beta}$, vectors in $\Re^3$, were the overdetermined fitting parameters. Considering three independent components for each vector, nine parameters were determined by 75 measurements (25 sets of $\vec{X}_i$).

One drawback with the Nelder-Mead method was that, like other multidimensional unconstrained optimization algorithms, it occasionally located a local minimum. To overcome this drawback and minimize the discrepancy of fitting, the fitting process was repeated at the current best point[65] until the difference of discrepancies between two consecutive fitting operations fell below 5% of the discrepancy obtained from the previous fitting operation.

## 6.3. RESULTS

Fig. (6.1) shows the registration error of the NCC registration method used in this study. Registration error was defined as the discrepancy between the displacement given by the registration and that given by manual tissue tracking. 100 landmarks were selected in the inferior portion of lung from five patients. The motion magnitudes of landmarks ranged from 10mm to 30mm. The mean registration error was 1.32mm.

Fig. (6.2) and Fig. (6.) show the coronal and sagittal planar samples of $|\vec{\alpha}|$ and $|\vec{\beta}|$ in the left and right lungs of one patient with lung cancer. $|\vec{\alpha}|$, in units of millimeters per liter, represents the displacement of the tissue in the lung after inhaling one liter. $|\vec{\beta}|$, with units of millimeters per liter per second, represents the tissue motion hysteresis at an airflow of one liter per second. For this patient, the $85^{th}$ percentile tidal volume was 665.0 ml and the airflow varied from –309.1 ml/s to 280.8 ml/s.

The result showed that $\vec{\alpha}$ was greater in the inferior and posterior portions of the lungs and smaller in the superior and anterior portions of the lungs. The craniocaudal component of $\vec{\alpha}$ dominated the displacement of the motion during the breathing cycle.

$\vec{\beta}$ was greater in the lateral lungs. This pattern of $|\vec{\alpha}|$ and $|\vec{\beta}|$ distribution were observed in 44 out of 49 patients and was therefore defined as the normal pattern.

Fig. (6.4) and Fig. (6.5) showed the coronal and sagittal projection of $|\vec{\alpha}|$ and $|\vec{\beta}|$ in the left and right lung of a patient that had an abnormal motion pattern. For this patient, the 85$^{th}$ percentile tidal volume was 460.1 ml and the airflow varied from –300.0 ml/s to 327.8 ml/s.

For this patient, in the right lung, $|\vec{\alpha}|$ was greater in the inferior and posterior portions while $|\vec{\beta}|$ was greater in the lateral lung. Both were similar to what was observed in the normal case. However, $|\vec{\alpha}|$ and $|\vec{\beta}|$ exhibited a different pattern in the left lung. Fig. (6.4) shows that $|\vec{\alpha}|$ was greater in the superior and anterior portions of the left lung. Fig. (6.5) shows that $|\vec{\beta}|$, instead of being greater in the lateral lung, was greater in the superior portion of the left lung, as indicated by arrows. The craniocaudal component of $\vec{\alpha}$ dominated the displacement of the motion during the breathing cycle. CT images reconstructed at a series of tidal volumes showed that the size of the left lung was only half of the size of the right lung, and the left diaphragm barely moved during respiration. The dysfunction of left diaphragm caused the left lung breathing to be dominated by chest expansion, so the lung expanded in the anterior-posterior direction, which was well modeled by $\vec{\alpha}$.

Of the 49 patients, $|\vec{\alpha}|$ reached its maximum in the anterior lung in three patients, while for two other patients, $|\vec{\alpha}|$ was greatest in the lateral lung. For 45 out of 49 patients, $|\vec{\alpha}|$ reached its maximum in the inferior and posterior portions of the lungs. The hysteresis motion $\vec{\beta}$ had greater variability, but for the majority of patients, $|\vec{\beta}|$ was greatest in the lateral lungs.

The values of $|\vec{\alpha}|$ and $|\vec{\beta}|$ are three dimensional scalar fields, so a histogram of the 85$^{th}$ percentile values was selected to describe the inter-patient variability. Fig. (6.6) shows the histogram of the 85$^{th}$ percentile of $|\vec{\alpha}|$ and $|\vec{\beta}|$ in all of the patients. The mean 85$^{th}$ percentiles of $|\vec{\alpha}|$ in the left and right lungs were 23.2 mm/l and 26.1 mm/l, respectively. The mean 85$^{th}$ percentiles of $|\vec{\beta}|$ in the left and right lungs were 3.7 mm·s/l and 3.6 mm·s/l, respectively.

Fig. (6.7a) shows the cumulative histogram of discrepancies between the modeled and measured locations of all 49 patient datasets. The result indicated that for 80% of the lung tissues, the discrepancies were less than 1.75 mm, and for 90%, less than 2.14 mm. Fig. (6.7b) shows the cumulative histogram of relative discrepancies for motion magnitudes greater than 15 mm. The relative discrepancy was defined as the ratio of the discrepancy to the motion magnitude. For tissues where the overall motion was greater than 15mm, 78% and 96% of the lung tissue positions had less than 10% and 15% relative position

discrepancies, respectively. Fig. (6.7c) and Fig. (6.7d) shows the cumulative histograms of relative discrepancies for motions between 10 mm and 15 mm and motions between 5mm and 10mm.

## 6.4. DISCUSSION

This is the first report of the 3-dimensional breathing motion model parameters for a large cohort of patients. The overall $|\vec{\alpha}|$ and $|\vec{\beta}|$ maps varied smoothly as expected. $\vec{\alpha}$ and $\vec{\beta}$ described different breathing motion characteristics. $\vec{\alpha}$ modeled local lung expansion and could be interpreted as the breathing motion as if the patient breathed infinitely slowly. $\vec{\beta}$ modeled the hysteresis motion which was hypothesized to be caused by the dynamics of breathing. The relative magnitudes of $\vec{\alpha}$ and $\vec{\beta}$ are major determinates of the motion path eccentricity. In general, regions that had greater values of $|\vec{\beta}|$ corresponded to regions with greater $|\vec{\alpha}|$. These results showed that the majority of patients exhibited similar $|\vec{\alpha}|$ maps. The $|\vec{\beta}|$ maps showed greater inter-patient variability with the common feature that $|\vec{\beta}|$ was greater in the lateral lungs.

The utility of the proposed breathing motion model is to non-invasively monitor and predict the motion of lung tissues and tumors using only external surrogates. The positions of any piece of lung tissue were hypothesized to be determined by the tidal volume and airflow. The implication of this hypothesis was that the position of a specific piece of tissue or tumor would be at the same location if given the same tidal volume and

airflow, regardless of the point of time. It has been shown that the position of tumors varies day-to-day at exhalation[21], in apparent contradiction to the model. The model, however, is based on tidal volume, which has a zero value at a selected percentile. This value is valid only for a single scanning or treatment session. To compare the positions of tissues between sessions, an absolute lung volume surrogate would be required, for example, the total air content. Rather than measure the total air content, the position of a piece of tissue, using an implanted surrogate for example, could be used to shift the tidal volume definition to correspond to the original 4D CT session.

Although airflow is the time derivative of tidal volume, the breathing motion model is an explicit function only of tidal volume and airflow. The tidal volume and airflow are themselves functions of real time. The assumption is made that a first-order relationship between the displacement and the surrogates will meet the clinical requirement in precision of dose delivery or treatment planning. For this study, 25 scans were acquired and good agreement between the measurements and the predictions from the breathing motion model was observed when the motion was greater than 15 mm, as illustrated in Fig. (6.7b), with more than 90% of the points having less than 15% relative discrepancy. Since the average registration error in this study is 1.32mm as illustrated in Fig. (6.1), and is quite constant over widely varying motion magnitudes, the registered trajectory tends to be more relatively dispersive in less active points, as the registration error gains more weight in the motion magnitude that is relatively small. Therefore it is not surprising that the model performs worse for points that move less, as illustrated in Fig. (6.7c) and Fig. (6.7d). However 90% of the points still exhibited better than 2 mm agreement.

In this study, 25 scans were acquired for each couch position while the breathing motion model had only 9 independent parameters. Theoretically, 3 scans acquired at different tidal volumes and airflows would have provided sufficient motion data to fit the model parameters. Errors in registration and motion-induced image artifacts would still cause errors in motion parameter determinations. The use of additional CT scans was expected to reduce the impact of individual registration errors, but at the cost of dose to the patient. The minimum number of scans and optimization of the breathing phases of those scans remains an open question.

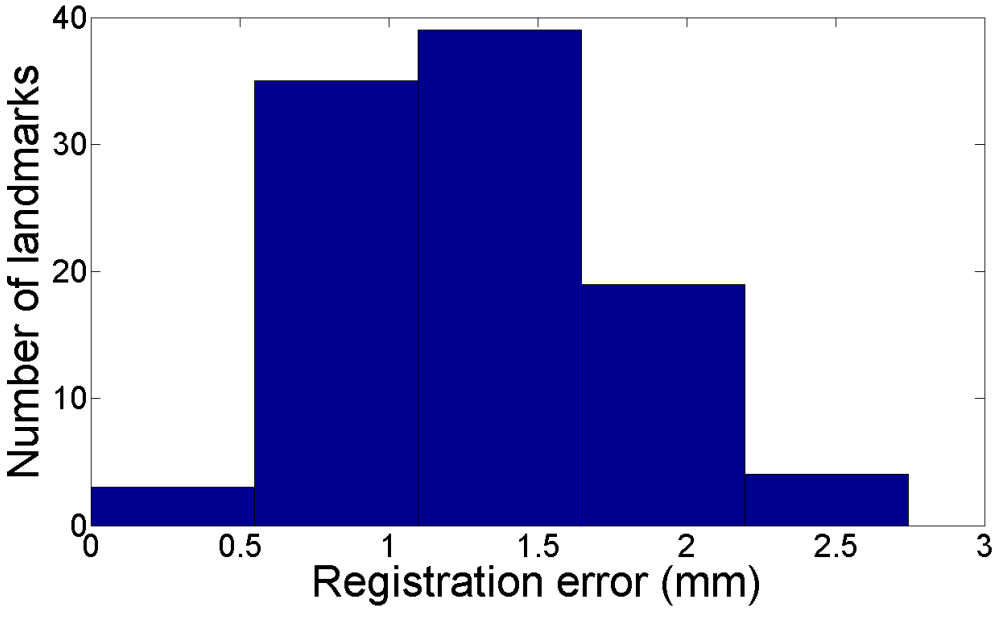


Fig. 6.1: The registration error of the normalized cross-correlation registration method employed

in this study. The registration error is defined as the discrepancy between the displacement fields given by the registration method and manual tracking. 100 landmarks selected in the inferior part of lung from five patients were tracked and manually compared. The motion magnitudes of these landmarks varied from 10 mm to 30 mm

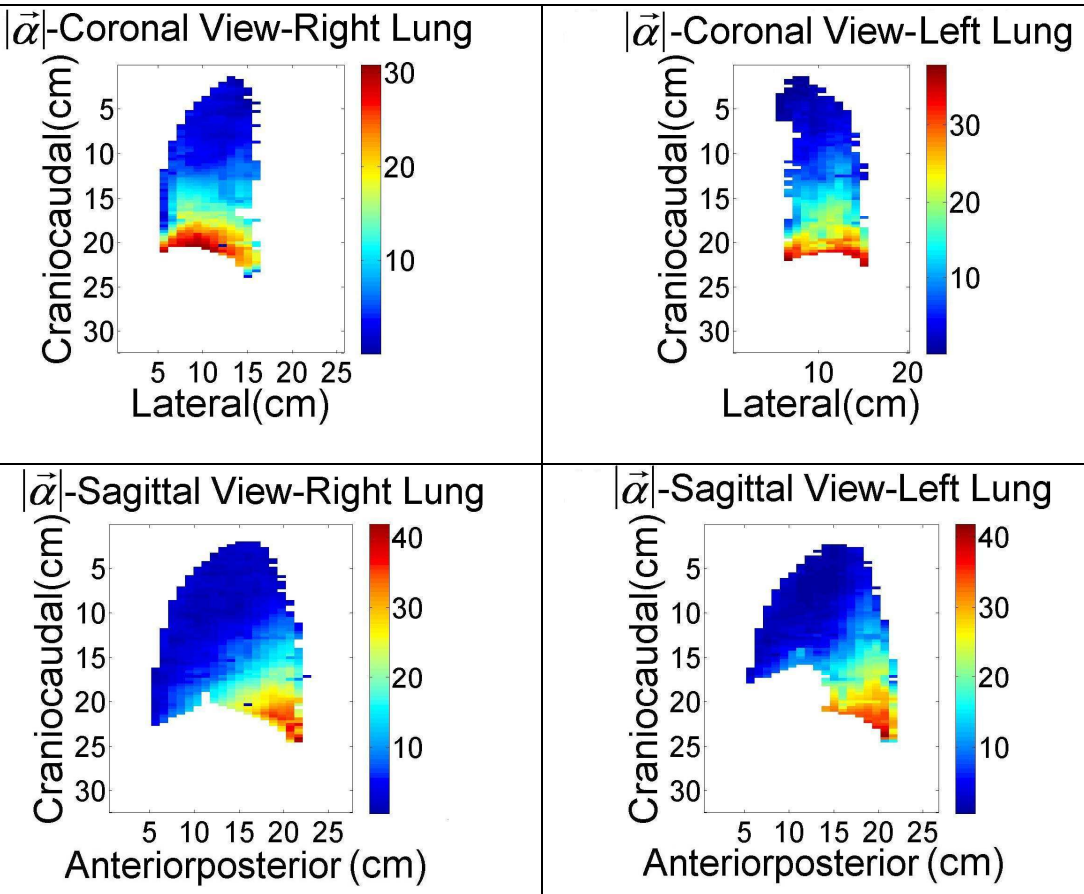


Fig. 6.2: Distribution of $|\vec{\alpha}|$ in a normal pattern

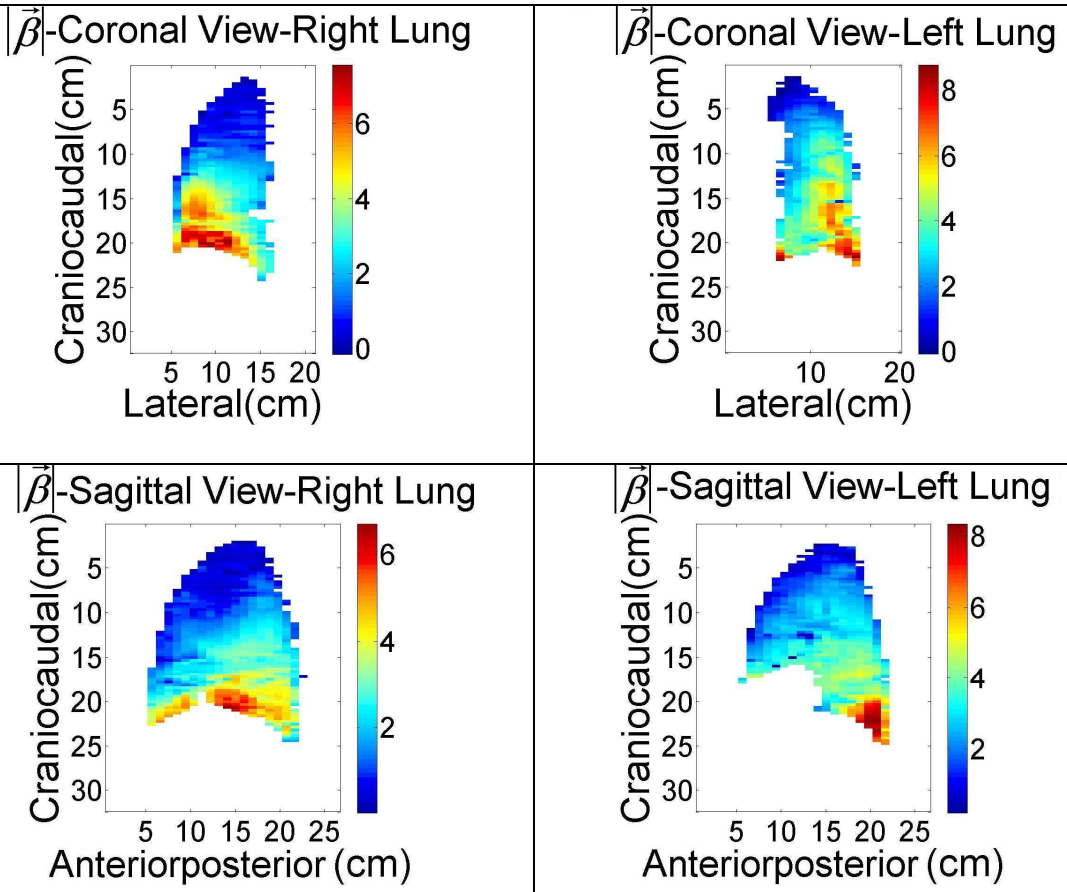


Fig. 6.3: Distribution of $|\vec{\beta}|$ in a normal pattern

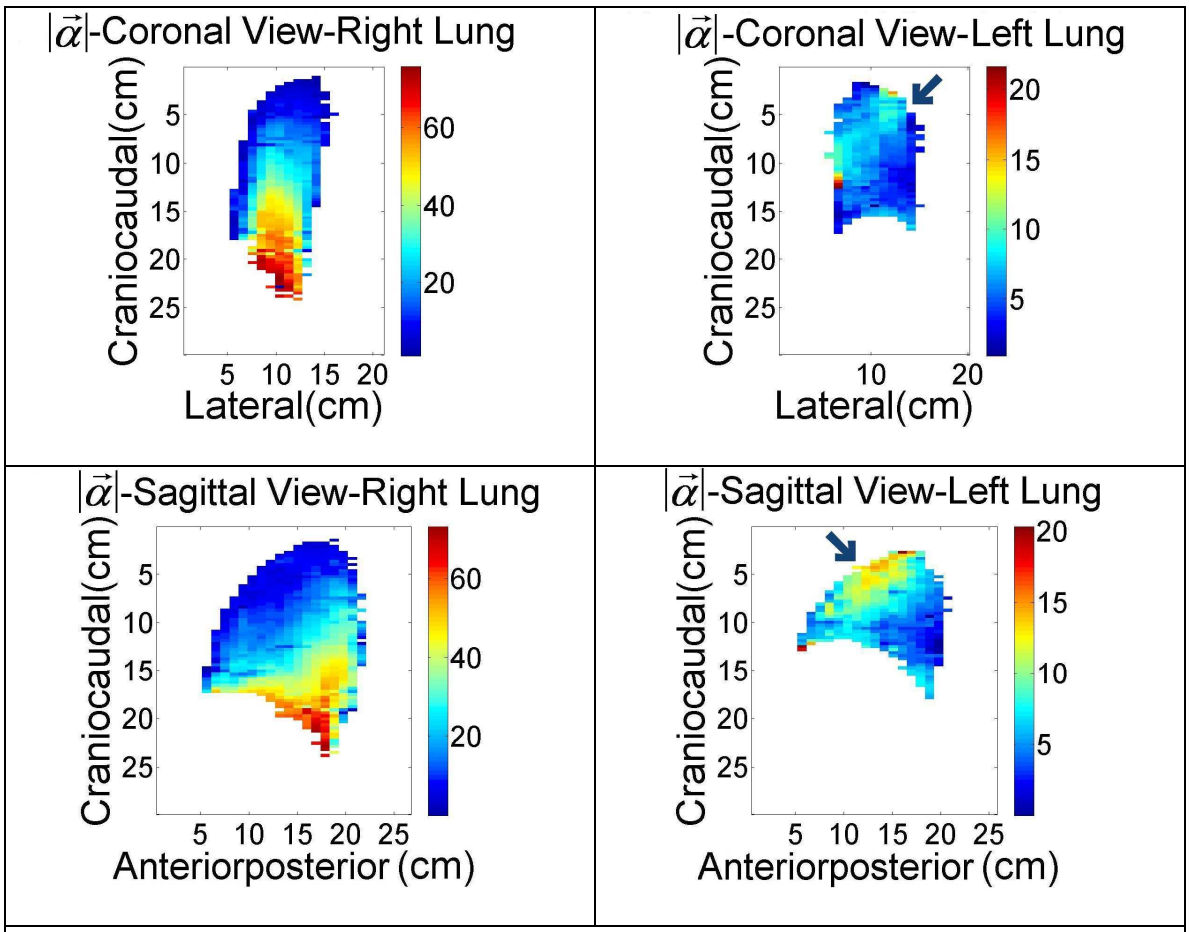


Fig. 6.4: Distribution of $|\vec{\alpha}|$ in an abnormal pattern

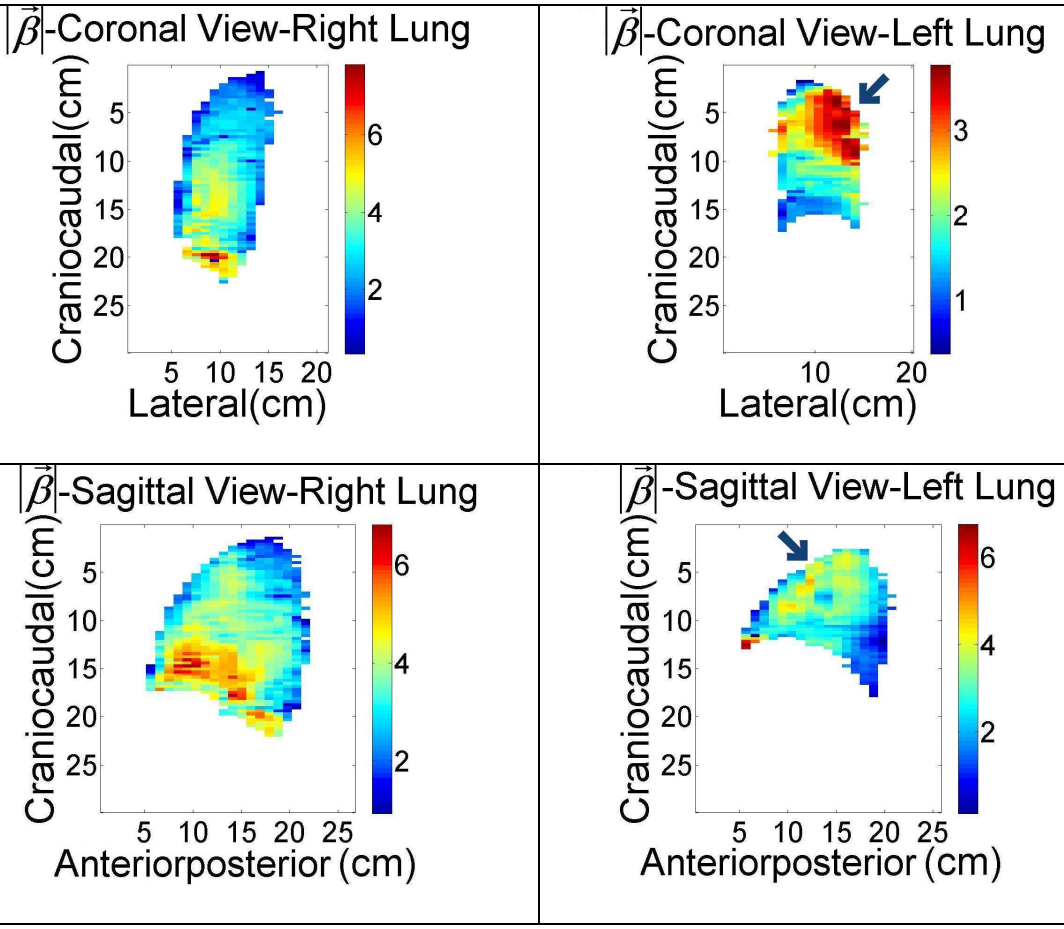


Fig. 6.5: Distribution of $|\vec{\beta}|$ in an abnormal pattern

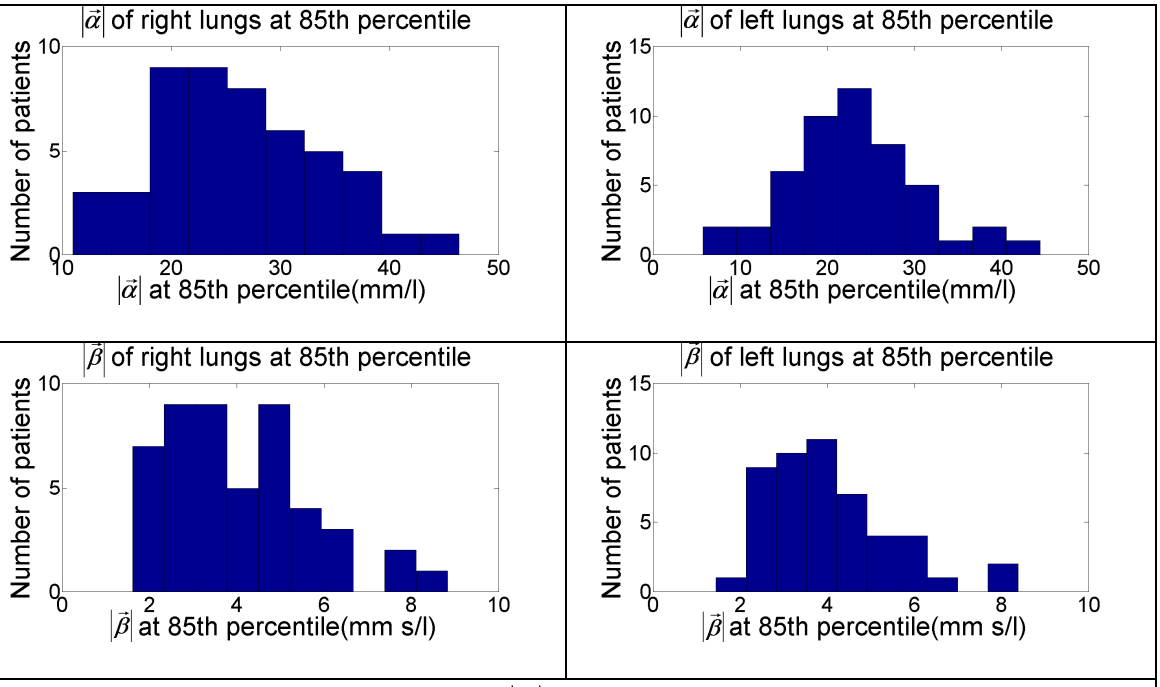


Fig. 6.6: Histogram of the mean $|\vec{\alpha}|$ and $|\vec{\beta}|$ at the 85$^{th}$ percentile for 49 patients.

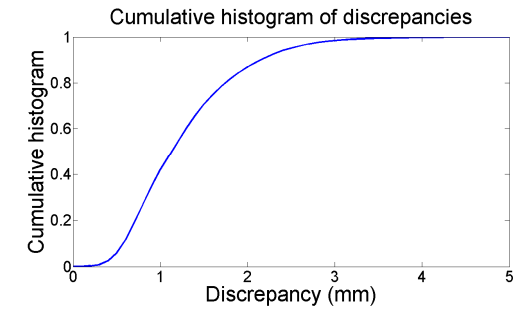


(a)

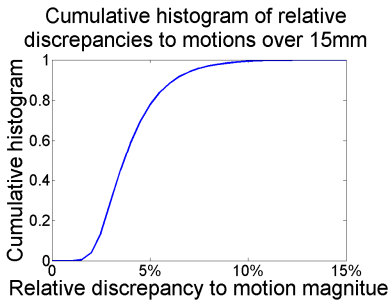


(b)

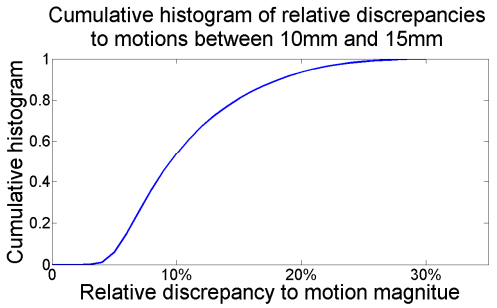


(c)

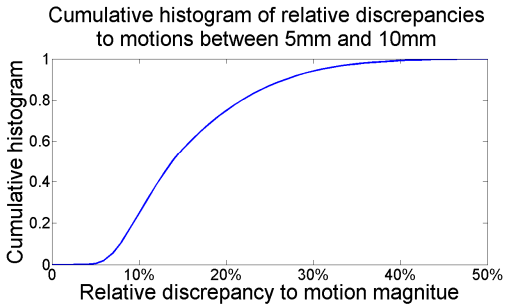


(d)

Fig. 6.7: (a) Cumulative histogram of discrepancies between measured and fit locations. (b) Cumulative histogram of relative discrepancies to motion magnitudes over 15mm. (c) Cumulative histogram of relative discrepancies to motion magnitudes between 10mm and 15mm. (d) Cumulative histogram of relative discrepancies to motion magnitudes between 5mm and 10 mm.

# Chapter 7

# Clinical Application

Anatomical and physiological evidences have shown that solid tumors in breast typically have greater firmness than the surrounding normal tissue[66]. This characteristic has been linked to the presence of abundant collagen in the tumor stroma, commonly referred to as the desmoplastic reaction[67]. A recent study by Ragavendra et al[68] further confirmed this phenomena in thyroid gland tumors. In Ragavendra's study, a 5-cm long and 25-gauge fine needle was repeatedly advanced and withdrawn through suspected tumor regions. The firmness of the tissue was evaluated and ranked by the nature and strength of the haptic force-feedback from the tumor due to tissue penetration. All the participants were categorized into two groups. Group 1 exhibited penetration resistance with a distinctive force-feedback; group 2 exhibited no resistance. Final cytological diagnoses were made after obtaining resistance information. Of 146 participants in group 1, 93 were diagnosed with tumor and 53 without tumor. Of 463 participants in group 2, 22 were diagnosed with tumor and 441 without tumor. The overall sensitivity was 0.81 and the overall specificity was 0.89. This result clearly indicated a high correlation between the firmness and the solid tumors.

Section 7.1 will discuss the potential clinical application of the free breathing lung motion model as auxiliary evidence in diagnosing lung tumor. The parameters in the

model were related to the biomechanical properties of lung in Chapter 5, where the corresponding biomechanical description of firmness is Young's modulus. The firmness of a tissue, which determines the extent of the tissue elasticity, has a direct impact on the stress distribution. Therefore, the escalation of firmness in cancerous regions would be reflected in the model parameters.

Section 7.2 will discuss the model stability. One of the central hypotheses of the free breathing lung motion model is that variations in the breathing cycle are explicitly considered because the model variables are tidal volume and airflow. Therefore, the model parameters should not change significantly except for a) disease progression or b) radiation damage and radiation response. A healthy subject (non-lung cancer) should exhibit little variation in the motion model parameters, especially the positions of parameter maxima and minima, corresponding to maximum and minimum breathing motion, respectively. The model parameters are directly related to the tissue motion, so an analysis of model parameter changes can be directly interpreted as changes in the motion magnitude.

Section 7.3 will discuss the monitoring of radiation damage using our model. We hope this study would give us more insight into the correlation between the radiation damage and the variation of lung density by examining the change of model parameters. Clinically, we hope this study would provide us timely update on the change of biomechanical properties of lung to assist in the evaluation of radiation damages.

Section 7.4 will discuss the application of the breathing motion model in removing breathing motion artifacts from Positron emission tomography (PET) images if the model is robust only within the time of the CT scan session

## 7.1 Distortion of $\vec{\beta}$ in Cancerous Region

In chapter 5, we have related the model parameters, $\vec{\alpha}$ and $\vec{\beta}$, to the normal stress distribution, Young's modulus and shear modulus in the lung.

$$\vec{\alpha}(\vec{x}_0) = \int_0^{\vec{x}_0} \frac{1}{E(\vec{x})} \left. \frac{\partial \vec{\sigma}_n(V, f_0, \vec{x})}{\partial V} \right|_{V=V_0} d\vec{x} \tag{7.1}$$

$$\vec{\beta}(\vec{x}_0) = \int_0^{\vec{x}_0} \frac{1}{E(\vec{x})} \left. \frac{\partial \vec{\sigma}_n(V_0, f, \vec{x})}{\partial f} \right|_{f=f_0} d\vec{x} + \int_0^{\vec{x}_0} \frac{1}{G(\vec{x})} \left. \frac{\partial \vec{\tau}_n(f, \vec{x})}{\partial f} \right|_{f=f_0} d\vec{x} \tag{7.2}$$

where $\vec{\sigma}_n$ is the normal stress and $\vec{\tau}_n$ is the shear stress. $E$ is the Young's modulus and $G$ is the shear modulus. Both Young's modulus and shear modulus are the indicators of tissue firmness. A solid tissue usually comes with higher Young's modulus and shear modulus. Hence Young's modulus and shear modulus are related to the local expansibility and deformability of the tissue. Abrupt change of the elastic modulus is also expected around the boundary of cancerous region. Since $\vec{\alpha}$ and $\vec{\beta}$ is accumulative along the path from the reference point which is defined as the fixed point in the lung during respiration, the influence of tissue stiffness on the amplitudes of $\vec{\alpha}$ and $\vec{\beta}$ would be swallowed in the integral. However, the directions of $\vec{\alpha}$ and $\vec{\beta}$ are different stories. The escalation of Young's modulus and shear modulus in the cancerous region reduces the contribution of that region to $\vec{\alpha}$ and $\vec{\beta}$. As the integral approaches the cancerous

region, weight of contributions from regions with lower Young's modulus and shear modulus would increase, and weight of contributions from cancerous regions would drop. Although the magnitude of $\vec{\alpha}$ and $\vec{\beta}$ barely changes because the integral, the directions of $\vec{\alpha}$ and $\vec{\beta}$ would turn to regions with lower Young's modules and shear modulus.

Fig (7.1) showed the coronal views of $\vec{\alpha}$ and $\vec{\beta}$ in one patient with NSCLC. The red triangle indicates the tumor position. The color bar on the right side of the figure indicates the magnitude of $\vec{\alpha}$ and $\vec{\beta}$, in unit of $mm/L$ and $mm \cdot s/L$, respectively. A mild distortion in the $\vec{\alpha}$ direction exists near the tumor. For $\vec{\beta}$, a very clear distortion in its direction exists near the tumor.

The flow of $\vec{\beta}$ appeared to avoid or escape from the cancerous region, similarly to the way that water in a river flows around a rock. The distortion in the $\vec{\beta}$ direction can be explained by its two orthogonal components, $\vec{\beta}_1$ and $\vec{\beta}_2$. As discussed in Chapter 5, $\vec{\beta}_1$ is parallel to $\vec{\alpha}$, the displacement of the tissue contributed by infinitely slow filling of air. Along the boundary of the cancerous region, $\vec{\beta}_1$ is constrained by the firmness of the tumor simply because the tumor is more resistant to stretching or squeezing than the surrounding normal tissue, while $\vec{\beta}_2$, which is parallel to $\vec{\alpha}$, is barely affected. As the relative contribution of $\vec{\beta}_2$ increases relative to $\vec{\beta}$, it would tend to divert $\vec{\beta}$ toward the direction that is perpendicular to $\vec{\alpha}$ from its original direction at the absence of tumor.. Fig. (7.2) shows more examples of the distortion of $\vec{\beta}$ around the tumor.

The significance of this study is that the breathing motion model is potentially capable of aiding cancer diagnosis by visualizing the suspicious cancerous region at the distortion of model parameters.

## 7.2 Model Stability

The utilization of the motion model depends on its stability over time. If the breathing motion model parameters change significantly between sessions (either imaging or treatment), the specific motion model would be useful only for single-session activities, such as removing motion artifacts from nuclear medicine images. If the motion model parameters are stable for weeks, exclusive of disease progression or treatment response, it would be useful for supporting radiation therapy treatment planning, including optimization of linear accelerator gating windows. If the model is proven to be stable over timescales consistent with the course of radiation therapy, changes in the model parameters might be used to monitor disease progression or radiation response.

We are currently recruiting patients with healthy lungs to determine the motion model stability. So fare we only have one subject. Fig. (7.3) was the coronal view of $|\vec{\alpha}|$ calculated from 2 scans that were acquired two weeks apart from that patient. Fig. (7.4a) was the histogram of $|\vec{\alpha}|$ variation between two scanning sessions. The $|\vec{\alpha}|$ variation ratio is defined as

$$\mathrm{var}(x) = \left| \frac{I_1(\vec{x}) - I_2(\vec{x})}{I_1(\vec{x}) + I_2(\vec{x})} \right| \tag{7.3}$$

where $I_1(\vec{x})$ and $I_2(\vec{x})$ are the values of model parameter of the same tissue in two scanning sessions. Fig. (7.4b) was the cumulative histogram of $|\vec{\alpha}|$ variation ratios. The shape of the $|\vec{\alpha}|$ distribution was similar between the two scan sessions, with 84% of $|\vec{\alpha}|$ varying by less than 20% from the first session to the second session. The $|\vec{\alpha}|$ distribution on the left lung appeared to be more consistent, with 95% of $|\vec{\alpha}|$ varying by less than 20% between two scanning sessions. Fig. (7.5) showed the coronal view of $|\vec{\beta}|$ in the two scans and Fig. (7.6) showed the histogram of $|\vec{\beta}|$ variation ratios and the cumulative histogram. Although the shapes of $|\vec{\beta}|$ distributions were similar, large variations were observed in the magnitude of $|\vec{\beta}|$, with only 53% of $|\vec{\beta}|$ varying by 20% or less between two scanning sessions.

Since there is only one subject with healthy lung has been recruited and studied, it is too early to draw a conclusion on the stability of the breathing motion model over weeks, especially given the facts that the registration is compromised by the image artifacts in the first scan. Similar scans from a two lung cancer patients has also exhibited little change in $|\vec{\alpha}|$ and $|\vec{\beta}|$. As more patients are imaged, we will soon accumulate enough evidence to test our hypothesis on the model stability over the timescale of weeks. If inconsistencies are observed in most of the subjects, the uncertainties in the model will be quantified.

## 7.3 Radiation damage monitoring

As we discussed in section 7.1, the magnitudes of $\vec{\alpha}$ and $\vec{\beta}$ are not clear enough to distinguish tumors from normal tissues because the magnitudes of $\vec{\alpha}$ and $\vec{\beta}$ are accumulated along the path originating from the reference point. However, the spatial differences of $\vec{\alpha}$ and $\vec{\beta}$ reflect local expansibility and motion hysteresis and could be good indicators for any change in the biomechanical properties of lung. In this section, we will discuss the relationship between the lung density and divergences of model parameters. We hope this discuss in this section would lead to a scheme to monitor the radiation damage effectively in clinical application.

Radiation damage may occur after a patient receives radiation therapy or is exposed to products or substances containing radiation. It is the major side effect that patients receive from radiotherapy. If we can develop an effective and prompt method to monitor the damage from radiation treatment, it could help the physician to adjust the treatment plan for the patient developing radiation damage.

Radiation damage is usually accompanied by symptoms like cough, weight loss and disorder of lung function. We hypothesize that the model parameter obtained at various days would change dramatically in patients who are undergoing radiation damages.

A coarse relationship between the divergence of $\vec{\alpha}$ and the lung density was discussed in Chapter 4, given the condition that airflow keeps constant during respiration. A general equation that applies at any tidal volume and airflow developed below.

As we have demonstrated in Chapter 4 that the relationship between the tissue velocity and the tissue density is given by

$$\rho\vec{\nabla}\bullet\vec{U}=-\frac{d\rho}{dt} \tag{7.4}$$

The hypothesis in our lung motion model is that the motion is a function of tidal volume and airflow. Although tidal volume and airflow evolve with time, time only serves as an implicit variable. Therefore, applying the chain law on both sides, Eq. (7.4) now expands to,

$$\rho\nabla\bullet\left(\frac{\partial\vec{X}}{\partial V}\frac{dV}{dt}+\frac{\partial\vec{X}}{\partial f}\frac{df}{dt}\right)=-\left(\frac{\partial\rho}{\partial V}\frac{dV}{dt}+\frac{\partial\rho}{\partial f}\frac{df}{dt}\right) \tag{7.5}$$

Moving all items with tidal volume to the left side and all items with airflow to the right side, Eq. (7.5) is rewritten as,

$$\rho\nabla\bullet\frac{\partial\vec{X}}{\partial V}+\frac{\partial\rho}{\partial V}=-\frac{\rho\dot{f}}{f}\frac{\partial\vec{X}}{\partial f}-\frac{\dot{f}}{f}\frac{\partial\rho}{\partial f} \tag{7.6}$$

by replacing $\frac{dV}{dt}$ with $f$ and $\frac{df}{dt}$ with $\dot{f}$

Eq. (7.6) only holds when the airflow is not zero. The equation for zero airflow has been discussed in Chapter 4.

In a time evolving system, all variables are either explicitly or implicitly function of time, in which sense that all the variables are connected and dependant on time. In the lung motion model discussed in this dissertation, time is explicitly excluded. Images taken at close tidal volumes and airflow have not necessarily been acquired in close temporal

proximity. Tidal volume and airflow serve as two independent variables in our lung motion model.

The density is an implicit function of time. Since time is excluded in our lung motion model, the involvement of time in our model is replaced by the tidal volume and airflow. We constrain the density to have the form

$$\rho(V, f) = \rho(V)\rho(f) \tag{7.7}$$

Plugging Eq. (7.7) into Eq. (7.6), we have

$$\rho(V)\nabla \bullet \frac{\partial \vec{X}}{\partial V} + \frac{\partial \rho(V)}{\partial V} = -\frac{\dot{f}\rho(f)}{f}\frac{\partial \vec{X}}{\partial f} - \frac{\dot{f}}{f}\frac{\partial \rho(f)}{\partial f} \tag{7.8}$$

Observe that the left side of the equation, denoted by $\lambda(V)$ is a function of $V$ only , and the right side of the equation, denoted by $\lambda(f, \dot{f})$, is a function of $f$ and $\dot{f}$. Since the values of $V$, $f$ and $\dot{f}$ are independent to each other, $\lambda$ must be constant.

$$\lambda(V) = \lambda(f, \dot{f}) = k \tag{7.9}$$

Since $\dot{f}$ is expected to vanish at end of inhalation and exhalation,

$$\lambda(f, \dot{f} = 0) = 0 \tag{7.10}$$

the only option left for $k$ is zero.

$$k = 0 \tag{7.11}$$

Therefore, Eq. (7.6) splits up to two equations,

$$\rho(V)\nabla \bullet \frac{\partial \vec{X}}{\partial V} + \frac{\partial \rho(V)}{\partial V} = 0 \tag{7.12}$$

and

$$\rho(f)\nabla \bullet \frac{\partial \vec{X}}{\partial f} + \frac{\partial \rho(f)}{\partial f} = 0 \tag{7.13}$$

Replacing $\vec{X}$ with $\vec{X}_0 + \vec{\alpha}V + \vec{\beta}f$ , Eq. (7.12) and Eq. (7.13) can now be written in terms of the motion model parameters,

$$\rho(V)\nabla \bullet \vec{\alpha} + \frac{\partial \rho(V)}{\partial V} = 0 \tag{7.14}$$

and

$$\rho(f)\nabla \bullet \vec{\beta} + \frac{\partial \rho(f)}{\partial f} = 0 \tag{7.15}$$

Eq. (7.14) and Eq. (7.15) govern the change of local density as a function of tidal volume and airflow during respiration. The hypothesis is, that the change of local density will keep constant if observed at two different points of time, presuming that no fundamental change happens in the time across the observations. However, if fundamental changes do happen to the lung, such as propagation of pulmonary disease or radiation damage, we hypothesize that the relationship between the variations of local density and model parameters will not remain constant at various points of time.

Fig. (7.7) shows the coronal views of $|\vec{\alpha}|$ obtained from one lung-cancer patient who was scanned at the middle of the treatment and at the end of the treatment. Fig. (7.8) shows the dose delivered to the patient during the whole treatment. The region that received radiation highly correlated the region where $|\vec{\alpha}|$ is obviously smaller that the remaining regions.

Fig. (7.9a) shows the profile of $|\vec{\alpha}|$ on a line that passes through the center of the right lung, shown in Fig. (7.3b), which was a healthy lung. Fig. (7.9b) shows the profile of $|\vec{\alpha}|$ on a line that passes through the center of the right lung, shown in Fig. (7.7a), which was a lung with tumor. Fig. (7.9a) shows that for a healthy lung, the $\vec{\alpha}$ divergence increased craniocaudally in a smooth way. However, for a lung received radiation, an abrupt escalation of $\vec{\alpha}$ divergence at the boundary of irradiated region was observed. This is shown in Fig. (7.9b) and indicates a suppression of $\vec{\alpha}$ divergence in the irradiated region and boosted $\vec{\alpha}$ divergence in the un-irradiated region, when compared against the healthy lung. This could be due to a redistribution of ventilation between irradiated and un-irradiated lung tissues.

Fig. (7.10) shows the comparison of $\nabla \bullet \vec{\alpha}$ between un-irradiated lung and irradiated lung. Fig. (7.10a) indicates that $\nabla \bullet \vec{\alpha}$ was slightly larger in the inferior portion of the lung. This agreed with the observation made by Ball et al [69] in 1962 that ventilation was more active in the inferior region of the lung than superior. However, Fig. (7.10b) showed that $\nabla \bullet \vec{\alpha}$ was much greater in the inferior than superior portion of the lung. Since the boundary of abrupt escalation of $\nabla \bullet \vec{\alpha}$ aligned with the boundary of delivered dose, we concluded that the dramatically deceased $\nabla \bullet \vec{\alpha}$ in the superior portion of the lung was caused by radiation that damaged the normal lung.

Currently, there is limited understanding of how much radiation will alter the lung density variation with respect to tidal volume and airflow, although evidence is being accumulated that hints that radiation compromises local tissue's function and alters its

biomechanical properties. If the damage happens in a region where a segmental bronchus passes by, it would cause symptomatic bronchial stenosis, the narrowing of the bronchi, which has been reported after the patients were exposed to high dose radiotherapy[70,71]. The narrowing of the bronchi usually occurs after the patients receive 60Gy. Poiseuille's law dictates that resistance in the airway is inversely proportional to the fourth power of the radius. Thus, even modest reductions may be sufficient to cause pulmonary symptoms. The normal function of the tissues whose ventilations are supplied through the compromised bronchus would suffer dramatically from shortage of ventilation, even there is no change qualitatively happens in that region. We hope, by verifying the correlation between model parameter divergences and radiation damage on more patients, the model could help us to find out how radiation damage develops during treatment and help us to visualize when and where the radiation damage takes place.

## 7.4 Breathing Motion Artifacts in Free Breathing PET Images

Positron-emission tomography (PET) scans provide unique functional imaging information with relatively poor spatial resolution. In contrast, CT scans provide whole body image in excellent spatial resolution within a few seconds. Integration of CT and PET offers the advantage of providing both metabolic and anatomical information, while improving both the sensitivity and specificity of malignant lesion detection[72].

One of the major drawbacks of PET imaging is the significant time required for image acquisition (up to 10 minutes per bed position). When scanning the thorax and upper

abdomen where breathing motion causes significant movement of tumors and normal organs, the attenuation, on which the scanner relies to generate the image, is the average attenuation instead of actual one. The incorrectly determined attenuation will cause inaccurate attenuation corrections and subsequently inaccurate PET radionuclide uptake. Generation of accurate attenuation maps requires a quantitative model of the breathing motion of the internal organs.

The restoration of tissue images can by done by applying the breathing motion model developed in this study, the relative positions of the target tissue are know for each breathing phase. The individual PET scan images can be deformably mapped and summed onto a single image dataset at a reference phase of breathing that has only residual (small) breathing motion artifacts. A phantom study was conducted to test the feasibility of this method for acquiring free-breathing thoracic PET images without breathing motion artifacts but with full statistics.

Data were collected using a Philips Brilliance and Siemens Biograph PET/CT scanners using list mode. Patient-modeled tumor trajectories were provided using a custom-fabricated 4D motion phantom shown in Fig. (7.11a). A spherical PET phantom with diameter of 1cm, shown in Fig. (7.11b), was used in this study, moved in a motion trajectory shown in Fig. (7.11c). The trajectory was subdivided into 10 bins of 8 mm width and the average location in each bin was denoted by a brown dot. The probability distribution of the phantom motion distribution was shown in Fig. (7.11d) in 20ms time units. There were two regions where the phantom did not pass (0% probability), but the

phantom passed a finite fraction of the time through remaining 8 regions. To synchronize the phantom and PET acquisition, a TTL synchronization signal was fed to the cardiac trigger channel. The trigger was activated when the phantom passed a user-determined spatial threshold and therefore provided an irregular but well-determined time pattern. The list mode was queried to determine the relative time of the cardiac triggers and this was used to synchronize the phantom position and the list mode data. PET events were selected from the list mode file according to which bin the phantom was in at the time of the PET event. This created 10 separate list mode files. Those list mode files were submitted to the commercial reconstruction software to reconstruct images using only events occurring in the corresponding bins. The reconstruction images were shifted by the known phantom displacement and summed. The subsequent image was compared against the known phantom shape to determine if the reconstruction was successful.

The gated reconstructions were compared against the ungated (original list mode file) reconstructions, showing significant improvement in the reconstructed phantom shape, both in Philips Brilliance and Siemens Biograph PET/CT scanners as shown in Fig. (7.12) Residual deformation was noted, consistent with the 8 mm wide gating window. This study indicates that the phantom shape can be restored by gating windows and shows promise in acquiring PET images in the thorax and upper abdomen without significant breathing motion artifacts if provided a quantitative breathing motion model

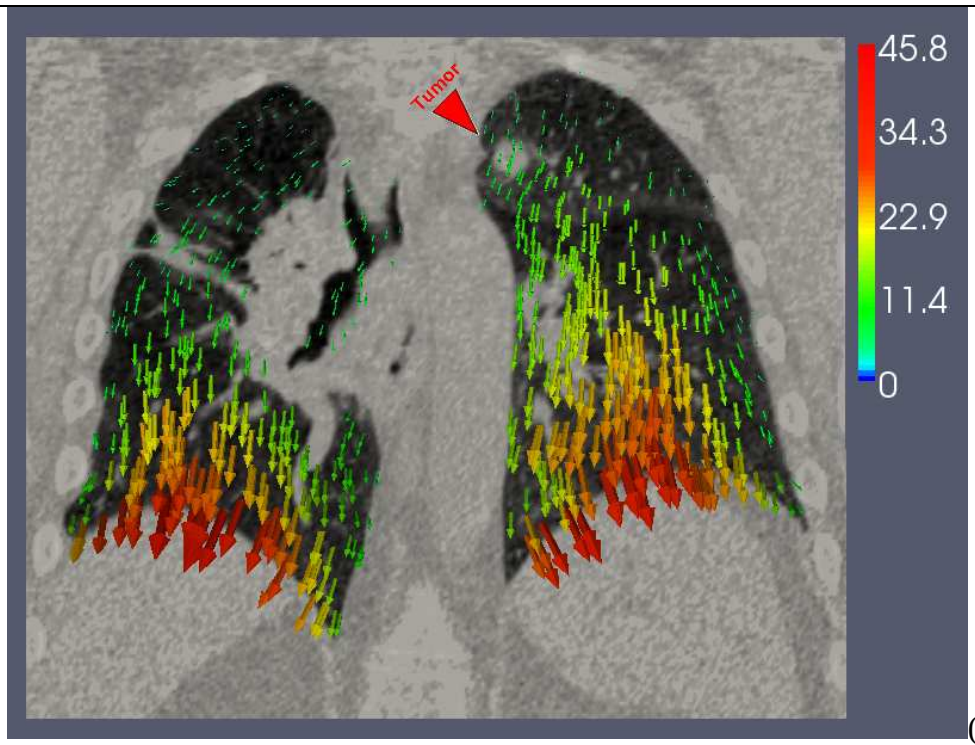


(a)

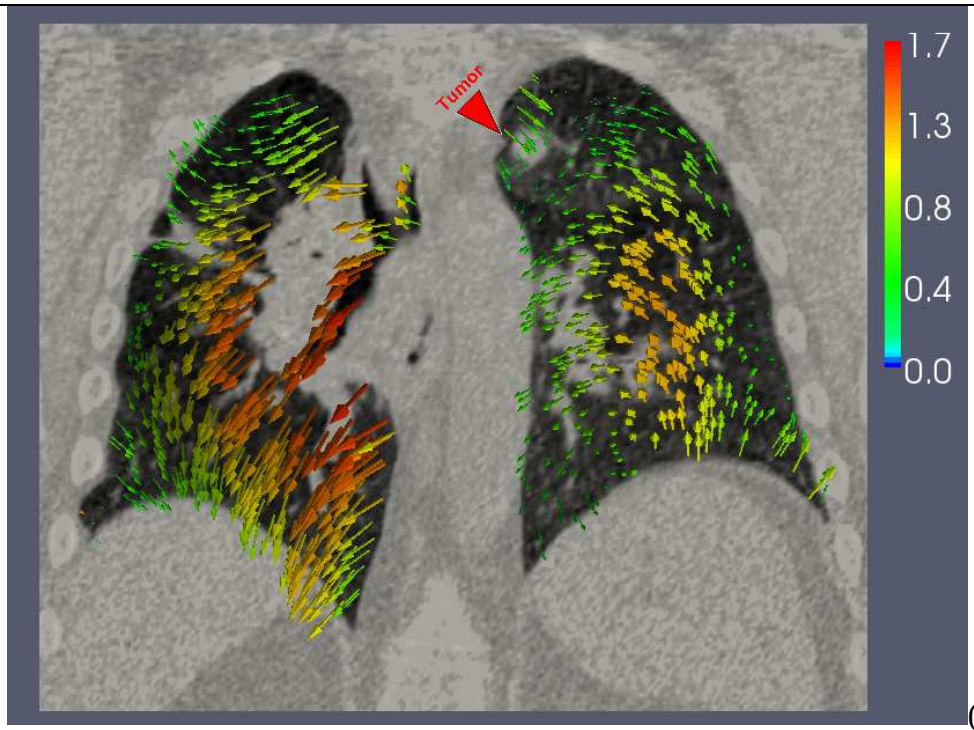


(b)

Fig.7.1(a) Coronal view of $\vec{\alpha}$ in a lung cancer patient (b) Coronal view of $\vec{\beta}$ in a lung cancer patient

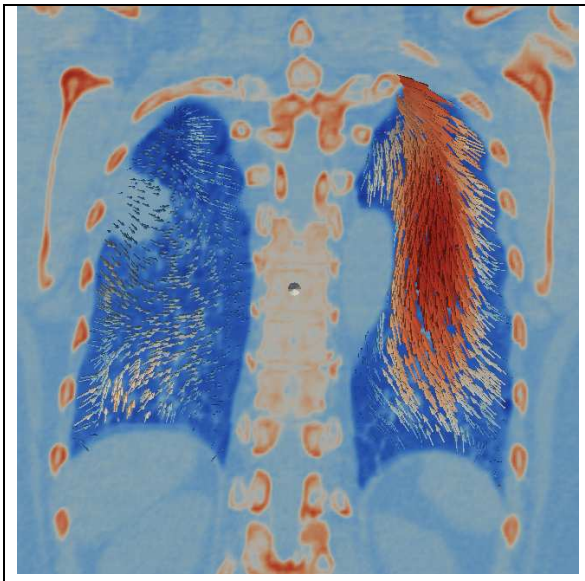

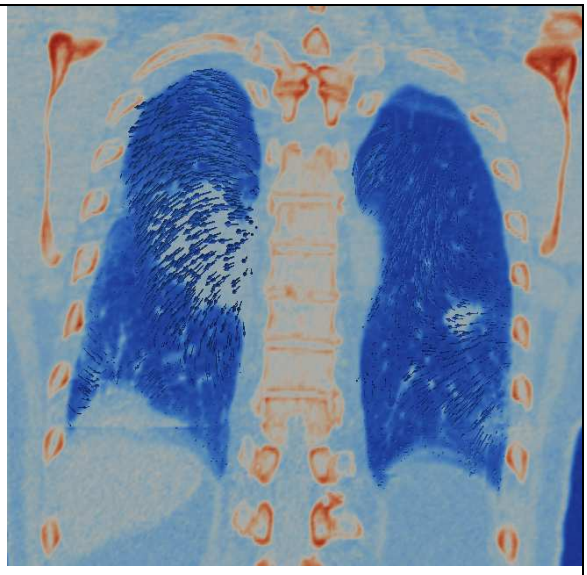

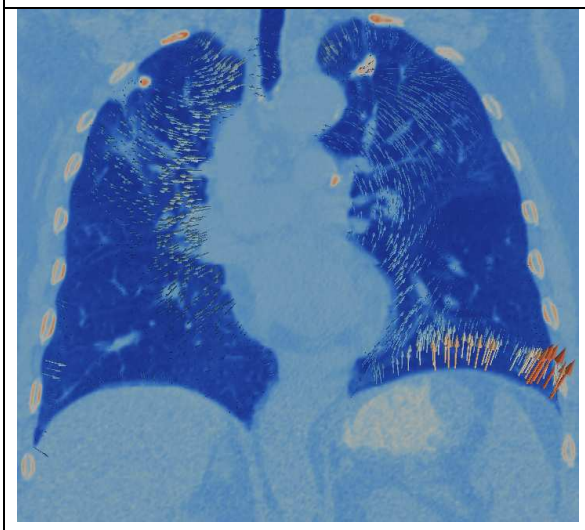

Fig. 7.2 More examples of $\vec{\beta}$ discontinuity around a tumor.

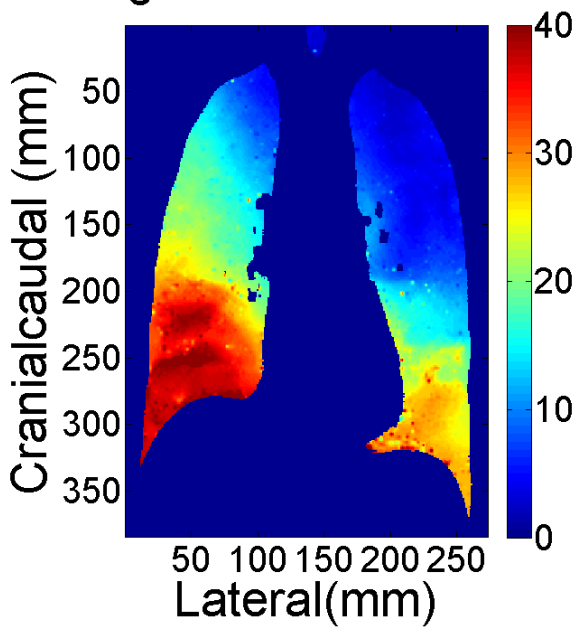


(a)

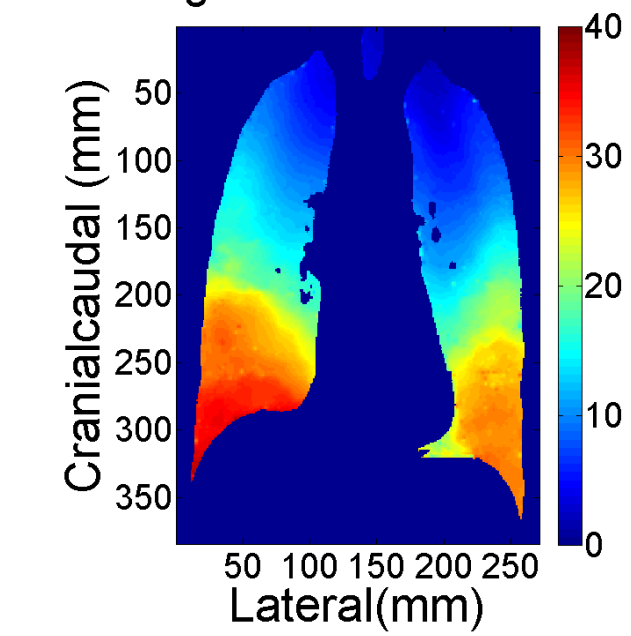


(b)

Fig. 7.3 $|\vec{\alpha}|$ distributions of the non-lung cancer patient scanned two weeks apart

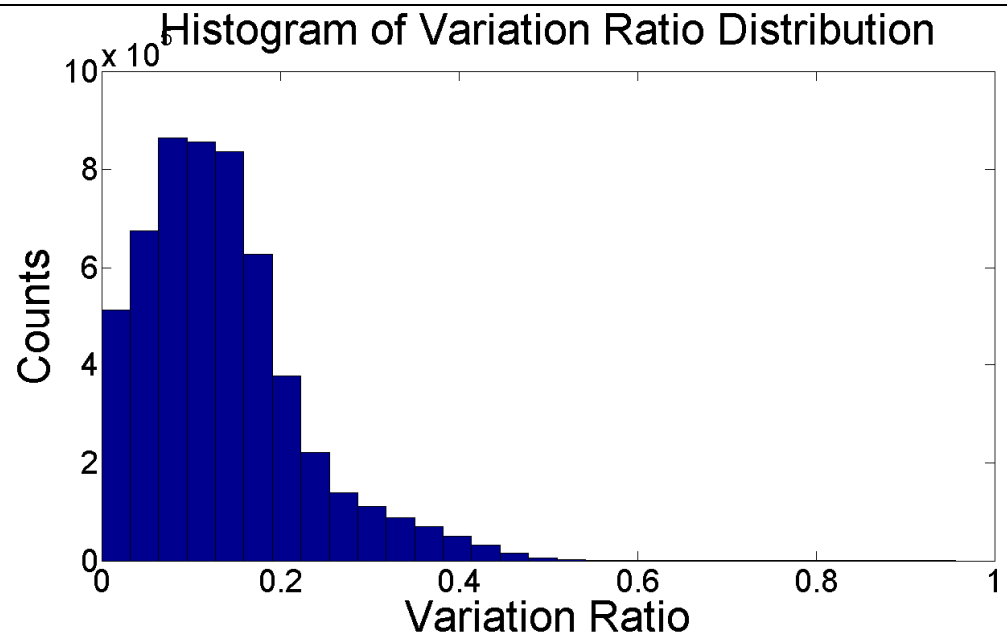


(a)

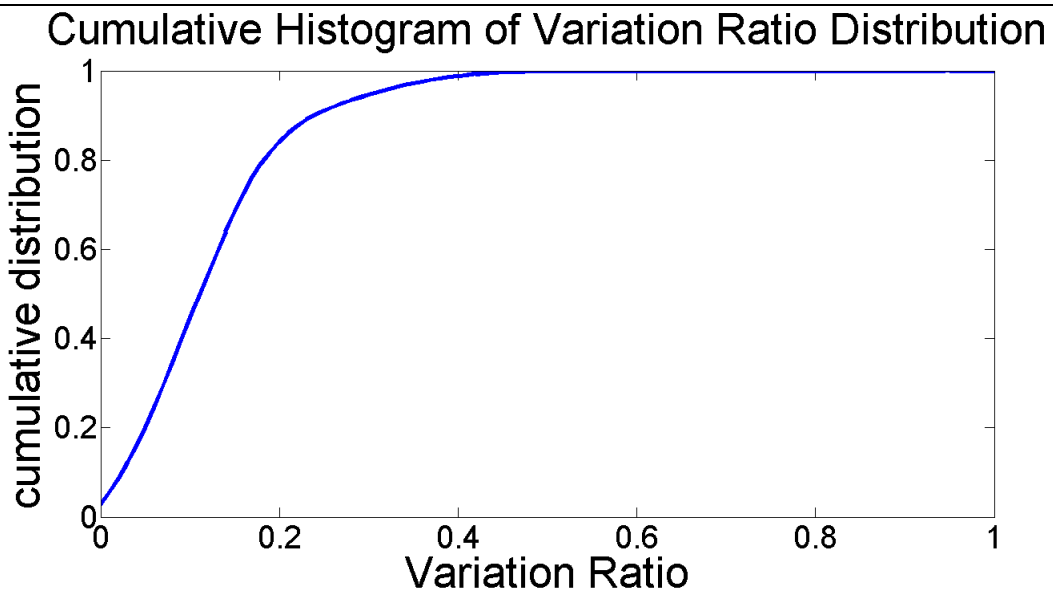


(b)

Fig. 7.4 Histogram of $|\vec{\alpha}|$ variation ratios between two scanning sessions

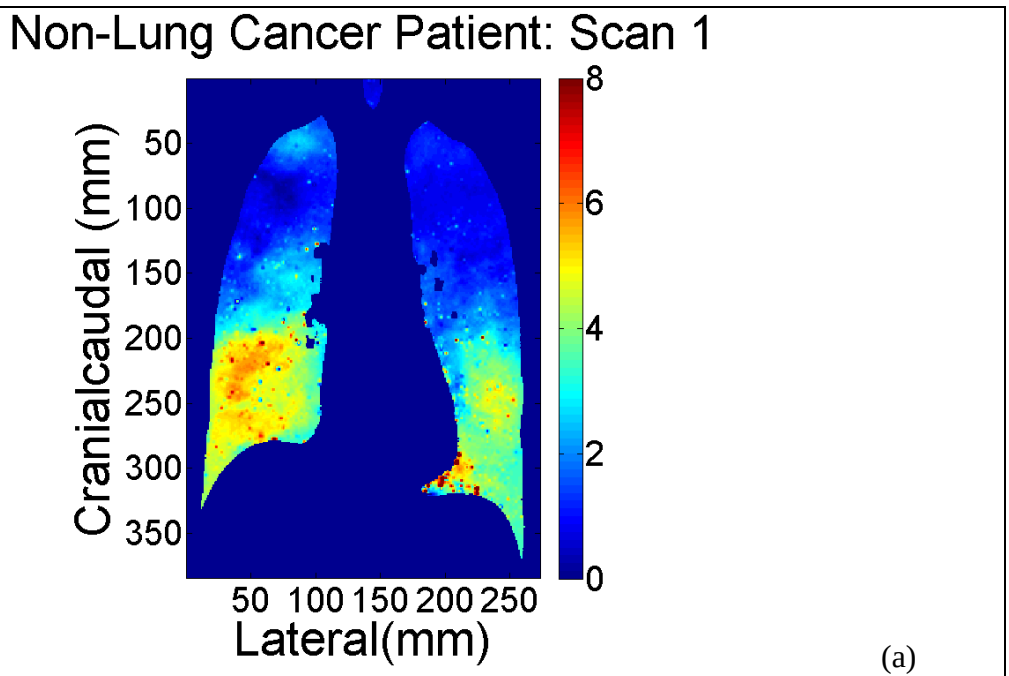


(a)

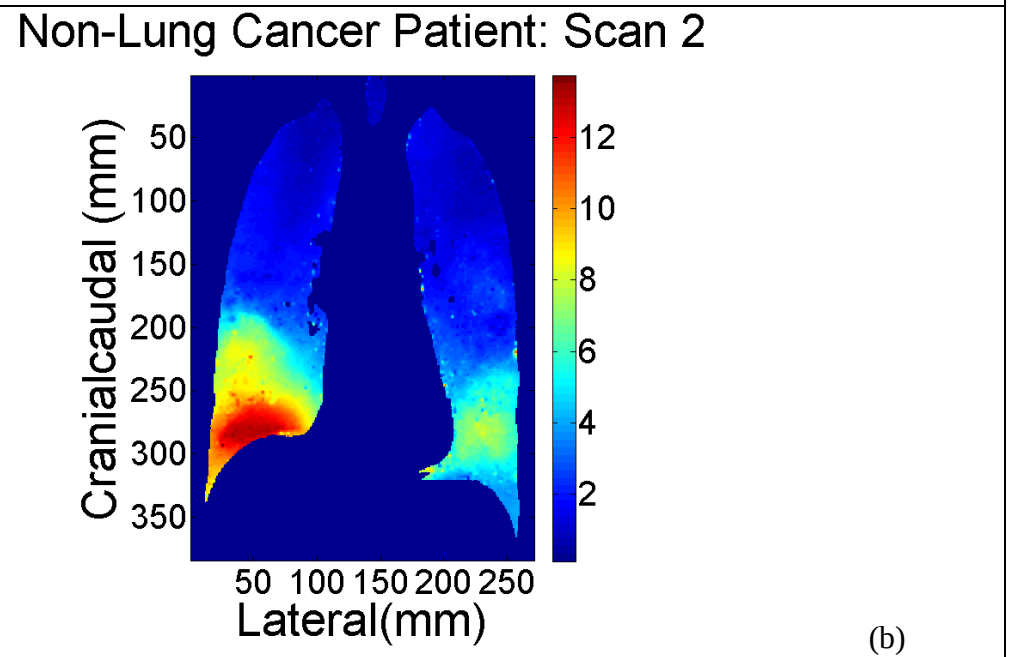


(b)

Fig. 7.5 $|\vec{\beta}|$ distributions of the non-lung cancer patient scanned two weeks apart

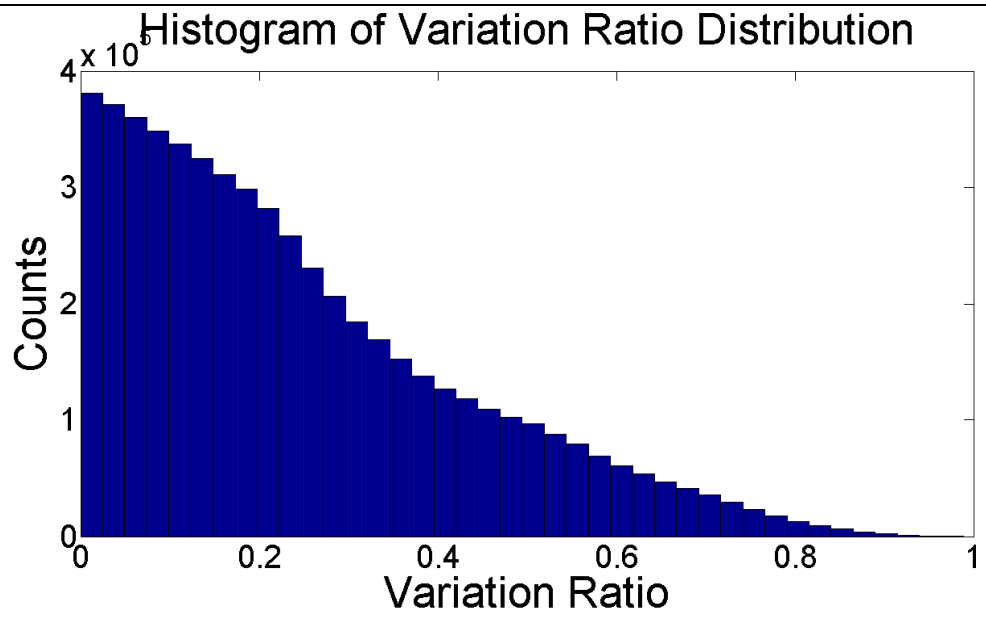


(a)

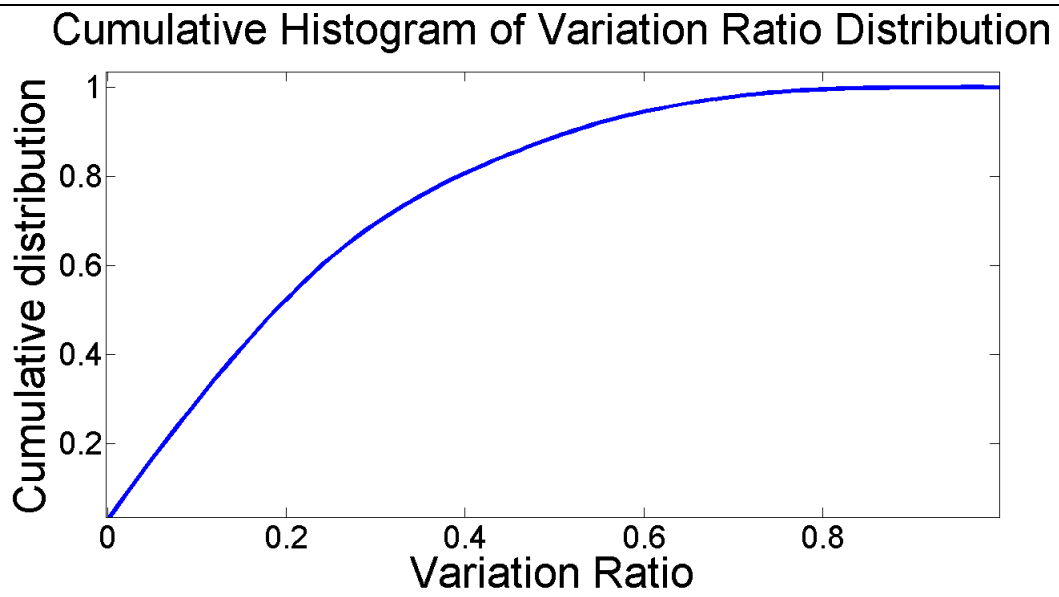


(b)

Fig. 7.6 Histogram of $\left|\vec{\beta}\right|$ variation ratios between two scanning sessions

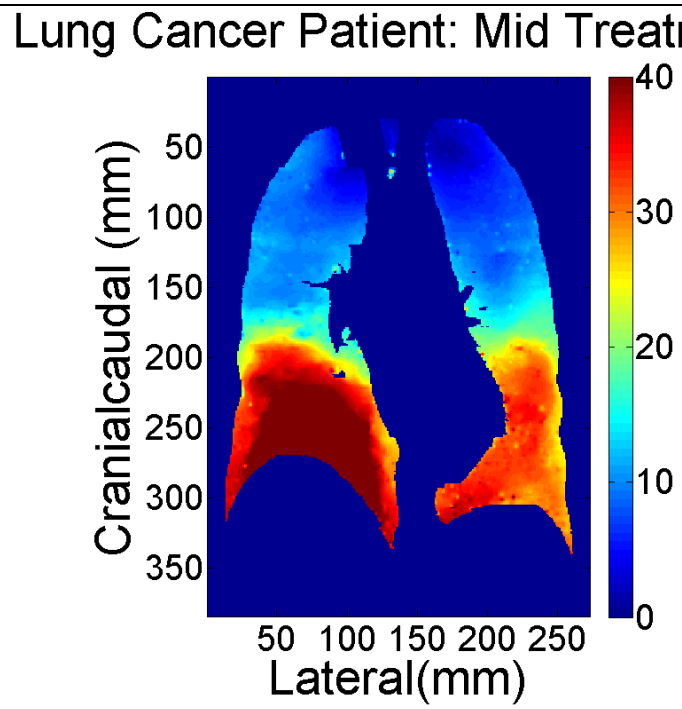


(a)

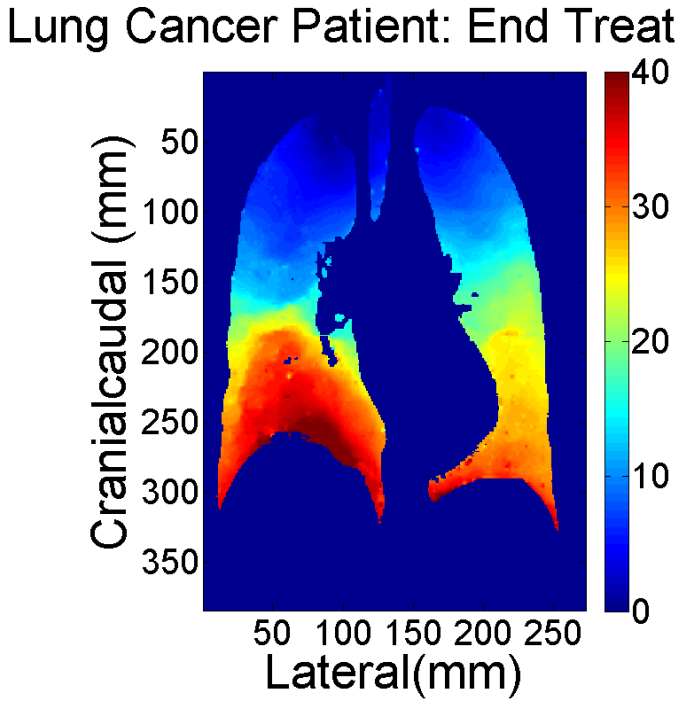


(b)

Fig. 7.7 $|\vec{\alpha}|$ distributions of one lung cancer patient scanned two weeks apart

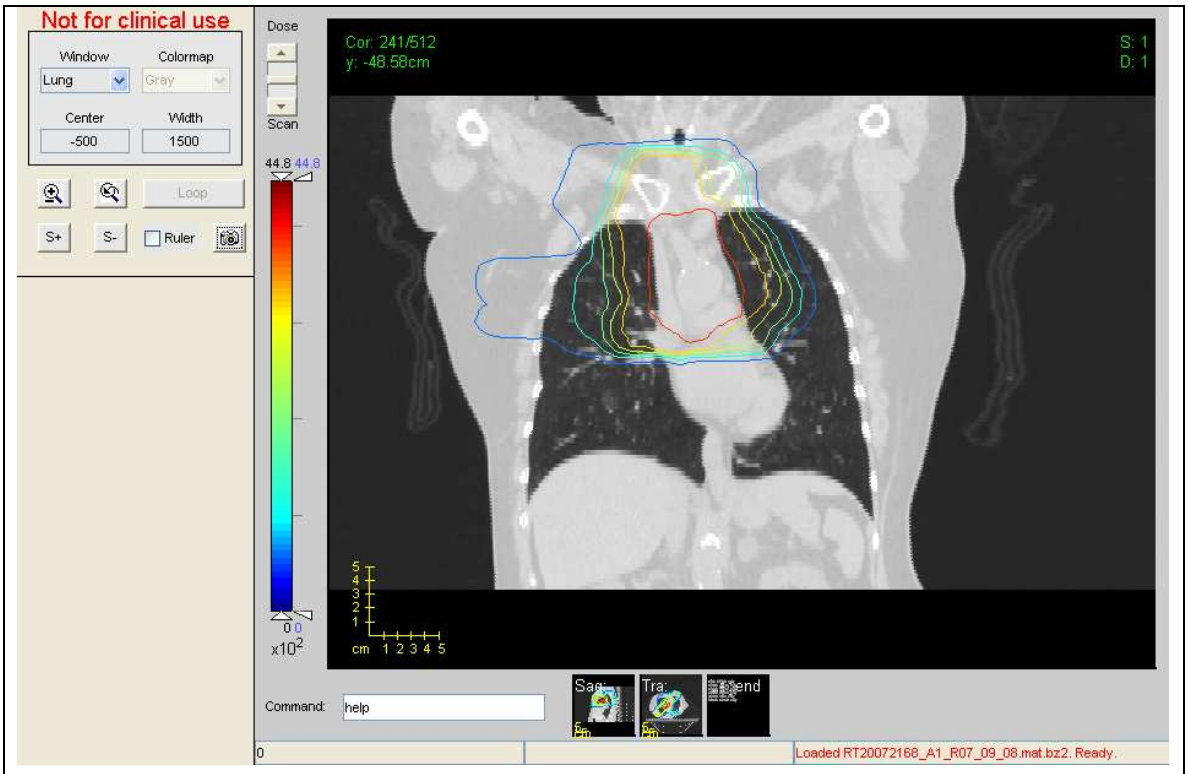


Fig. 7.8 Dose delivered to the lung cancer patient

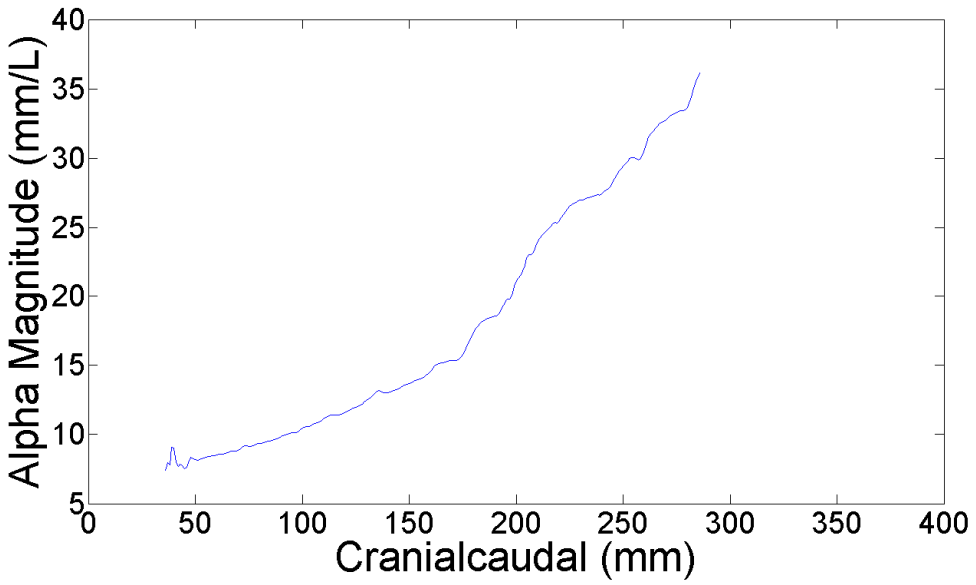


(a)

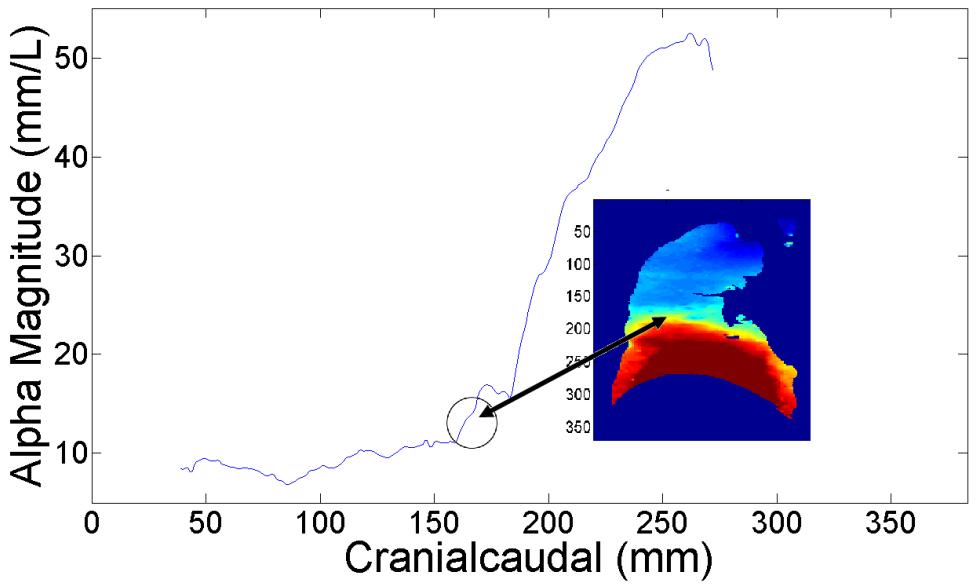


(

b)

Fig. 7.9 Comparison of $|\vec{\alpha}|$ change in cranialcaudal direction. a) Cranialcaudal profile of $|\vec{\alpha}|$ from the non-lung cancer patient. b) Cranialcaudal profile of $|\vec{\alpha}|$ from the lung cancer patient

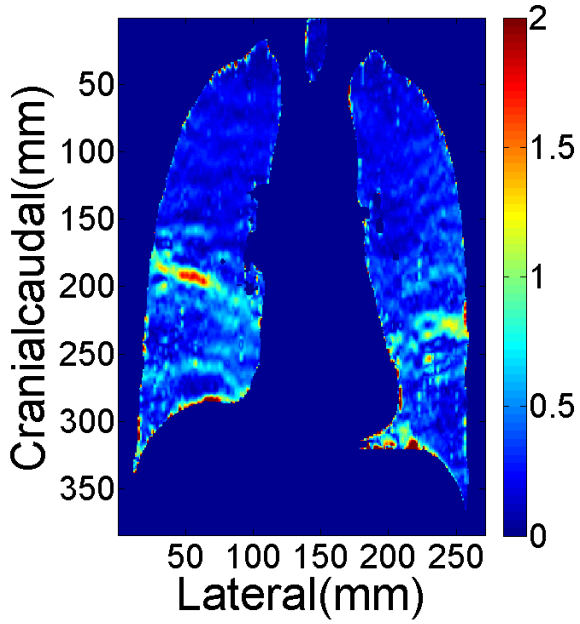


(a)

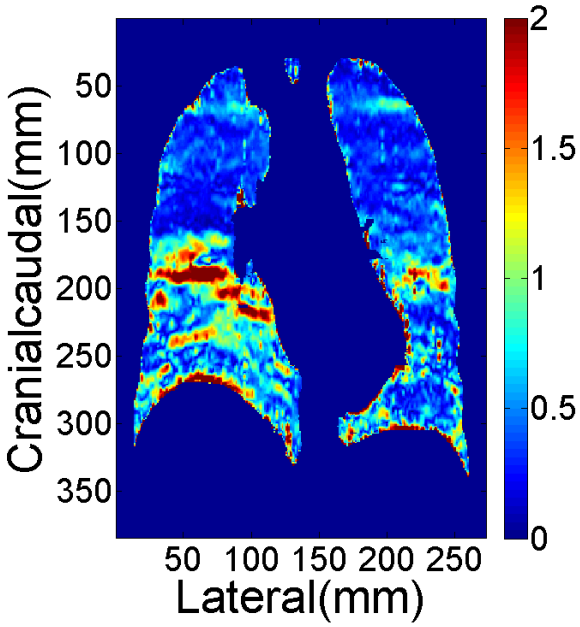


(b)

Fig. 7.10 Comparison of $\nabla \bullet \vec{\alpha}$ in (a) un-irradiated lung and (b) irradiated lung.

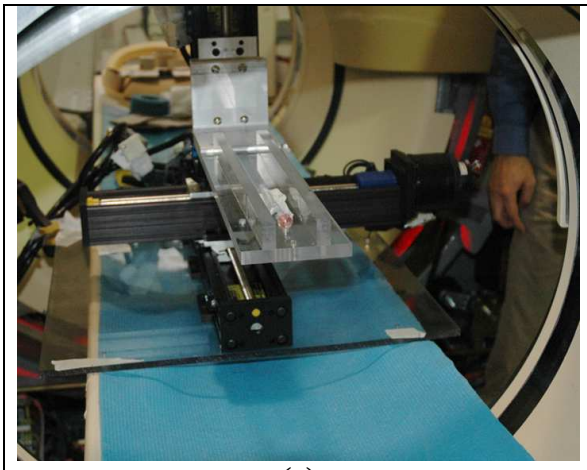

(a)

(b)

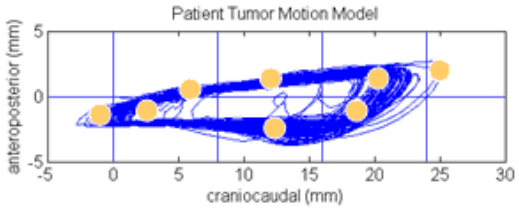


(c)

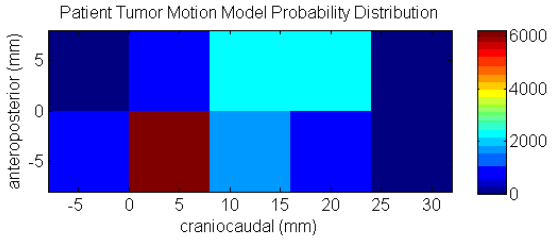


(d)

Fig. 7.11 a) The 4D phantom in a Philips PET/CT scanner. b) The spherical PET phantom with diameter of 1cm . c) Trajectory used to move the phantom in this study with the gating windows used to subdivide the trajectories. The dots denoted the average trajectory locations within each window. These positions were used to determine the shifts from each of the gated PET images. d) The probability distribution (in 20 ms time units) of the phantom motion distribution.

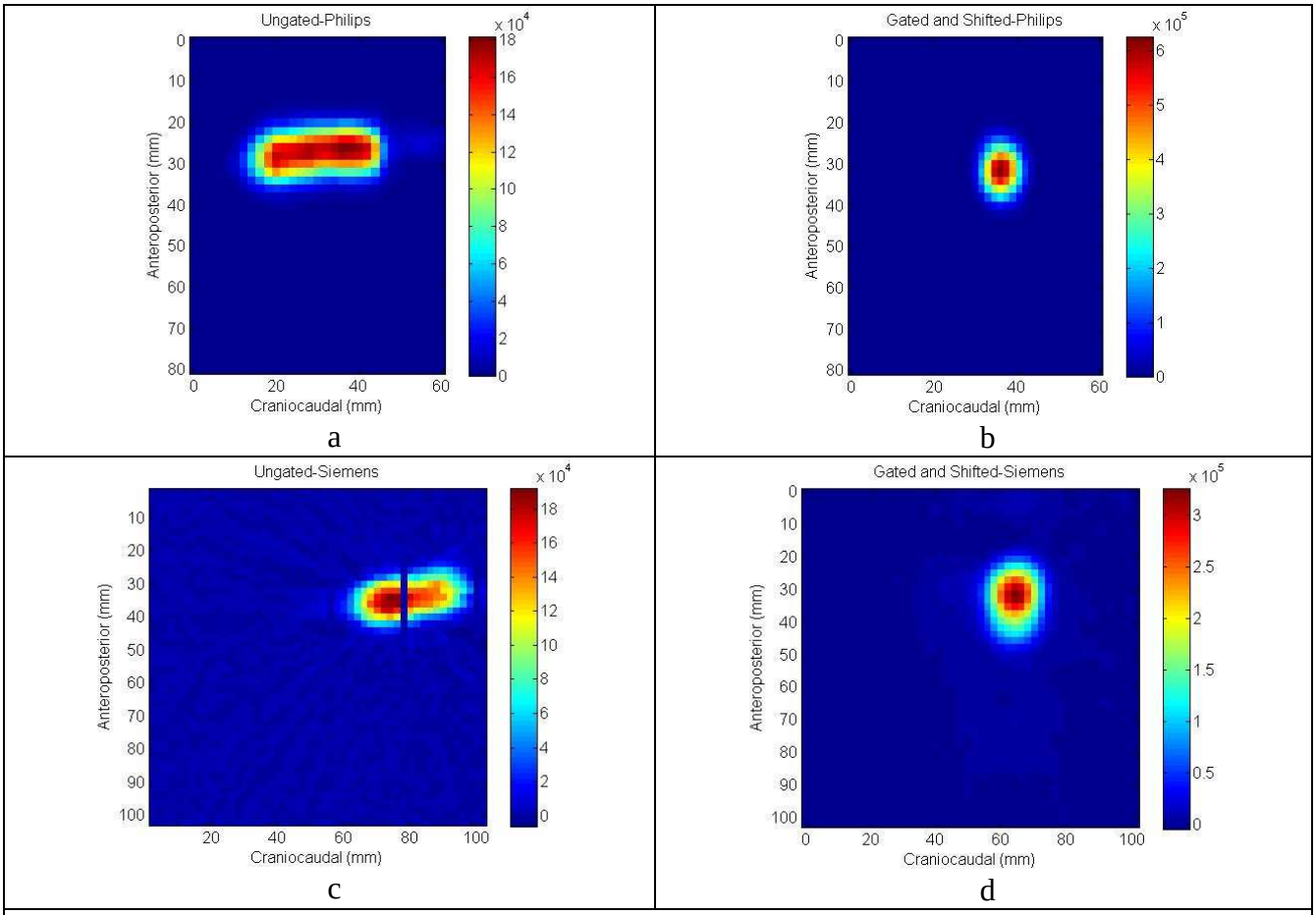


Fig. 7.12 a) The image reconstructed using all of the list-mode data (ungated) acquired in the Philips PET/CT scanner. The elongation of the spherical target due to the motion is evident. b) The shifted and summed PET image from Philips PET/CT scanner showing the recovery of the spherical target shape due to the quantitative nature of the gating and shifting algorithm. c) The ungated image from the Siemens PET/CT scanner. d) The shifted and summed PET image from the Siemens PET/CT scanner

# Chapter 8

# Conclusion

In this chapter, we review the results obtained in this dissertation in accordance with the objectives we had in mind.

## 8.1 Conclusions

A breathing motion model is needed to predict the motion of lung and lung tumor for more precise delivery of dose in radiotherapy and other clinical purposes like suppressing image artifacts. The breathing motion model is developed based on two observations: 1) the lung tissues move father along their trajectories as the patient breathes deeper. 2) the shapes of the trajectories resemble ellipse and circles due to the intrinsic hysteresis-like behavior.

Tidal volume was introduced into the breathing motion as the first surrogate to meet the first observation. Air flow was introduced as the second surrogate to give the motion a different path during exhalation than during inhalation. We hypothesize that any unique pair of tidal volume and air flow would give a unique location for the concerned tissue.

To determine the model parameter, a quantity of trajectory samples with corresponding tidal volumes and air flows are required. The trajectory samples were obtained by registering images scanned at different breathing phases. The image acquisition protocols were developed for both 16-slice Philips CT scanner and 64-slice Philips CT scanner as our scanner was updated while the research project went on due to the rapid developing of scanning technology. For most of the subjects tidal volume and air flow were measured using a spirometer. Some subjects that could not tolerate the spirometer, so tidal volume and air flow were calculated by converting the CT numbers to ratio of air in the CT volume.

Registration provides the trajectory of lung tissues that are the input of the breathing motion model. Registration is also one of the major sources of error. Another major sources of error are the image artifacts that distorts CT images. 3 image registration techniques were listed in Chapter 3 chronologically.

The preceding discussion identifies the variables and methods that are necessary for describing the lung and lung tumor trajectories. In Chapter 4, the continuity equation was applied to the breathing motion model to quantitatively test the model performance. The continuity equation resulted in a prediction that the volume integral of the divergence of the $\vec{\alpha}$ vector field was 1.11 for all patients. The integral of the divergence of the $\vec{\beta}$ vector field was expected to be zero. 35 patients were selected for this study. The $\vec{\alpha}$ vector field prediction was 1.06 ± 0.14, encompassing the expected value. For the $\vec{\beta}$ vector field prediction, the average value was 0.02 ± 0.03. These results provide

quantitative evidence that the breathing motion model yields accurate predictions of breathing dynamics.

To get a deeper understanding of the model parameters, we developed a biomechanical interpretation by investigating the normal stress in the lung. $\vec{\alpha}$ was modeled to be related to the tidal volume derivative of normal stress and $\vec{\beta}$ was related to the air flow derivative of normal stress. Averages of $|\vec{\alpha}|$ estimated using published data were compared with averages of $|\vec{\alpha}|$ from 49 patients. The comparison gave a discrepancy less than 10% between results from two methods. The spectrum of angles between $\vec{\alpha}$ and $\vec{\beta}$ was found to present a characteristic distribution where two peaks were observed in the data from most of the 49 patients. A calculation based on our biomechanical interpretation gave two maximum-likelihood angles that agreed to within 10º with the peaks observed in the patient data.

The model was employed to characterize the free-breathing patterns for a large cohort of patients. The $\vec{\alpha}$ and $\vec{\beta}$ distributions were examined for each patient to determine overall general patterns and inter-patient pattern variations. For most of the patients, the largest values of $|\vec{\alpha}|$ were observed in the inferior and posterior lungs. The hysteresis motion $\vec{\beta}$ had greater variability, but for the majority of patients, $|\vec{\beta}|$ was largest in the lateral lungs. The study showed that the breathing motion model has the potential for non-invasively predicting lung motion. The majority of patients exhibited similar $|\vec{\alpha}|$ maps, and the $|\vec{\beta}|$

maps showed greater inter-patient variability. The motion parameter inter-patient variability will inform our need for custom radiation therapy motion models. The utility of this model depends on the parameter stability over time, which is still under investigation.

The stability of the model parameters was investigate by enrolling radiotherapy patients with healthy lungs (no lung tumors) for two separate scans weeks apart. Currently we have available data from only one patient. The study on that patient showed that the distribution model parameter kept similar shapes. 84% of tissues investigated varied less than 20% in $|\vec{\alpha}|$ and only 53% varied less than 20% in $|\vec{\beta}|$. We will continue to recruit more patients to investigate the model stability in the future.

Other clinic applications in include the potential of $\vec{\beta}$ as an indicator of cancerous regions, divergence of the model parameters as an indicator of radiation damage and suppressing motion artifacts in PET images.

## 8.2 Future work

We anticipate continuing the following studies after the successful validation of the registration and the breathing motion model techniques

If the stability of model parameters is proved or normal fluctuation range is determined, we would continue this study in

1. Evaluation, staging and management of respiratory diseases in addition to cancer

2. Monitoring radiation damage
3. Quantitative guidance for treatment planners regarding the impact of linear accelerator gating on the accuracy and efficiency of radiation therapy dose distribution planning.

If the model is robust only within the time of the CT scan session, we would continue this study in

1. Quantitative nuclear medicine (PET/CT and SPECT/CT) study acquisition for free breathing patients without breathing motion artifacts
2. Quantitative evaluation of the benefit of tumor tracking on dose delivery accuracy and conformality.
3. Quantitative evaluation of the impact of breathing motion on IMRT dose delivery

This work is supported in part by NIHR01CA096679 and NIHR01CA116712.

[1]WHO, "Cancer," World Health Organization. (2006).

[2]A. C. Society, "Cancer Facts and Figures: 2009," Atlanta:American Cancer Society. (2009).

[3]M. C. Perry, "Diagnosis and Treatment of Lung Cancer: An Evidence-Based Guide for the Practicing Clinician," N Engl J Med. **344**, 1723-a-1724 (2001).

[4]A. R. Le Chevalier T, Quoix E, Ruffie P, Martin M, Douillard JY, Tarayre M, Lacombe-Terrier MJ, Laplanche A, "Radiotherapy alone versus combined chemotherapy and radiotherapy in unresectable non-small cell lung carcinoma," Lung Cancer. **10**, 239-244 (1994).

[5]B. Emami, M. V. Graham, and J. A. Purdy, "Three-dimensional conformal radiotherapy in bronchogenic carcinoma: considerations for implementation," Lung Cancer. **11**, S117-S128 (1994).

[6]K. Kubota, K. Furuse, M. Kawahara, N. Kodama, M. Yamamoto, M. Ogawara, S. Negoro, N. Masuda, M. Takada, and K. Matsui, "Role of radiotherapy in combined modality treatment of locally advanced non-small-cell lung cancer," J Clin Oncol. **12**, 1547-1552 (1994).

[7]M. K. Martel, R. K. Ten Haken, M. B. Hazuka, M. L. Kessler, M. Strawderman, A. T. Turrisi, T. S. Lawrence, B. A. Fraass, and A. S. Lichter, "Estimation of tumor control probability model parameters from 3-D dose distributions of non-small cell lung cancer patients," Lung Cancer. **24**, 31-37 (1999).

[8]L.-M. Sun, S. W. Leung, C.-J. Wang, H.-C. Chen, F.-M. Fang, E.-Y. Huang, H.-C. Hsu, S.-A. Yeh, C.-Y. Hsiung, and D. T. Huang, "Concomitant boost radiation therapy for

inoperable non-small-cell lung cancer: preliminary report of a prospective randomized study," International Journal of Radiation Oncology*Biology*Physics. **47**, 413-418 (2000).

[9]J. A. Hayman, M. K. Martel, R. K. Ten Haken, D. P. Normolle, R. F. Todd, III, J. F. Littles, M. A. Sullivan, P. W. Possert, A. T. Turrisi, and A. S. Lichter, "Dose Escalation in Non-Small-Cell Lung Cancer Using Three-Dimensional Conformal Radiation Therapy: Update of a Phase I Trial," J Clin Oncol. **19**, 127-136 (2001).

[10]S. Shimizu, H. Shirato, S. Ogura, H. Akita-Dosaka, K. Kitamura, T. Nishioka, K. Kagei, M. Nishimura, and K. Miyasaka, "Detection of lung tumor movement in real-time tumor-tracking radiotherapy," International Journal of Radiation Oncology*Biology*Physics. **51**, 304-310 (2001).

[11]T. Bortfeld, S. B. Jiang, and E. Rietzel, "Effects of motion on the total dose distribution," Seminars in Radiation Oncology. **14**, 41-51 (2004).

[12]P. K. D.A. Low, T. Bortfeld, M. Engelsman and S. Jiang, "The effects of motion on IMRT," Med. Phys. **31**, 1 (2004).

[13]J. Liang, D. Yan, L. L. Kestin, and A. A. Martinez, "Minimization of target margin by adapting treatment planning to target respiratory motion," International Journal of Radiation Oncology*Biology*Physics. **57**, S233-S234 (2003).

[14]H. D. Kubo and B. C. Hill, "Respiration gated radiotherapy treatment: a technical study," Physics in Medicine and Biology. **41**, 83-91 (1996).

[15]X. A. Li, C. Stepaniak, and E. Gore, "Technical and dosimetric aspects of respiratory gating using a pressure-sensor motion monitoring system," Medical Physics. **33**, 145-154 (2006).

[16]T. Neicu, H. Shirato, Y. Seppenwoolde, and S. B. Jiang, "Synchronized moving aperture radiation therapy (SMART): average tumour trajectory for lung patients," Physics in Medicine and Biology. **48**, 587-598 (2003).

[17]L. Papiez, D. Rangaraj, and P. Keall, "Real-time DMLC IMRT delivery for mobile and deforming targets," Medical Physics. **32**, 3037-3048 (2005).

[18]D. Tewatia, T. Zhang, W. Tome, B. Paliwal, and M. Metha, "Clinical implementation of target tracking by breathing synchronized delivery," Medical Physics. **33**, 4330-4336 (2006).

[19]D. A. Low, M. Nystrom, E. Kalinin, P. Parikh, J. F. Dempsey, J. D. Bradley, S. Mutic, S. H. Wahab, T. Islam, G. Christensen, D. G. Politte, and B. R. Whiting, "A method for the reconstruction of four-dimensional synchronized CT scans acquired during free breathing," Medical Physics. **30**, 1254-1263 (2003).

[20]H. Shirato, S. Shimizu, K. Kitamura, T. Nishioka, K. Kagei, S. Hashimoto, H. Aoyama, T. Kunieda, N. Shinohara, H. Dosaka-Akita, and K. Miyasaka, "Four-dimensional treatment planning and fluoroscopic real-time tumor tracking radiotherapy for moving tumor," International Journal of Radiation Oncology*Biology*Physics. **48**, 435-442 (2000).

[21]Y. Seppenwoolde, H. Shirato, K. Kitamura, S. Shimizu, M. van Herk, J. V. Lebesque, and K. Miyasaka, "Precise and real-time measurement of 3D tumor motion in lung due to breathing and heartbeat, measured during radiotherapy," International Journal of Radiation Oncology*Biology*Physics. **53**, 822-834 (2002).

[22]G. C. Sharp, S. B. Jiang, S. Shimizu, and H. Shirato, "Prediction of respiratory tumour motion for real-time image-guided radiotherapy," Physics in Medicine and Biology. **49**, 425-440 (2004).

[23]S. S. Vedam, P. J. Keall, V. R. Kini, H. Mostafavi, H. P. Shukla, and R. Mohan, "Acquiring a four-dimensional computed tomography dataset using an external respiratory signal," Physics in Medicine and Biology. **48**, 45-62 (2003).

[24]S. Minohara, T. Kanai, M. Endo, K. Noda, and M. Kanazawa, "Respiratory gated irradiation system for heavy-ion radiotherapy," International Journal of Radiation Oncology*Biology*Physics. **47**, 1097-1103 (2000).

[25]S. S. Vedam, P. J. Keall, V. R. Kini, and R. Mohan, "Determining parameters for respiration-gated radiotherapy," Medical Physics. **28**, 2139-2146 (2001).

[26]J. Hanley, M. M. Debois, D. Mah, G. S. Mageras, A. Raben, K. Rosenzweig, B. Mychalczak, L. H. Schwartz, P. J. Gloeggler, W. Lutz, C. C. Ling, S. A. Leibel, Z. Fuks, and G. J. Kutcher, "Deep respiration breath-hold technique for lung tumors: the potential value of target immobilization and reduced lung density in dose escalation," International Journal of Radiation Oncology*Biology*Physics. **45**, 603-611 (1999).

[27]D. Mah, J. Hanley, K. E. Rosenzweig, E. Yorke, L. Braban, C. C. Ling, S. A. Leibel, and G. Mageras, "Technical aspects of the deep inspiration breath-hold technique in the treatment of thoracic cancer," International Journal of Radiation Oncology*Biology*Physics. **48**, 1175-1185 (2000).

[28]K. E. Rosenzweig, J. Hanley, D. Mah, G. Mageras, M. Hunt, S. Toner, C. Burman, C. C. Ling, B. Mychalczak, Z. Fuks, and S. A. Leibel, "The deep inspiration breath-hold

technique in the treatment of inoperable non-small-cell lung cancer," International Journal of Radiation Oncology*Biology*Physics. **48**, 81-87 (2000).

[29]J. W. Wong, M. B. Sharpe, D. A. Jaffray, V. R. Kini, J. M. Robertson, J. S. Stromberg, and A. A. Martinez, "The use of active breathing control (ABC) to reduce margin for breathing motion," International Journal of Radiation Oncology*Biology*Physics. **44**, 911-919 (1999).

[30]T.-Q. L. D. R. Gary H. Glover, "Image-based method for retrospective correction of physiological motion effects in fMRI: RETROICOR," Magnetic Resonance in Medicine. **44**, 162-167 (2000).

[31]A. E. Lujan, E. W. Larsen, J. M. Balter, and R. K. Ten Haken, "A method for incorporating organ motion due to breathing into 3D dose calculations," Medical Physics. **26**, 715-720 (1999).

[32]W. Lu, P. J. Parikh, J. P. Hubenschmidt, J. D. Bradley, and D. A. Low, "A comparison between amplitude sorting and phase-angle sorting using external respiratory measurement for 4D CT," Medical Physics. **33**, 2964-2974 (2006).

[33]D. A. Low, P. J. Parikh, W. Lu, J. F. Dempsey, S. H. Wahab, J. P. Hubenschmidt, M. M. Nystrom, M. Handoko, and J. D. Bradley, "Novel breathing motion model for radiotherapy," International Journal of Radiation Oncology*Biology*Physics. **63**, 921-929 (2005).

[34]V. Baudet, P. F. Villard, F. Jaillet, M. Beuve, and B. Shariat, “Towards accurate tumour tracking in lungs,” Information Visualization, 2003. IV 2003. Proceedings. Seventh International Conference on, 2003.

[35]B. Jonson, L. Beydon, K. Brauer, C. Mansson, S. Valind, and H. Grytzell, "Mechanics of respiratory system in healthy anesthetized humans with emphasis on viscoelastic properties," Journal of Applied Physiology. **75**, 132-140 (1993).

[36]R. K. Lambert, T. A. Wilson, R. E. Hyatt, and J. R. Rodarte, "A computational model for expiratory flow," Journal of Applied Physiology. **52**, 44-56 (1982).

[37]A. M. Lorino and A. Harf, "Techniques for measuring respiratory mechanics: an analytic approach with a viscoelastic model," Journal of Applied Physiology. **74**, 2373-2379 (1993).

[38]E. Promayon, P. Baconnier, and C. Puech, "Physically-based model for simulating the human trunk respiration movements," in *CVRMed-MRCAS'97* (1997), pp. 379-388.

[39]B. Suki and J. H. Bates, "A nonlinear viscoelastic model of lung tissue mechanics," Journal of Applied Physiology. **71**, 826-833 (1991).

[40]S. Tokumoto, Y. Fujita, and S. Hirai, "Deformation modeling of viscoelastic objects for their shape control," Robotics and Automation, 1999. Proceedings. 1999 IEEE International Conference on, 1999.

[41]K. Volker, R. José, B. Günther, M. Georg, and G. Josef, "Respiratory system inertance: investigation in a physical inertance model," Technology and Health Care. **8**, 1-14 (2000).

[42]E. Weibel, "Morphometry of the Human Lung," Anesthesiology. **26**, 367 (1962).

[43]J. Mead, T. Takishima, and D. Leith, "Stress distribution in lungs: a model of pulmonary elasticity," Journal of Applied Physiology. **28**, 596-608 (1970).

[44]E. D'Angelo, F. M. Robatto, E. Calderini, M. Tavola, D. Bono, G. Torri, and J. Milic-Emili, "Pulmonary and chest wall mechanics in anesthetized paralyzed humans," Journal of Applied Physiology. **70**, 2602-2610 (1991).

[45]E. D'Angelo, E. Calderini, G. Torri, F. M. Robatto, D. Bono, and J. Milic-Emili, "Respiratory mechanics in anesthetized paralyzed humans: effects of flow, volume, and time," Journal of Applied Physiology. **67**, 2556-2564 (1989).

[46]D. Yang, W. Lu, D. A. Low, J. O. Deasy, A. J. Hope, and I. El Naqa, "4D-CT motion estimation using deformable image registration and 5D respiratory motion modeling," Medical Physics. **35**, 4577-4590 (2008).

[47]W. Lu, D. A. Low, P. J. Parikh, M. M. Nystrom, I. M. El Naqa, S. H. Wahab, M. Handoko, D. Fooshee, and J. D. Bradley, "Comparison of spirometry and abdominal height as four-dimensional computed tomography metrics in lung," Medical Physics. **32**, 2351-2357 (2005).

[48]W. Lu, P. J. Parikh, I. M. El Naqa, M. M. Nystrom, J. P. Hubenschmidt, S. H. Wahab, S. Mutic, A. K. Singh, G. E. Christensen, J. D. Bradley, and D. A. Low, "Quantitation of the reconstruction quality of a four-dimensional computed tomography process for lung cancer patients," Medical Physics. **32**, 890-901 (2005).

[49]R. Werner, B. White, H. Handels, W. Lu, and D. A. Low, "Technical Note: Development of a tidal volume surrogate that replaces spirometry for physiological breathing monitoring in 4D CT," Medical Physics. **37**, 615-619

[50]J. P. Lewis, "Fast Template Matching," Vision Interface. 120-123 (1995).

[51]B. G. S. B.K.P. Horn, "Determining Optical Flow," Artificial Intelligence. **17**, 185-203 (1981).

[52]T. P. C Zach, and H Bischof, "A duality based approach for realtime TV-L1 optical flow," Pattern Recognition (Proc. DAGM ). 214-223 (2007).

[53]J. A. Nelder and R. Mead, "A simplex method for function minimization," The Computer Journal. **7**, 308-313 (1964).

[54]D. A. Low, P. J. Parikh, W. Lu, J. F. Dempsey, S. H. Wahab, J. P. Hubenschmidt, M. M. Nystrom, M. Handoko, and J. D. Bradley, "Novel breathing motion model for radiotherapy," Int J Radiat Oncol Biol Phys. **63**, 921-929 (2005).

[55]M. P. Hlastala and A. J. Berger, *Physiology of respiration*. 2nd ed. (Oxford University Press, Oxford ; New York, 2001).

[56]W. Lu, P. J. Parikh, J. P. Hubenschmidt, J. D. Bradley, and D. A. Low, "A comparison between amplitude sorting and phase-angle sorting using external respiratory measurement for 4D CT," Med Phys. **33**, 2964-2974 (2006).

[57]S. J. Lai-Fook, "Pleural Mechanics and Fluid Exchange," Physiol. Rev. **84**, 385-410 (2004).

[58]T. Zhao, W. Lu, D. Yang, S. Mutic, C. E. Noel, P. J. Parikh, J. D. Bradley, and D. A. Low, "Characterization of free breathing patterns with 5D lung motion model," Medical Physics. **36**, 5183-5189 (2009).

[59]K. K. Brewer, H. Sakai, A. M. Alencar, A. Majumdar, S. P. Arold, K. R. Lutchen, E. P. Ingenito, and B. Suki, "Lung and alveolar wall elastic and hysteretic behavior in rats: effects of in vivo elastase treatment," J Appl Physiol. **95**, 1926-1936 (2003).

[60]J. R. Rodarte, G. Noredin, C. Miller, V. Brusasco, and R. Pellegrino, "Lung elastic recoil during breathing at increased lung volume," J Appl Physiol. **87**, 1491-1495 (1999).

[61]R. Chatterjee, *Mathematical Theory of Continuum Mechanics*. (Alpha Science Int'l Ltd, 1999).

[62]S. E. Stubbs and R. E. Hyatt, "Effect of increased lung recoil pressure on maximal expiratory flow in normal subjects," J Appl Physiol. **32**, 325-331 (1972).

[63]S. J. Lai-Fook, R. E. Hyatt, and J. R. Rodarte, "Elastic constants of trapped lung parenchyma," J Appl Physiol. **44**, 853-858 (1978).

[64]A. Zapletal, T. Paul, and M. Samanek, "Pulmonary elasticity in children and adolescents," J Appl Physiol. **40**, 953-961 (1976).

[65]K. I. M. McKinnon, "Convergence of the Nelder--Mead Simplex Method to a Nonstationary Point," SIAM Journal on Optimization. **9**, 148-158 (1998).

[66]M. Lippman, *Harrison's Principles of Internal Medicine*. ( McGraw-Hill, New York, 2008).

[67]R. Walker, "The complexities of breast cancer desmoplasia," Breast Cancer Res. **3**, 143 - 145 (2001).

[68]N. Ragavendra, J. W. Ju, J. Sayre, S. Hirschowitz, I. Chopra, and M. Yeh, "In vivo analysis of fracture toughness of thyroid gland tumors," Journal of Biological Engineering. **2**, 12 (2008).

[69]J. W. C. Ball, P. B. Stewart, L. G. S. Newsham, D. V. Bates, "Regional pulmonary function studied with xenon133," J Clin Invest. . **41**, 519-531 (1962).

[70]K. L. Miller, T. D. Shafman, M. S. Anscher, S.-M. Zhou, R. W. Clough, J. L. Garst, J. Crawford, J. Rosenman, M. A. Socinski, W. Blackstock, G. S. Sibley, and L. B. Marks, "Bronchial stenosis: An underreported complication of high-dose external beam radiotherapy for lung cancer?," International Journal of Radiation Oncology*Biology*Physics. **61**, 64-69 (2005).

[71]C. R. Kelsey, D. Kahn, D. R. Hollis, K. L. Miller, S.-m. Zhou, R. W. Clough, and L. B. Marks, "Radiation-induced narrowing of the tracheobronchial tree: An in-depth analysis," Lung Cancer. **52**, 111-116 (2006).

[72]S. M. Woolley and P. B. Rajesh, "The Use of PET and PET/CT Scanning in Lung Cancer," Asian Cardiovasc Thorac Ann. **16**, 353-354 (2008).